Summer 8-20-2019

Non-Contact Distillation

Rawand Muzafar Rasheed
Portland State University

Non-Contact Distillation

by

Rawand Muzafar Rasheed

A thesis submitted in partial fulfillment of the
requirements for the degree of

Master of Science
in
Mechanical Engineering

Thesis Committee:
Mark M. Weislogel, Chair
Raúl Bayoán Cal
Derek C. Tretheway

Portland State University
2019

Abstract

Leidenfrost phenomenon has been studied extensively for its role in applications ranging from nuclear reactor cooling, to metals manufacturing, combustion, and other fields. Herein, Leidenfrost phenomenon is pursued towards non-contact distillation processes with hopes of reducing or even eliminating contaminant fouling. In particular, the microgravity environment of a drop tower is exploited to demonstrate the facility with which droplets achieve and sustain the Leidenfrost state. Dynamic Leidenfrost impacts in microgravity are presented for impacts on hydrophilic and superhydrophobic planar substrates, macro-pillar arrays, confined passageways, and others. Nearly ideal elastic non-contact impacts and droplet oscillation modes are observed. Dynamic Leidenfrost impacts in microgravity for uniquely low velocity impacts are investigated analytically and experimentally. We find Leidenfrost vapor layer thicknesses on the order of millimeters for a 1 mL droplet of water with impact velocity 1 mm/s - a 100-fold increase relative to terrestrial vapor layers. Such results are supported by preliminary experimental observations. Further droplet distillation experiments are conducted in a terrestrial gravity environment using a heated tilted rotating hemi-circular track. Droplet evaporation rates and lifetimes are tabulated for the sliding/rolling drops at varying angular velocities and tilt angles. An analytical model for the evaporation rate of a rolling Leidenfrost droplet is developed and compared to the experimental results with good agreement. The empirical and analytical results serve as key design tools for sizing a prototypical non-contact distillation system for terrestrial desalinization or spacecraft water recycling.

Acknowledgements

This work is dedicated to the loving memory of my father. The sacrifices you made for us inspire me to push myself everyday to be better and to do good for everyone around me. I hope to one day be half the man you were.

A special thank you to everyone on the DDT team. Your support and help day in and day out has helped me learn and grow more than I could have ever wished for. Thank you to Karl Cardin, Logan Torres, and Erin Schmidt for teaching me how to be successful. I would not have made it without you.

Thank you to the folks at the NASA Johnson Space Center for supporting my interests and giving me the opportunity to explore what I have found to be intellectually exciting. A special thank you to John Graf. Your selfless commitment to helping make the world of others around you better is a quintessential example to live by.

A final thank you to my adviser, Mark Weislogel. I owe you a debt that can never be repaid. I can only hope that committing to a lifelong cause of investing in others and providing people with the gift of opportunity and inspiration will be enough to make you proud.

Financial support for this work has been provided by a NASA Space Technology Research Fellowship Leidenfrost Driven Waste-Water Separator, September 15, 2017: CoTR Jennifer Pruitt, grant 80NSSC17K0175.

Contents

List of Tables

List of Figures

Nomenclature

Latin Letters

A	Area
c_{p}	Specific heat
d	Droplet diameter
f	Interfactial area fraction
g	Gravitational acceleration
h_{fg}	Latent heat of Vaporization
ID	Inner diameter
L_{c}	Capillary length-scale
m	Mass
$\dot{m}$	Mass flowrate
$\dot{m}_{\mathrm{evap}}$	Evaporating vapor mass flowrate
OD	Outer diameter
p	Perimeter
q	Heat transfer
q_c	Thin film convective heat transfer
q_{fc}	Forced outer convective heat transfer
R	Radius
r	Time varying radius
r_t	First time derivative of radius
t	Time
T	Temperature
u	Velocity
u_v	Evaporating vapor velocity
x	Position
$\dot{x}$	Velocity
$\ddot{x}$	Acceleration

Greek Symbols

α	Wedge Half Angle
δ	Leidenfrost vapor layer thickness
μ	Dynamic viscosity
ρ	Density
σ	Surface Tension
θ	Angle
θ^*	Apparent contact angle
ω	Angular velocity

Subscripts

a	Air
c	Centrifugal
d	Droplet
f	Final
gs	Gas-Solid Interface
i	Incident
l	Liquid
lg	Liquid-Gas Interface
ls	Liquid-Solid Interface
o	Initial
R	Reflection
s	Surface
v	Vapor
∞	Ambient environment

Dimensionless Quantities

Bo	Bond number
Ep	Evapo-propulsion number: Ratio of Inertial and Evaporation Energies
Gr	Grashoff number
Pr	Prandtl number
Re	Reynolds number
Ri	Richardson number
We	Weber number

Acronyms

ESM	Equivalent system mass
EVA	Extravehicular Activity
ISS	International Space Station
NP	Nanoparticle
PTFE	Polytetrafluoroethylene
SEM	Scanning electron microscope
SPS	Static phase separator
STS	Space transportation system
SWCA	Static water contact angle
WRS	Water Recovery System

Chapter 1

Introduction

1.1 Large Length Scale Capillary Fluidics

In the gravity environment of Earth ($1g_o$), Mars ($0.38g_o$), and the moon ($0.17g_o$), gravitational forces largely dominate fluid physical processes. However, when gravity is sufficiently small, other forces become significant, in particular the surface tension force. The Bond number Bo is used to measure the relative magnitude of body forces with respect to surface tension forces at a fluid interface given by,

$$\mathrm{Bo} = \frac{\Delta\rho a {L_c}^2}{\sigma}, \tag{1.1}$$

where $\Delta\rho$ is the difference in density between two fluid phases, a is the ambient acceleration imposed on a fluid, and L_c is a characteristic free surface length scale. Surface tension forces become dominant when $\mathrm{Bo} \ll 1$. Classical terrestrial cases wherein surface tension forces are dominant include neutrally buoyant systems where $\Delta\rho \ll 1$, and small length scale systems where $L_c \ll 1$. The latter case is for microfluidic devices where characteristic system length scales are submillimetric. When $a \ll 1$ $\mathrm{Bo} \ll 1$, body forces are also negligible. This is often the case aboard orbiting spacecraft. In this unique regime, capillary forces are dominant even at large characteristic length scales $\sim \mathrm{O}(1\,\mathrm{m})$. For this reason, the study of capillary phenomenon in the absence of body forces is termed large length scale capillary phenomenon. The term 'capillary fluidics' describes capillary phenomenon at all length scales.

1.2 Microgravity Fluid System Mishaps Aboard Spacecraft

A plethora of systems aboard spacecraft to a great extent function on or utilize liquids. These systems include propulsion systems, a wide host of life support systems, phase separation devices, heat exchangers, and others [1] [2]. In the microgravity environment aboard spacecraft, capillary forces pose problems for fluid systems designers and play a role in human bodily function and quality of life in space. The design challenges of fluid systems aboard spacecraft are often non-trivial due to the fundamental difference between microgravity and gravity-dominated fluid physics. As a result, unforeseen consequences arising from capillary forces have been observed in various systems aboard spacecraft. Complications have arisen from wetting phenomenon, unforeseen capillary driven flows, phase separations, bubble formation in fluid lines, boiling, condensation, and others. A selection of examples are cited below. Sources describing such events include NASA technical reports, books summarizing technical achievements and lessons learned during various periods of space exploration, and other works telling the stories of astronaut experiences in space.

Instances of system complications resulting from condensation of humid cabin air have been reported throughout spaceflight history. Gordon Cooper's Mercury-Atlas 9 flight in 1963 experienced critical electrical equipment and sensor malfunction, which was linked to the condensation and capillary wicking of water on cool electrical components [3] [4]. The immediate solution required absorbing the water away using paper towels. Aboard Apollo 13, condensation accumulation on walls, panels, and wire harnesses in the command module turned into rain in the cabin upon re-entry decelerations in Earth's upper atmosphere [3]. The rate of condensation on walls and win-

dows on Apollo 16 was so significant during trans-earth injection that when the crew went to take photographic images, windows on the spacecraft had to be wiped between each image [5]. On numerous Apollo missions condensation in cabin and space suit air ducts produced free-flying droplets of water from the condensate buildup in airlines [6]. Subsequent freezing and sublimation of condensate resulting from cabin depressurization before extravehicular activity (EVA) caused fluids to freeze in lines on the Apollo 15 Lunar Module resulting in fluctuating pressures in the water/glycol pump and decreases in the water seperator speed [4]. Aboard the MIR space station power outages caused a massive build up of condensation throughout the spacecraft with reports of water condensate volumes up to 'a cubic meter in size' [7]. Astronauts reported devoting 4 to 8 hours a day, everyday, cleaning up condensate by mopping with used clothes or employing a 'device that sucked the water into an airtight bag.' The crew noted that water spread across the walls of the station, and migrated into wiring. Aboard space shuttle mission STS-32, water was discovered at the outlet of a humidity separator and reported to be approximately 250 mL in volume [8].

Migration of fluids due to wetting, disturbances, and other forces have resulted in fluids entering unintended places. During the Apollo missions, migration of condensed water in space suits caused faulty measurements from carbon dioxide sensors [4] [9]. Migration of moisture and other contaminates to sensors still plagues modern space suits [10]. Failure of a pitot style water separator caused by minute accumulation of silica resulted in the intrusion of a large amount of water into the helmet of a space suit, seriously threatening the life of an astronaut [10] [11]. In missions prior to STS-5 there were reports of migration of urine under a urinal cap, which was employed by astronauts during urination [12]. The cap was redesigned after discovering

that male users restricted airflow into the urinal cap due to the male anatomy, allowing urine to migrate throughout the cap.

Fluid containment in low-gravity poses challenges arising from the liberation of liquid droplets resulting from everyday astronaut actives (washing, eating, brushing teeth, etc.). Free-flying droplets are a concern due to their potential for causing electrical shorts, disrupting sensors, and compromising crew health, especially in cases of toxic liquids. Even non-toxic salt-water entering an astronaut's eye can cause significant discomfort and impair crew performance. Astronauts aboard Skylab described issues with the hand wash and expressed concerns of splashing water and a desire for an improved design that would contain liberated droplets [13]. Similar concerns were expressed for the shower aboard Skylab where the astronauts also mention a residual soap left over on skin that caused painful irritation. During the Apollo era, suppressing splashing during urination was a concern for life support systems designers [14]. Liberating the final drop of urine from the human body after urination has proven challenging in low-gravity with complications arising from improper liberation resulting in free-flying urine droplets [15]. The ‘last-drop’ problem continued well into the Space Shuttle era with temporary solutions involving increased urinal airflow and manual wicking procedures [12] [16].

Other fluid system mishaps aboard spacecraft involve gas bubbles in fluid lines, phase separation, and various thermal-fluid phenomenon. The space station heat pipe advanced radiator element (SHARE) was an experiment that experienced massive bubble generation in heat pipe channels to the point of halting fluid flow [17]. Improper design of hydraulic diameters between condenser and evaporator elements were found to be the root cause of the issues. The space shuttle humidity separator

(a condensing heat exchanger) experienced issues of liquid droplet carryover resulting from debris clogging pitot tubes [18]. A prefilter for the humidity separator was developed to alleviate the problem. The prefilter experienced water clogging issues at the air inlet resulting from insufficient pressure, and consequently insufficient shear forces required to drive the fluid downstream. Clogging at a downstream teflon screen was also observed. The clogging would only be relieved once sufficient clogging occurred increasing the overall pressure drop across the prefilter forcing the fluid through the device. Trapped hydrogen gas bubbles in potable water lines have been known to cause gastrointestinal upsets in astronauts [3] [19]. Work has been conducted on the NASA flash evaporator [20] [21]. The flash evaporator experienced issues with freezing on poorly heated surfaces with such surfaces requiring extra heat to maintain temperatures above the Leidenfrost point to significantly reduce physical contact between the liquid and ducting via the Leidenfrost vapor layer and prevent freezing [22]. Poor heat transfer of the Leidenfrost state also maintains elevated duct temperature which also delays freezing. The Leidenfrost point is also sensitive to wetting conditions. Surface contamination usually increases surface wettability for liquids, which increases the Leidenfrost temperature.

This brief history of fluid system mishaps is a preliminary outline of a more comprehensive review to come. The outlined examples of fluid system mishaps in microgravity demonstrate the challenges of fluid management in space where gravity is negligibly small causing other small order forces to become paramount. Most notably, capillary forces. As shown in prior examples, this results in unintended fluid system consequences such as unintended flows, clogging, bubble ingestion, etc.

1.3 Thesis Organization

In Chapter 2 we first review easy-to-fabricate superhydrophobic substrates with a variety of characteristics including thermal stability, corrosion resistance, and resistance to mechanical abrasion. Such properties are of potential interest for non-contact distillation processes and fouling-free fluid processing and transportation applications for use aboard spacecraft. An experiment investigating the fouling resistance of superhydrophobic surfaces exposed to intermittent streams of urine is presented with results showing up to a 30-fold reduction in fouling rates for superhydrophobic substrates compared to wetting surfaces. Chapter 3 outlines a study of Leidenfrost phenomena where Leidenfrost temperatures are combined with superhydrophobic substrates to promote robust non-contact distillation of dynamic fluid droplets. A detailed investigation of Leidenfrost droplet evaporation was conducted for dynamic sliding/rolling Leidenfrost droplets on an aluminum substrate. Novel microgravity dynamic Leidenfrost drop impact experiments are conducted revealing droplet transport modes in such states. Results from terrestrial Leidenfrost distillation experiments for droplets at varying velocities tangential to the substrate are presented along with analytical models for Leidenfrost droplet evaporation and lifetimes. Chapter 4 discusses the design and development of an omni-gravity non-contact Leidenfrost-driven water recovery system developed for waste-water distillation applications. The water recovery system was tested with salt-water demonstrating contact-free droplet distillation. Chapter 5 presents a variety of first-observations showcasing an airflow analog to the Leidenfrost phenomenon, cryogenic capillary auto-ejection, Leidenfrost puddle jump on a fluid interface, and Leidenfrost droplet ejection from an interior corner.

Chapter 2

The Unrealized Potential of Superhydrophobic Substrates in Advanced Life Support Systems

2.1 Introduction

In the absence of significant gravitational acceleration, multiphase fluid phenomena is controlled largely by surface tension and wetting conditions. The latter are characterized by the contact or wetting angle. Non-wetting conditions have not been exploited significantly aboard spacecraft to date despite their potential to passively repel and thus passively position liquids in highly advantageous ways. In this chapter we provide a brief review of the literature regarding the terrestrial applications of superhydrophobic substrates, including mention of examples found in nature and several theoretical foundations. We then provide a brief review of facile methods for producing such superhydrophobic substrates. Applications of such surfaces within the fluid systems aboard spacecraft are then discussed following demonstrations of large length scale superhydrophobic capillary phenomena in low-gravity drop tower experiments.

A class of substrates and surfaces that are strongly repellent to aqueous solutions are called superhydrophobic surfaces. Over the past 20 years, research into production methods of superhydrophobic surfaces has received significant attention for their use in a variety of applications including self-cleaning surfaces [23] - [28], drag reduction [29] - [31], anti-icing and anti-fog surfaces [32] - [36], fouling-free surfaces [37] - [39], fluid separation such as oil-water [40] [41], and corrosion protection for metals [42] [43]. A special class of surfaces that are simultaneously repellent to aqueous solutions,

oils, and alcohols are called superomniphobic surfaces [44].

The wettability of a substrate is defined by the equilibrium contact angle θ and the range of metastable contact angles above and below θ defined by contact angle hysteresis. Substrates with contact angle above 150°, and low contact angle hysteresis, $< \pm$ 5°, are classified as super-repellent, superhydrophobic surfaces. Figure 2.1 provides a common sketch for three equilibrium wetting conditions: wetting/partial wetting ($\theta <$ 90°), neutral wetting ($\theta = 90°$), and non-wetting ($\theta > 90°$). A surface is considered wetting/spreading when $\theta = 0°$. The equilibrium contact angle on a smooth surface has been defined by Young's relation

$$\sigma_{SV} = \sigma_{SL} + \sigma_{LV}\cos\theta, \tag{2.1}$$

where σ_{LV}, σ_{SV}, and σ_{SL} are the surface tensions of the liquid-vapor, solid-vapor, and solid-liquid, respectively. Figure 2.2 illustrates the interfacial force balance at the liquid-solid-gas contact line. According to Young's relation, to achieve large contact angles, the free surface energy σ_{SV} must be proportionally small. Young's relationship has an apparent theoretical limit of ~120° for water on teflon [45] [46]. The maximum experimentally observed equilibrium water contact angle on a smooth surface observed in practice is 130° [47] on a teflon surface.

Despite this apparent limit, many surfaces exist in nature that are superhydrophobic, with contact angles greater than 150°. The legs of water striders [48] - [50], various plant leaves [51] - [53], the eyes and wings of numerous insects [54] - [56], and the backs of certain beetles [57] - [60] are superhydrophobic. Oleophobic surfaces have also been observed in nature on the shells of soil dwelling arthropods [61] [62]. The common feature allowing all of these organisms the enhanced ability to repel fluids is

the presence of micro/nano-scale surface roughness. Wenzel [63] was perhaps the first to consider substrate surface roughness effects on contact angle

$$\cos\theta^* = r\cos\theta, \tag{2.2}$$

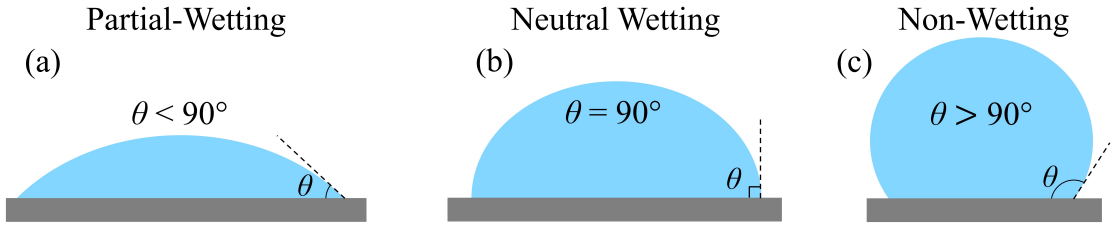

Figure 2.1: Liquid drop on a surface displaying (a) partial wetting, (b) neutral wetting, and (c) non-wetting states.

where θ^* is the apparent contact angle and r is the roughness ratio defined as the ratio between the area of the rough surface to the area of the projected surface with no surface roughness, $r \equiv A_{rough}/A_{smooth}$. Figure 2.3a provides a schematic of a droplet on a rough surface in a Wenzel state. The Wenzel model considers a fluid that is in total contact with all surface features. The roughness ratio for a smooth surface is $r = 1$, and for a rough surface $r > 1$. It is apparent from Eq. 2.2, also known as the Wenzel model, that the roughness ratio enhances both wetting and non-wetting surface characteristics. That is, if $\theta < 90°$, $\theta^* < \theta$, but if $\theta > 90°$, $\theta^* > \theta$. The

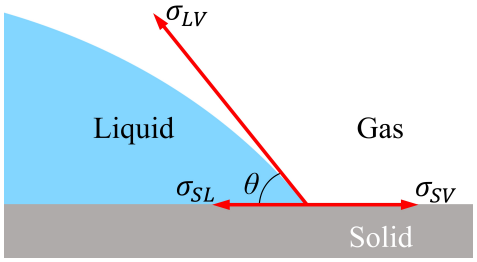

Figure 2.2: Force diagram of the three-phase contact line and relevant parameters for wetting.

Wenzel model can predict droplet behavior in certain circumstances, but has limited value in others. The Wenzel model does not imply any upper limit on the roughness ratio, and does not take into consideration surface features of varying length scales.

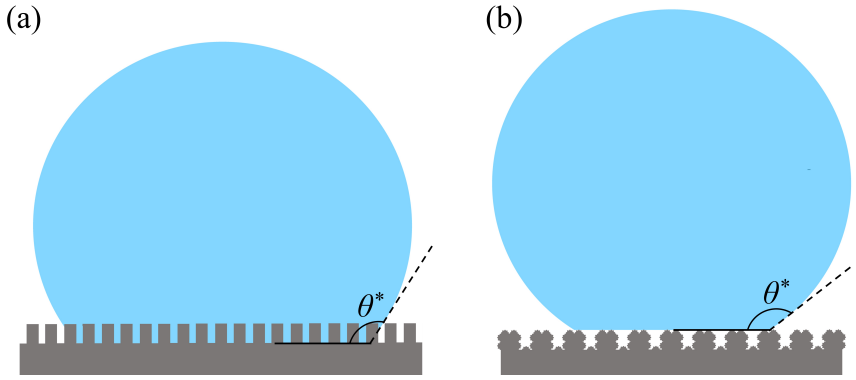

Figure 2.3: (a) A liquid droplet on a rough solid substrate in the Wenzel state. (b) A liquid droplet in the Cassie-Baxter state on a hierarchically rough solid substrate with a large surface roughness and a smaller secondary solid substrate feature atop the larger surface roughness.

A second Cassie-Baxter model [64] takes into account n different surface features

$$\cos\theta^* = \sum_{i=1}^{n} f_i \cos\theta_i, \tag{2.3}$$

where f_i is an interfacial area fraction and θ_i the equilibrium contact angle predicted from Young's relation. Eq. 2.3 is a general form and can be simplified by recognizing that two characteristic interfacial area fractions exist such that $f_{i,LV} + f_{i,SL} = 1$, where $f_{i,LV}$ is the liquid-gas interfacial area fraction and $f_{i,SL}$ is the solid-liquid interfacial area fraction. Substituting $\cos\theta_{i,LV} = -1$, and assuming a homogenous material and a single characteristic roughness, the Cassie-Baxter model simplifies to

$$\cos\theta^* = f_{SL}\,(1+\cos\theta) - 1, \tag{2.4}$$

Eq. 2.4 predicts the equilibrium contact angle of a droplet on a surface in the Cassie-Baxter state. The Cassie-Baxter model, unlike the Wenzel model, assumes that the liquid does not occupy the surface features. Instead, the liquid is only partially in contact with the solid. A liquid droplet in the Cassie-Baxter state is depicted in Fig. 2.3b. It can be shown via Eq. 2.4 that a fractional value for f_{SL} drastically increases the apparent contact angle. Surfaces that promote the Cassie-Baxter state have been used to achieve highly non-wetting characteristics with contact angles > 150° with low contact angle hysteresis < ± 5°, since the liquid droplet is in large part in contact with completely non-wetted air. Surfaces with more than one characteristic roughness feature are known as hierarchical surfaces, an approach that has been used to generate super-repellant surfaces that are superomniphobic [65].

Thus, to achieve superhydrophobicity, a surface must have low surface energy, and must have at least one characteristic surface roughness length scale. Contact angle hysteresis is also a critical parameter for characterizing superhydrophobic surfaces. Contact angle hysteresis is defined as the difference in advancing, θ_A and receding, θ_R contact angles on a solid substrate, $\theta_A - \theta_R$. Shown in Fig. 2.4 is a stationary droplet on a tilted surface in a gravitational field with advancing and receding contact angles labeled. A surface with low contact angle hysteresis has a small difference between advancing and receding values. Droplets readily slide or roll across such surfaces with high contact angle and low contact angle hysteresis, whereas droplets on surfaces with a high contact angle and large contact angle hysteresis move with an erratic stick-slip motion. Contact angle hysteresis arises from chemical and topographical variability in a surface. To achieve super-repellent surfaces, homogenous surface roughness and chemical composition are sought.

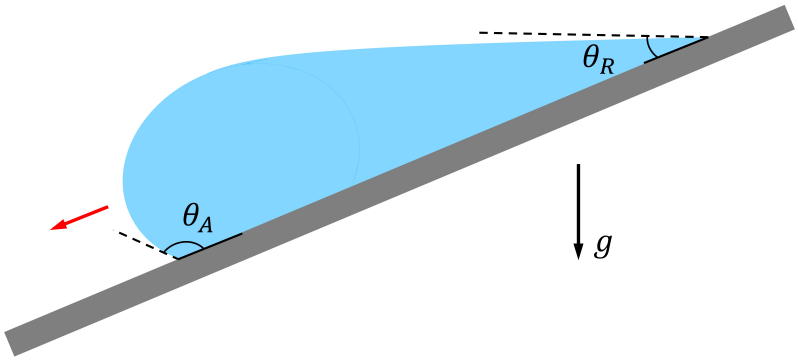

Figure 2.4: A droplet sliding/rolling down a surface with advancing contact angle, θ_A, and receding contact angle, θ_R.

Numerous advances have been made in the manufacture of superhydrophobic surfaces. There is a class of simple surfaces produced by chemical etch and immersion methods that provide an inexpensive means for producing superhydrophobic surfaces on metal substrates [66]. Such methods have the potential for production of superhydrophobic surfaces on complex geometries. Zhang et al. [67] developed an easy, one-step manufacturing process for the development of superhydrophobic surfaces on aluminum using a hydrochloric acid (HCl), ethanol, and myristic acid immersion method. The HCl chemically etches the aluminum surface, producing a hierarchically rough surface texture on the aluminum, while the myristic acid functionalizes the aluminum surface by depositing long chain, low-energy molecules (-CH_2 & -CH_3 groups) on the surface, rendering the aluminum superhydrophobic and exhibiting static water contact angles (SWCA) up to 160°. Wu et al. [68] highlight the increased reproducibility of aluminum superhydrophobic surfaces produced by acid etch and chemical functionalization. The use of an oxalic acid and HCl mixture for aluminum surface etching was found to produce a more homogenous microstructure. Li et al. [69] demonstrate added corrosion resistance to aluminum superhydrophobic surfaces by employing a potas-

sium permanganate passivation step after acid etch and before an immersion coating step wherein the substrate is immersed in a solution of ethanol and 20 mM trichlorosilane. A superhydrophobic surface with SWCA of 153.5° and corrosion resistance to saltwater was produced. Other studies have employed modified versions of acid etching and surface functionalization seeking improved non-wetting capabilities as well as other unique substrate surface properties. Facile fabrication of aluminum surfaces with anti-icing characteristics [70] - [74], surfaces functionalized using stearic acid for fluorine-free superhydrophobic surfaces relevant for environmentally friendly marine applications [75] [76], and surfaces that are thermally stable [77], and others [78] [79] have been developed using this method.

Facile coating methods have been employed for fabrication of superhydrophobic surfaces on various host substrates. Nanoparticles suspended in solutions that functionalize particles with low-energy coatings have been applied using curtain-coating [80], electrospinning [81], spin coating [82], and dip coating methods [83] [84]. Li et al. [85] produce superhydrophobic surfaces by brush coating a solution of titanium oxide nanoparticles modified in an ethanol- triethoxyoctylsilane solution. Gao et al. [86] produce superhydrophobic cotton surfaces by dip coating cotton in a solution of titanium oxide functionalized by n-octyltriethoxysilane. Spray coating methods have also been investigated for easy fabrication of superhydrophobic surfaces [87] - [89]. Li et al. [90] construct superhydrophobic surfaces on various substrates by spray coating a solution of amorphous silica nanoparticles, ethanol, and Trimethoxypropylsilane, achieving SWCA of 158.5°. Qahtan et al. [91] spray coat candle soot immersed in various solutions of acetone, isopropyl alcohol, and ethanol to produce superhydrophobic surfaces on metal substrates. Hancer & Arkaz [92] achieve SWCA greater than 178° on various sub-

strates using a spray coated solution of silicon dioxide nanoparticles, functionalized by perfluorodecyltrichlorosilane, in a poly-silicon matrix. Wei et al. [93] spray coat a mixture of silica nanoparticles, Methyltriethoxysilane, 3-[(Perfluorohexylsulfonyl) amino]-propyltriethoxysilane, and water on aluminum and glass substrates, producing syperhydrophobic surfaces that are also omniphobic, with SWCA of 158° and static contact angles of 148° and 134° for glycol and hexadecane, respectively. Chemical vapor deposition processes have also been studied for production of easy to produce superhydrophobic surfaces [94] - [97].

Nearly all fluid systems aboard spacecraft are dominated by interfacial fluid phenomenon, which is to a large extent determined by substrate wetting conditions. Superhydrophobic surfaces have numerous applications for spacecraft water systems. Anti-fouling surfaces for fluid transport, liquid-gas and liquid-liquid passive phase separation, condensing heat exchanger surfaces [98], and urine-water recovery are a few such applications. Herein, only facile methods for the production of superhydrophobic surfaces are outlined. Capillary fluidics experiments conducted in the microgravity environment of a drop tower are presented, demonstrating phenomenon arising from interactions with easily fabricated superhydrophobic surfaces. Current applications of superhydrophobic surfaces for use in spacecraft fluid systems are discussed.

2.2 Experimental

2.2.1 Drop Tower and Function

A drop tower [99] is employed in this work to simulate microgravity conditions. An image of the facility is shown in Fig. 2.5. A touch screen computer allows a single

operator to safely operate the drop tower assisted primarily by automated functions for quick experiment turn around with up to 20 drops per hour. An experiment rig is installed into a drag shield and released into freefall for 2.1 s. Figure 2.6 shows an example of an experiment rig inside the drag shield. The experiment rig and drag shield are released simultaneously. The drag shield is effectively guided by two 'non-contacting' cables. Two metal fins mounted to the sides of the drag shield pass through permanent magnets at the base of the tower. The relative motion between parallel magnetic fields and drag shield fins generate eddy currents in the fins that resist the motion and decelerate the falling masses which come to rest on foam pads. See Wollman [101] for further details.

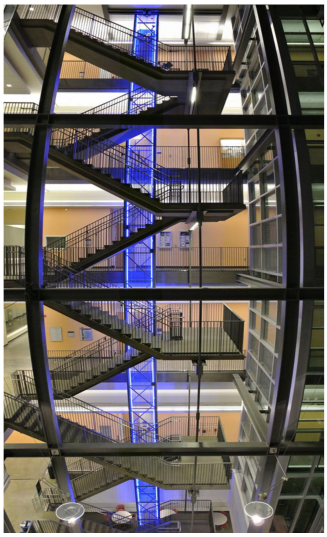

Figure 2.5: The 2.1 s drop tower. Image from Wollman [101].

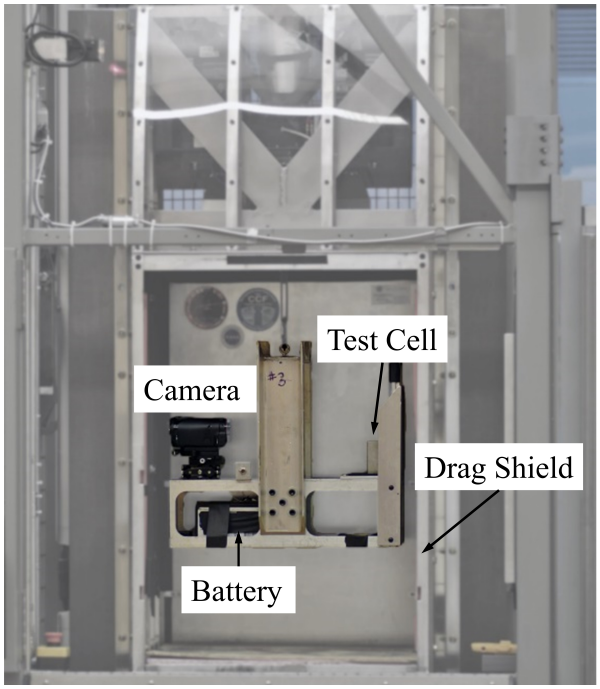

Figure 2.6: An experiment rig hanging inside the drag shield of the drop tower. Both the experiment rig and the drag shield are released at the same time. The experiment rig is allowed to fall freely inside the drag shield producing low-g (< $10^{-4} g_o$) conditions during the 2.1 s of free-fall. Image from Torres [102].

2.3 Production of Super-Facile Superhydrophobic Surfaces

Superhydrophobic surfaces requiring the most elementary of methods and materials for production have been developed and utilized in these studies. We define such surfaces as 'super-facile' surfaces. Superhydrophobic surfaces with SWCA of > 150° and roll off angles < 5° have been produced by spraying commercially available Dome Magic^{TM} Polytetrafluoroethylene (PTFE) spray on sand paper of varying grit sizes (200-2000 grit). The PTFE spray is applied in three lapping passes 15 cm away from the substrate.

Cytonix WX2100^{TM} one-step superhydrophobic spray is a commercially available

product that is a fluorine-based spray that creates nanometer sized surface features. Shown in Fig. 2.7a is a scanning electron microscope (SEM) image showing the surface with nanometer-scale features. Rust-Oleum Neverwet^{TM} spray is another commercially available solution, a silicon-based spray that also forms nanometer-scale features, as shown in Fig. 2.7b. Both sprays provide similar ease of application and performance for purposes of the present demonstrations.

A super-facile production method of a thermally stable superhydrophobic surface has been employed for high-temperature applications. A surface is coated with candle soot until completely blackened. The surface is then sprayed with Dome Magic^{TM} PTFE spray in two to three lapping passes 15 cm away from the substrate. The PTFE spray acts as a binder for the fragile soot producing a mechanically robust surface that is also thermally stable. This surface has been repeatedly used in experiments where surface operating temperatures exceed 220°C with negligible losses in wetting characteristics.

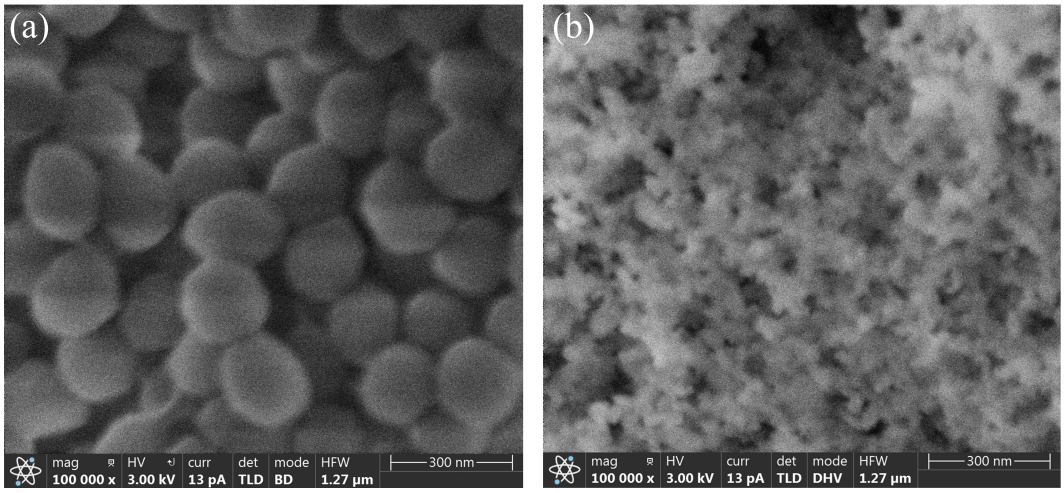

Figure 2.7: SEM images of (a) Cytonix WX2100^{TM} and (b) Rust-Oleum Neverwet^{TM} surface coatings.

2.4 Low-g Demonstrations and Applications

2.4.1 Liquid Rebounds from Superhydrophobic Surfaces

A host of drop tower experiments have been conducted demonstrating and investigating large length scale interfacial fluid phenomenon arising from interactions with superhydrophobic surfaces. In a microgravity environment, the length over which capillary forces are significant increases 1000-fold leading to enormous surface tension-dominated phenomena dictated often by the nanoscale wetting conditions of the system. For example, Attari et al. [103] demonstrate that large droplets (puddles) deposited on superhydrophobic surfaces in a terrestrial gravity environment spontaneously jump when experiencing a step reduction in gravity. This phenomenon has been coined 'puddle jumping.' Figure 2.8 shows a series of images of a 2 mL water puddle jumping from a superhydrophobic surface in the microgravity environment of a drop tower. Upon experiencing a step reduction in gravity (a) the puddle reorients into a sphere, resulting in (b) a collision of capillary waves, which overcome the negligible adhesion forces between the fluid and superhydrophobic substrate, resulting in the puddle (c) detaching from the surface with (d-e) constant velocity despite a variety of oscillation modes.

Puddle jumping phenomenon is a convenient droplet deployment method that has been applied in numerous microgravity experimental works including quantifying electrostatic forces on droplets [104] and droplet impact experiments [100] [105], such as dynamic Leidenfrost impacts [103]. However, droplet oscillations produced during the puddle jumping process are undesirable for experiments sensitive to droplet oscillation modes at impact. A microgravity, oscillation-free, droplet generator, referred

to as a 'Logan Shooter,' is a device that was developed for passive non-oscillating drop deployment [102], [106], & [107]. Figure 2.9a shows a schematic of the shooter. The Logan Shooter consists of two superhydrophobic surfaces forming a wedge. A volume of water is dispensed near the narrowest point of the wedge. Large liquid volumes form puddles. At initiation of the drop tower test the puddle jumps from the surface in an attempt to establish a sphere. However, the water is confined by the wedge which induces a capillary pressure gradient in the confined droplet that drives it out of the wedge. Oscillations in the drop are substantially damped during the ejection process. Figure 2.9b shows a Logan Shooter with 5° wedge half-angle ejecting a 10 mL droplet of water free of oscillations. Figure 2.10 shows a 30 Hz image overlay of a 1 mL droplet of water ejected between two parallel superhydrophobic plates using a Logan Shooter. The plates are separated by a distance of 13.5 mm, with overall length of 127 mm. The droplet has an initial velocity of 31.9 cm/s and final velocity of 23.2 cm/s. The sum of incident and reflection angles, $\theta_i + \theta_r$, increase from 93° to 100° over the course of five bounces.

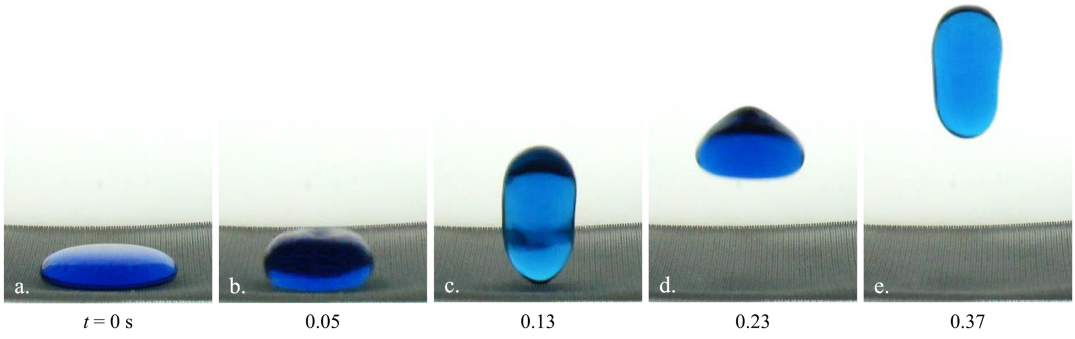

Figure 2.8: (a) A 2 mL puddle of water flattened under gravity. (b) The droplet reorients into a sphere in microgravity. (c) Collision of capillary waves propel the droplet off the surface with constant velocity and vertical oscillation modes (d) & (e) [103].

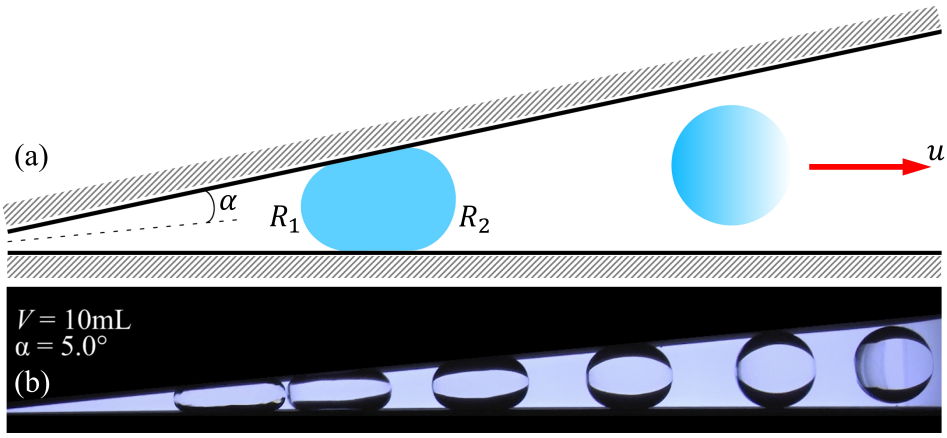

Figure 2.9: (a) A schematic of the Logan Shooter with half angle α and a droplet confined between two superhydrophobic plates. A capillary pressure gradient arising from the disparity in posterior, R_1, and anterior, R_2, radii of curvature forces the droplet out of the wedge with a velocity u. (b) A Logan Shooter with 5° half-angle ejecting a 10-mL droplet of water in a drop tower experiment [102].

Jet impacts on superhydrophobic surfaces in microgravity have been studied extensively [108] - [111]. Figure 2.11 shows an image of a large jet impacting a superhydrophobic surface in microgravity. The 6 mm diameter jet impacts with a Weber number defined as the ratio of inertial to surface tension forces We = $\rho u^2 D/\sigma = 21.4$ and a Reynolds number defined as the ratio of inertial to viscous forces Re = $\rho uD/\mu = 3005$. The incoming impact angle is 17.6° resulting in a perpendicular Weber number of 1.9. The jet is flattened upon impact due to inertial forces and rebounds into a cylindrical jet due to surface tension forces. In effect, the jet bounces off the surface. Such impacts have been studied extensively [108], mapping stable and unstable impact regimes.

Figure 2.10: A 30 fps overlay image of a 1 mL water droplet ejected with a Logan Shooter between two superhydrophobic plates. Plates are separated by a distance of 13.5 mm with total length of 127 mm. The droplet velocity decreases from 31.9 cm/s to 23.2 cm/s and $\theta_i + \theta_r$ increase from 93° to 100° over the course of five bounces. Image from Rasheed and Weislogel [112].

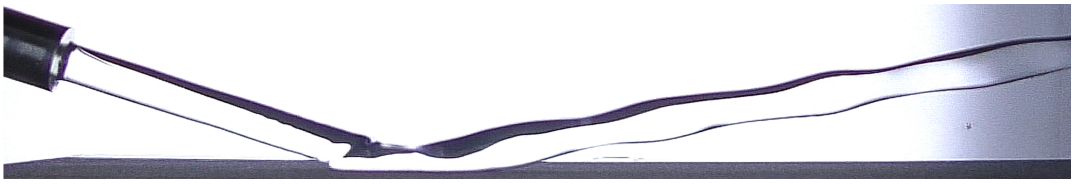

Figure 2.11: A large 6 mm jet impacting and rebounding from a superhydrophobic surface in a low-gravity environment. Image from Cardin [108].

2.4.2 Inhibition of Surface Fouling for Aqueous Fluid Streams

The wetting characteristics of many dilute aqueous solutions on superhydrophobic surfaces are often similar to those of pure water. Figure 2.12 provides a plot of contact angles for water, urine, and aqueous solutions of 25 g/L NaCl, sugar and KCl on a superhydrophobic surface consisting of candle soot and Dome Magic^{TM} PTFE spray applied to an aluminum substrate. All of the liquids exhibit contact angles > 150° and are within the standard error of water contact angle measurements.

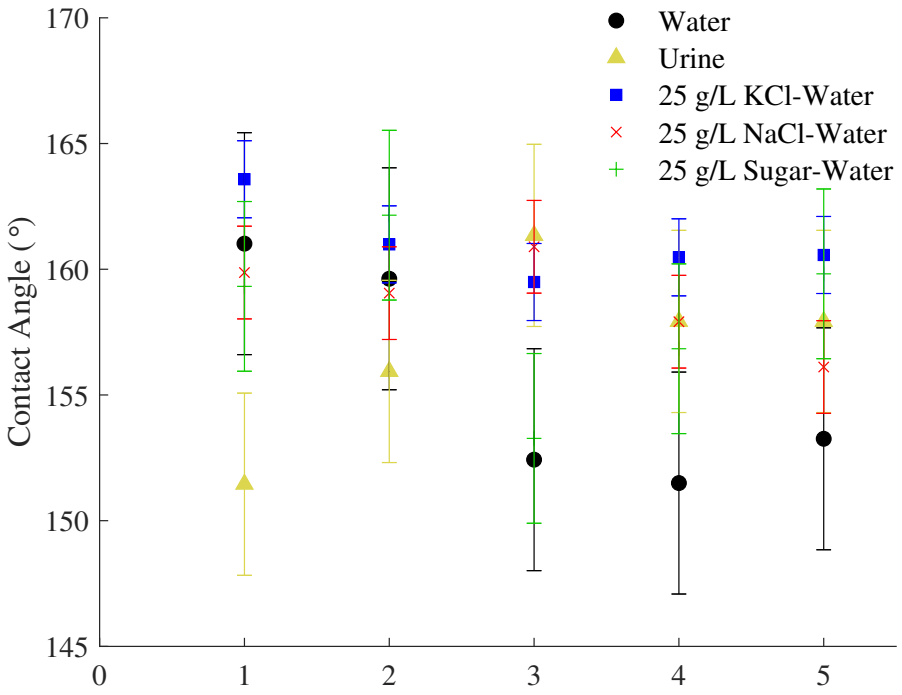

Figure 2.12: Contact angle results for water, urine, and aqueous mixtures on a superhydrophobic surface made of candle soot and Dome Magic^{TM} PTFE spray.

Transport of waste-water streams in microgravity has proven a challenging problem due to biofouling surfaces on system components and plumbing; i.e., urine streams [113] - [115]. The non-wetting characteristics of urine on superhydrophobic surfaces offers attractive opportunities for applications of non-wetting surfaces to separate, contain, and transport urine streams in microgravity. As an example, an experiment modelling the current operating conditions of the urinal funnel and hose system of the ISS potty was conducted [116] [117]. Two half-sections of 5.08 cm ID polyvinyl chloride (PVC) pipe were used in the tests. The inside of one half-section was coated with a superhydrophobic coating. Figure 2.13a provides a schematic of the experiment. A 100 mL volume of urine is poured into the half-pipe at a flowrate of 1

Lpm. The experiment is repeated every two to three hours for over one month. Figure 2.13b shows an image of the superhydrophobic half-pipe interior (above) and the non-hydrophobic half-pipe interior (below) after the first day of experimentation. A red box over a region on the non-hydrophobic half-pipe (Fig. 2.13b, bottom) shows initial signs of dry discolored urine residue on the non-hydrophobic pipe. Figure 2.13c shows an image of the same pipes after 31 days of testing. Discoloration of the uncoated pipe appeared at the first day of testing. The first signs of contamination for the superhydrophobic half-pipe were not detected until the 31^{st} day of testing (see red boxes). Figure 2.14 shows a plot of mass measurements for the PVC pipes over the span of 42 days of experimentation showing an average increase in mass of 3.1 mg per experiment for the non-hydrophobic half-pipe, and an average increase in mass of 0.5 mg per experiment for the superhydrophobic half-pipe. These preliminary results demonstrate what might be crudely approximated as 30-fold increase in surface life for the superhydrophobic surface compared to the non-hydrophobic surface.

2.4.3 Non-Contact Distillation

A novel, non-contact, heat-driven distillation method has been investigated to address NASAs water recovery challenge [112]. The method exploits the Leidenfrost phenomenon to perform distillation of droplet streams of waste-water. When a substrate's temperature is significantly higher than the liquid's boiling temperature, a droplet dispensed on the substrate will not undergo nucleate boiling, but will instead levitate on a layer of its own vapor. This vapor layer insulates the droplet from the heated substrate, reducing heat transfer to the liquid drop by orders of magnitude. Levitating droplets are not in contact with the surface, eliminating nucleation sites for bubble formation.

This contact-free mode of distillation has potential utility for addressing the urine water recovery challenges in a fouling-free system.

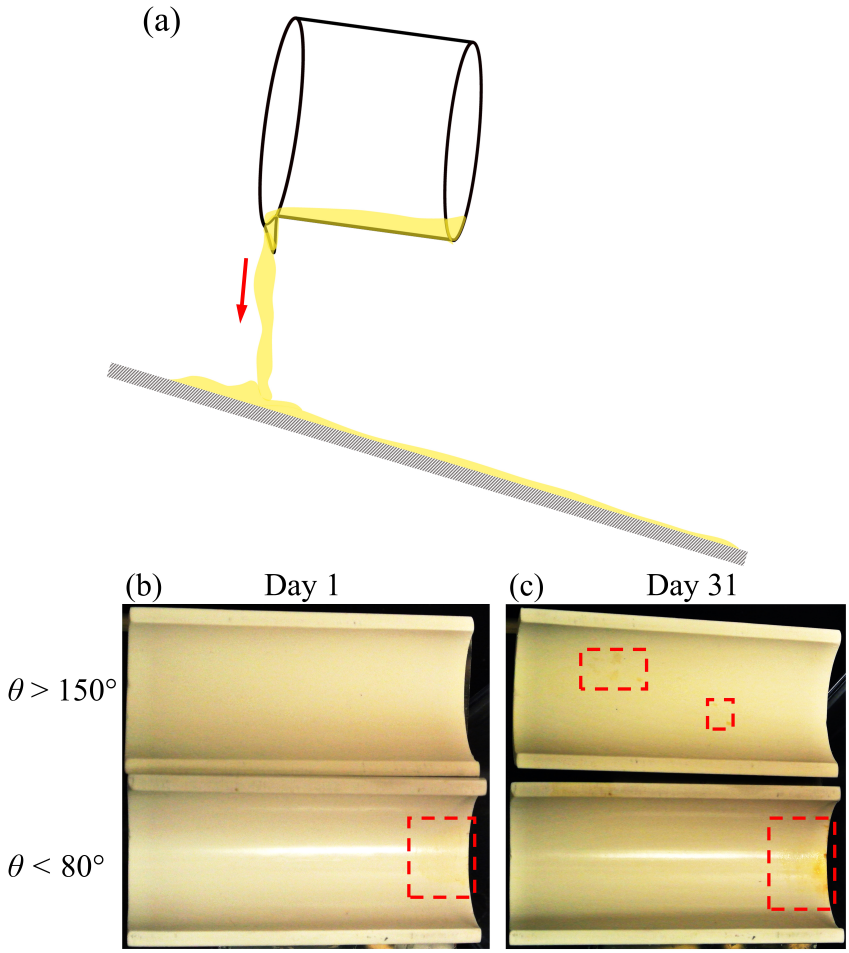

Figure 2.13: (a) Sketch of tests where urine is poured at 1 Lpm into a tilted PVC pipe. (b) Images of the superhydrophobic (above) and non-hydrophobic (below) interior surfaces of PVC pipes after 1 day and (c) 31 days of exposure. Red boxes highlight buildup of dry urine residue.

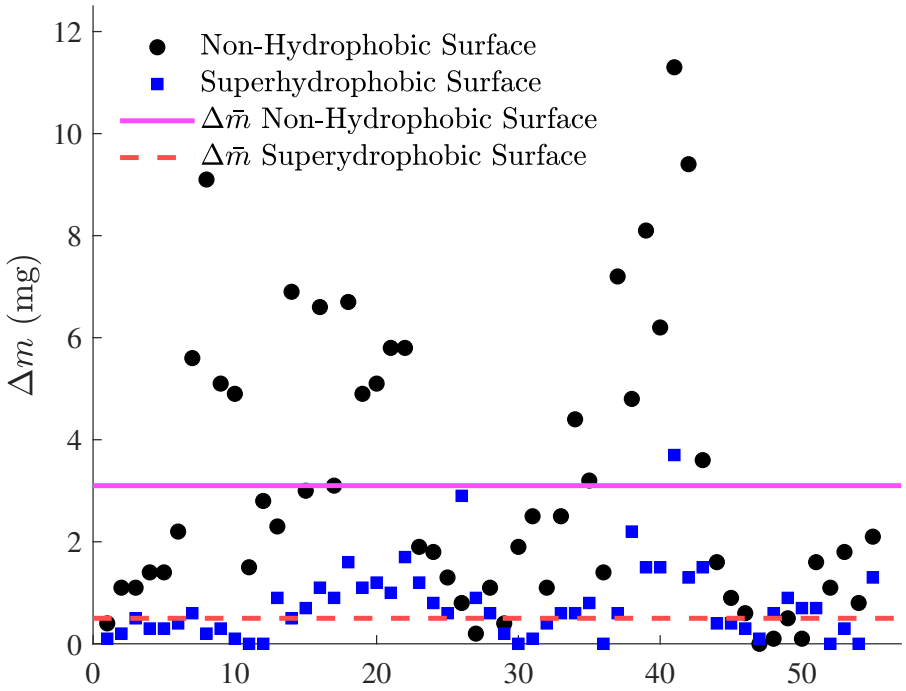

Figure 2.14: Change in mass for non-hydrophobic and superhydophobic surfaces as a result of 1 Lpm of urine flow across surfaces. Measurements taken over a span of 42 days indicate an average change in mass of 3.1 mg per experiment and 0.5 mg per experiment for the non-hydrophobic and superhydrophobic surfaces, respectively.

The Leidenfrost distillation method is enhanced by superhydrophobic surfaces. Superhydrophobic surfaces have been shown to dramatically decrease the Leidenfrost point temperature of water [118]. Dynamic Leidenfrost impact temperatures have been observed to decrease from 206°C on an aluminum surface to as low as 130°C on a superhydrophobic surface [112]. Figure 2.15 shows a series of 15 Hz images taken of a 1.3 mL water droplet in microgravity impacting a superhydrophobic substrate held at 140°C. A Logan Shooter is used to eject the water droplet free of oscillations toward the heated substrate with a normal velocity of 13.0 cm/s and a perpendicular Weber number of 3.1. The droplet impacts the substrate and elastically rebounds without

undergoing nucleate boiling. The reduction of Leidenfrost temperatures helps reduce energy consumption required for essentially non-contact Leidenfrost distillation. Superhydrophobic surfaces in conjunction with the Leidenfrost vapor layer separation provide an additional protection against contact between fluid and substrate [112].

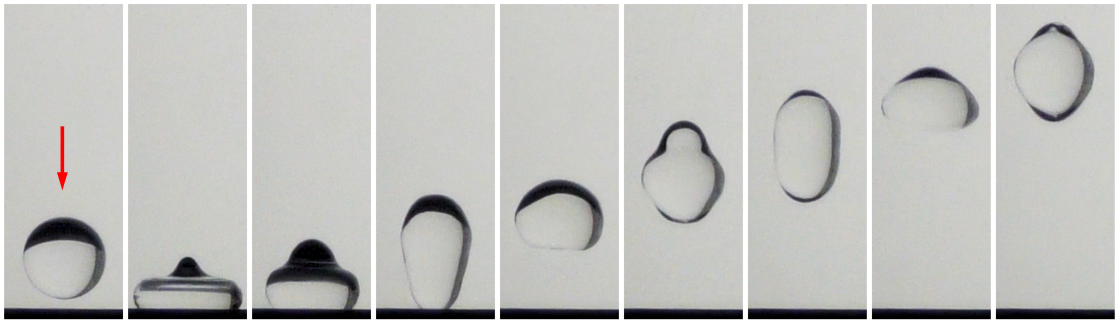

Figure 2.15: A sequence of 15 Hz images of a 1.3 mL water droplet impacting a planar superhydrophobic surface held at 140°C in a low-g drop tower test. The droplet is ejected using a passive Logan Shooter free of oscillations and normal to the substrate at 13.0 cm/s with a normal impact Weber number of 3.1 [119].

2.5 Conclusion

The recent advances in easy-to-fabricate superhydrophobic surfaces are readily applicable for low-g demonstrations leading to practical applications in fluids handling aboard spacecraft. Such surfaces require simple production methods and have gained significant attention in the past two decades. Desirable surface properties include thermal stability, corrosion resistance, wear resistance, bio-compatibility, and chemical stability, among others. Because such surfaces offer the potential for low-contact or even contact-free fluids handling aboard spacecraft, significant decreases in surface contamination might be achieved prolonging design life while reducing spares, mass, volume, costs, and crew time. Superhydrophobic surfaces offer a host of valued

characteristics for spacecraft fluids systems including increased thermal stability, corrosion resistance, resistance to mechanical abrasion, and more. The use of superhydrophobic surfaces in a selection of demonstrative drop tower experiments have been briefly presented herein which identify a variety of large length scale interfacial microgravity fluid phenomenon ranging from jumping puddles, to rebounding droplets, to bouncing jets, to non-contact low-g distillation exploiting superhydrophobic surfaces at or above the Leidenfrost temperature. Such demonstrations suggest that current life support system applications susceptible to biofouling plumbing may benefit greatly from the immediate deployment of such surfaces. The utility and potential performance improvements of fluid-based systems for these surfaces is high per unit design effort. Further low-g demonstrations are encouraged as well as the development of a suite of flight certified superhydrophobic substrates that might be employed in the life support systems aboard spacecraft.

Chapter 3

On-Demand Non-Contact Distillation: Low-g Demonstrations of a Leidenfrost Waste-Water Processor

3.1 Introduction

The National Aeronautics and Space Administration (NASA) has identified the separation and recovery of water from waste streams as a major challenge. NASA's technology roadmap has identified water recovery and management (TA 6.1.2) as an area in need of innovative technological solutions to enable human exploration of deep space. At least 98% water recovery from waste-water streams is required for such missions, a performance goal that is not yet attainable with current state of the art technology. It is also desirable to develop a water recovery system that significantly reduces the number of moving components, eliminates the need for urine storage, eliminates the need for addition of pretreat chemicals to urine, and unifies urine-brine processing. Herein, the foundations of a novel, non-contact, heat-driven distillation method are investigated as a potential method to address NASA's water recovery challenge.

Heat driven distillation is routinely employed to distill liquid-liquid and liquid-solute solutions. Such processes typically employ pool boiling. Film boiling is a less efficient boiling regime that is not usually exploited for distillation purposes. In the pool boiling regime, liquid droplets deposited on substrates slightly above the liquid's boiling temperature will undergo nucleate boiling and will boil away in seconds. However, if the substrate temperature is significantly higher than the liquid's boiling temperature, the droplet will not undergo nucleate boiling, but will instead levitate on its own

vapor layer. This vapor layer insulates the droplet from the heated substrate, reducing heat transfer to the liquid droplet by orders of magnitude. The levitating droplets are not in contact with the surface, eliminating nucleation sites for bubble formation. These combined effects increase droplet lifetimes by orders of magnitude. For example, a static 0.03 mL water droplet on a planar aluminum substrate above 193°C will require several minutes to completely evaporate. This phenomenon is called the Leidenfrost effect [120]. Figure 3.1 shows a droplet lifetime plot for a 2 mm diameter droplet of water on a polished aluminum surface at varying surface temperatures. The maximum droplet lifetime shown by the vertical line just below 150°C identifies the Leidenfrost point, the point of minimum heat flux.

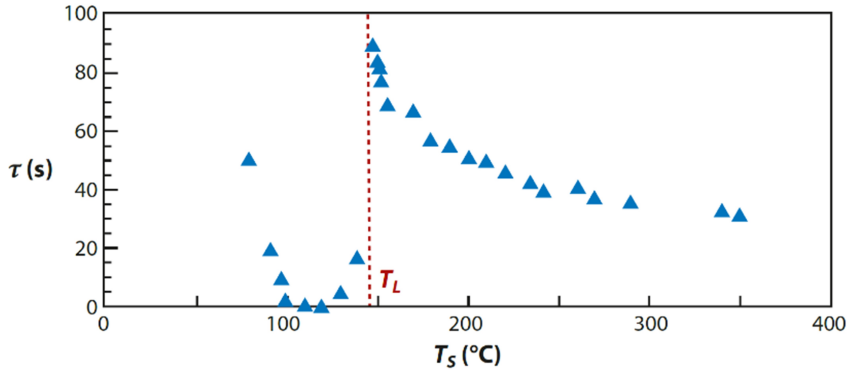

Figure 3.1: Lifetime plot for a 2 mm droplet of water deposited on a polished aluminum surface as a function of surface temperature, Ts. Figure from Quéré [121].

Though exploiting Leidenfrost phenomena may seem a poor choice due to low evaporation heat transfer rate, employing this phenomenon to distill streams of droplets is of interest for spacecraft applications due to the non-contact nature of the phenomenon, potentially enabling fouling-free distillation. Further, heat driven Leidenfrost distillation potentially allows for streams of waste-water solutions to be dis-

tilled fully to dry salt. Distillation rates are also comparable to certain liquid production rates (i.e., astronaut urine production) permitting essentially real-time distillation of streams of droplets at elevated temperatures. Stamey and Mihara [122] present experimental results for bacterial growth in sterile urine from human subjects. Results show that exponential bacterial growth occurs after two hours for all types of bacteria. Liquid solutions of urine processed essentially on-demand at temperatures in excess of 70°C ensure minimal microbial growth, reducing, if not eliminating the need for urine pretreat chemicals, which are used to significantly hinder the rate of bacterial growth in urine.

Leidenfrost droplets are highly mobile due to the vapor layer separating droplets from heated substrates. Viscous drag from the vapor layer is negligibly small leading to nearly frictionless motion across heated surfaces. Such mobility of Leidenfrost droplets encourages the possibility for competitive microgravity distillation system designs that employ heated conduits and a simple motive force for droplet streams in the form of airflow, pressure gradient, or the vapor production of the evaporating droplets themselves.

The Leidenfrost effect has been studied extensively for its relevance to numerous applications including spray cooling, fuel combustion, nuclear reactor cooling, jet and rocket engine propulsion, manufacturing of metals, and others [123] - [131]. Biance et al. [132] investigated Leidenfrost phenomenon providing a scale expression for static Leidenfrost droplet lifetimes. The dynamics of Leidenfrost droplet impacts have been investigated in depth [133] - [136]. It has been shown that the dynamic Leidenfrost point is a function of Weber number [135] as is the maximum spreading of the drops on impact [136]. Extensive experimental investigations quantifying heat transfer for dy-

namic Leidenfrost droplet impacts have been conducted [137] - [141] as well as mathematical considerations for heat transfer in the dynamic Leidenfrost mode [137] [142]. Leidenfrost droplet heat transfer and evaporation rates have also been experimentally investigated in the static case [143].

Maquet et al. [144] demonstrate that although the Leidenfrost point itself has a weak dependence on gravity level, Leidenfrost droplet lifetimes have a strong inverse dependence on gravity. Veldhoven and Capelleveen [145] show decreases in Leidenfrost temperature with decreasing ambient pressure. Chen et al. [146] show dramatic increases in dynamic Leidenfrost point temperature with increased levels of alcohol surfactants, showing that increases in the Leidenfrost point are due to decreasing surface tension.

Takata et al. [147] show increases in the Leidenfrost point with increased surface wettability. Kim et al. [148] report an increase and decrease in the Leidenfrost point for water on hydrophilic and hydrophobic surfaces, respectively. Kim et al. [149] [150] report significant increases in the Leidenfrost point of water as a result of impacts on porous and wetting micro-pillared surfaces. Such surface structures are found to disrupt and collapse vapor layer formation. Similar observations have been documented for wetting microstructured surfaces [151] - [154] as well as for surfaces consisting of carbon nanofibers [155]. Kwon et al. [156] report significant increases in the Leidenfrost point with decreasing micropillar density on wetting surfaces. Significant reduction in Leidenfrost point has also been reported on microstructured non-wetting surfaces [157] [158]. Vakarelski et al. [158] report significant decreases in the Leidenfrost point on microstructured superhydrophobic surfaces due to vapor layer stabilization on such surfaces. Kim et al. [148] also develop mathematical predictions for the dy-

namic Leidenfrost point on structured surfaces.

Exploratory low-gravity Leidenfrost behavior has been pursued in drop tower tests [103] [105]. As presented in Chapter 2, we present facile production methods for superhydrophobic surfaces, including thermally stable surfaces, which are utilized in this study. Superhydrophobic surfaces were also shown to reduce fouling of surfaces resulting from streams of urine by a factor of 30 [159]. In this work, Leidenfrost droplet modes of transport under varying conditions in microgravity are presented. Microgravity drop tower experiments include dynamic Leidenfrost impacts of oscillation free droplets on surfaces with varied wettability under varying impact conditions, droplet transport modes through conduit bends, and millimetric Leidenfrost vapor layer formation in the unique low-g Leidenfrost regime. Mathematical models are presented that predict Leidenfrost vapor recoil force and vapor layer thickness in the absence of gravity resulting in a newly formulated dimensionless parameter the Evapopropulsion number Ep. Results for experimental investigations extending terrestrial Leidenfrost droplet lifetime experiments for dynamically rolling droplets on heated substrates are also presented. The self-cleaning nature of fouled, superheated, superhydrophobic surfaces is also observed and reported. A model that predicts Leidenfrost droplet lifetime for droplets in the dynamic rolling mode in a terrestrial gravity environment is developed, showing good prediction of experimental results. These results have practical design implications for potential spacecraft applications.

3.2 Experimental

3.2.1 Microgravity Droplet Generators

To repeat, a microgravity, oscillation-free, droplet generator, referred to as a 'Logan Shooter,' is employed in the dynamic Leidenfrost impact experiments in microgravity. The Logan Shooter requires superhydrophobic non-wetting surfaces to function properly. For purposes of conducting dynamic Leidenfrost droplet impact experiments with wetting liquids such as ethanol, the method of passive capillary droplet ejection through a converging circular tube is employed as studied by Wollman [101]. Fluids with contact angle θ less than 90° rise to considerable heights in tubes in microgravity. Adding a nozzle to the end of the tube provides a mechanism for local liquid acceleration which adds enough local inertia to the liquid that a jet is spontaneously ejected from the nozzle. This jet breaks up into droplets which are then employed downstream in dynamic Leidenfrost impact experiments. Figure 3.2 shows passive capillary ejection of 5 cS PDMS (Polydimethylsiloxane) liquid in a 60 mm long, 6 mm ID circular glass tube with a converging nozzle of 1.2 mm ID at the end of the tube.

Figure 3.2: Spontaneous capillary rise and ejection of 5 cS PDMS in a circular tube with nozzle. Figure from Wollman [101].

3.2.2 Rolling Leidenfrost Droplets

Superhydrophobic Channel

An aluminum plate with 6.35 mm wide hemi-circular section milled circular track 56 mm in diameter is mounted to a turntable. The turntable is then tilted with respect to gravity and mounted to a lab bench. The plate surface is coated with a superhydrophobic coating consisting of a PTFE spray (Dome Magic^{TM}) over a soot layer deposited by candle flame [159]. Figure 3.3 provides images of the apparatus with top-view images of the circular track with a capillary-sized droplet of 25 g/L aqueous NaCl mixture inside the track. A variable speed DC motor is used to drive the turn-table with mounted aluminum plate. To the aluminum plate is mounted a 150-Watt strip heater controlled via Arduino control circuit comprised of thermocouples, ambient temperature thermocouple, humidity sensor, solid-state relays, and Arduino SD Shield for data acquisition.

The Arduino controller is programmed to establish the plate temperature. Once the setpoint temperature is reached, a droplet is dispensed in the channel while simultaneously turning on the DC turntable motor. A highspeed HD video camera records the events. The combined effects of plate rotation, plate tilt with respect to gravity, super-hydrophobicity, and Leidenfrost temperatures cause the droplet to roll ever-downwards along the channel. The droplet continues to roll until completely evaporated. Figure 3.3c shows an image of a droplet at the beginning of one such experiment with plate temperature of 170°C. The 25 g/L aqueous NaCl droplet initial volume is ~0.029 mL. Figures 3.3d and e provide images of the droplet at t = 56 s and t = 110 s, respectively. Figure 3.3f provides an image of the salt crystal left behind following com-

plete evaporation at t = 164 s. This apparatus is utilized for Leidenfrost droplet evaporation experiments atop a superhydrophobic surface, especially droplets of aqueous mixtures and urine. Such experiments provide insight on fouling mechanisms for superhydrophobic surfaces due to complete distillation and deposition of salt solutions.

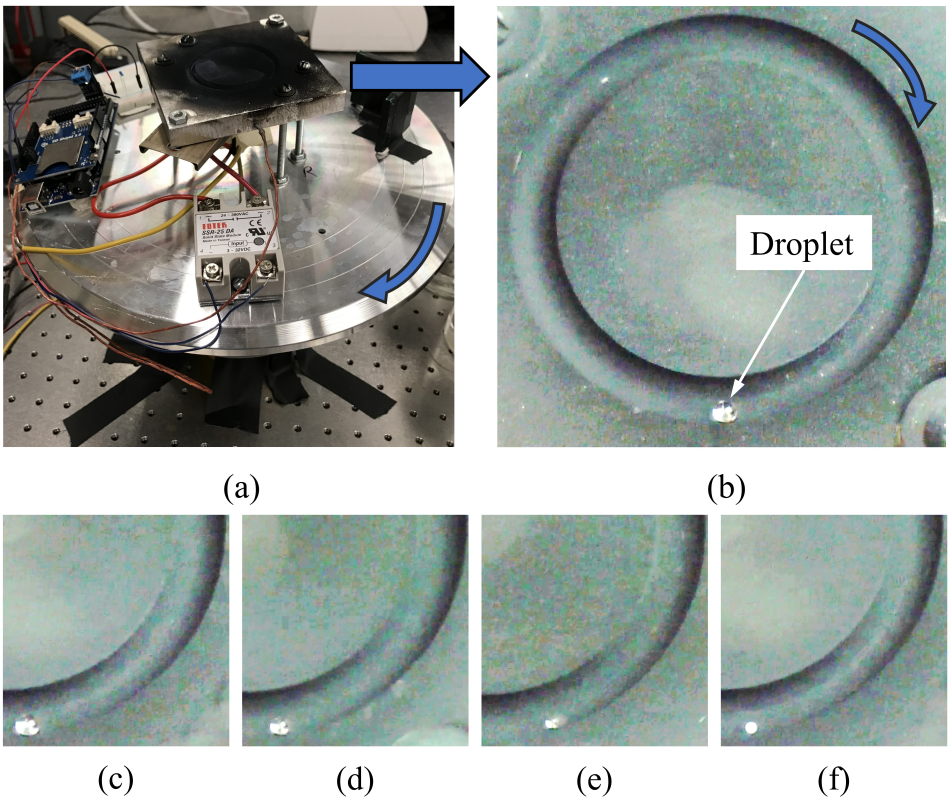

Figure 3.3: (a) Image of the experimental setup with the blue arrow pointing in direction of tilted turntable rotation. (b) A capillary-sized droplet (~0.029 mL) in a 6.35 mm wide, 56 mm diameter channel. (c) A droplet of 25 g/L aqueous salt solution rolls along the superhydrophobic channel held at 170°C. Image taken at t = 0 s. The droplet evaporates in time (d) t = 56 s and (e) t = 110 s. (f) Complete distillation leaves a single salt crystal in the channel, t = 164 s.

Aluminum Channel

A circular aluminum plate with 11.7 ± 0.1 mm wide hemi-circular channel machined circular track 129 ± 1 mm in diameter is shown in Fig. 3.4a. The plate is mounted in the center to a gearbox shaft attached to a variable speed DC motor. Mounted underneath the plate is a 450 W ring heater controlled via Arduino control circuit comprised of thermocouples, ambient temperature thermocouple, humidity sensor, solid-state relays, and Arduino SD Shield for data acquisition. The whole assembly is mounted to a precision vise capable of continuous and accurate adjustment of the plate tilt angle. Figure 3.4b shows a cross-sectional view of the apparatus tilted with angle θ. A pancake slip ring is mounted to the shaft above the circular plate for connection of rotating electrical circuitry to stationary objects (i.e., rotating heater and thermocouple wires to stationary outlet and Arduino microcontroller, respectively). Figure 3.4c shows a droplet of water with red food coloring in the hemi-circular channel heated past the Leidenfrost point of water on aluminum rotating with angular velocity ω.

The Arduino controller is programmed to establish the plate temperature. Once the setpoint temperature is reached, a droplet is dispensed in the channel while simultaneously turning on the DC turntable motor. A highspeed HD video camera records the events. The combined effects of plate rotation, plate tilt with respect to gravity and Leidenfrost temperatures cause the droplet to roll ever-downwards along the channel. The droplet continues to roll until completely evaporated. From these experiments we establish maximum Leidenfrost evaporation rates via droplet lifetime and evaporation rate measurements. Such rates can be used to estimate envelope and performance metrics for low-g Leidenfrost distillation devices.

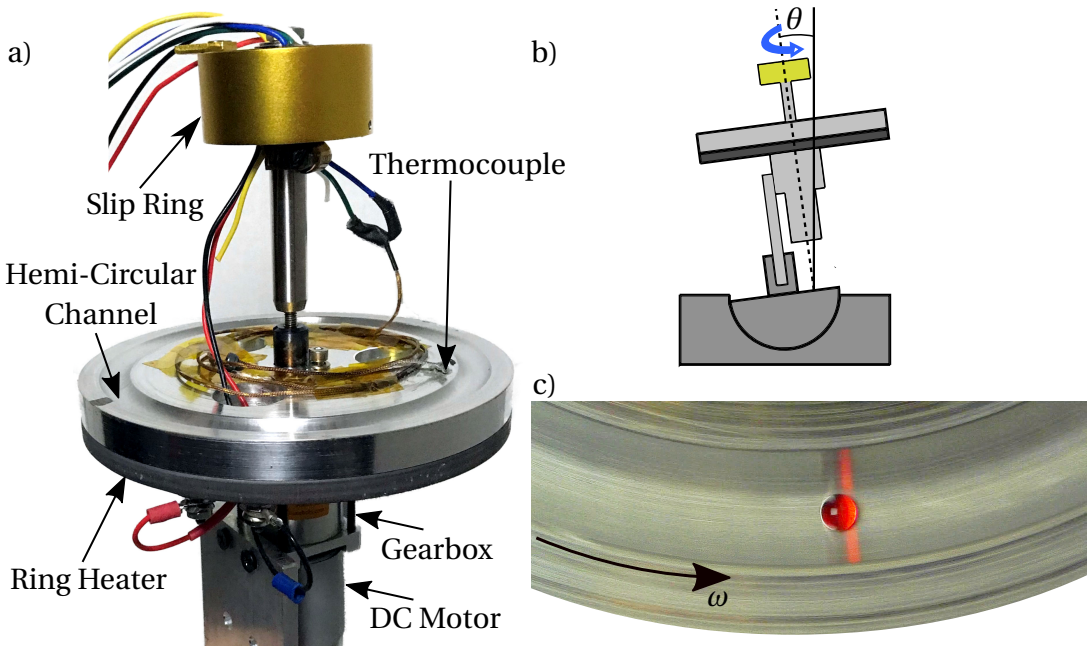

Figure 3.4: a) The rotating heated plate apparatus with respective system components labeled. b) Cross-sectional view of plate mounted to a precision vise tilted at angle θ. c) A droplet of water in the hemi-circular channel heated past the Leidenfrost point of water on aluminum rotating with angular velocity ω.

3.3 Mathematical Model

3.3.1 Dynamic Leidenfrost Droplet Impact in Microgravity: Creeping Flow Limit

We suspect that Leidenfrost behavior will be significantly impacted for low velocity impacts in a low-gravity environment. Thus, we pursue an order of magnitude assessment of the Leidenfrost vapor layer thickness for a free-flying, low-velocity droplet approaching a planar heated substrate well above the Leidenfrost point in a zero-gravity environment. A schematic of the problem is provided in Fig. 3.5. Neglecting drag in the gas phase, the approach of the droplet to the wall is modeled using a force balance where the acceleration of the droplet is set equal to the momentum of evaporation

from the droplet in the direction of the wall; namely,

$$m\ddot{x} = \dot{m}_{evap} u_{vap}, \tag{3.1}$$

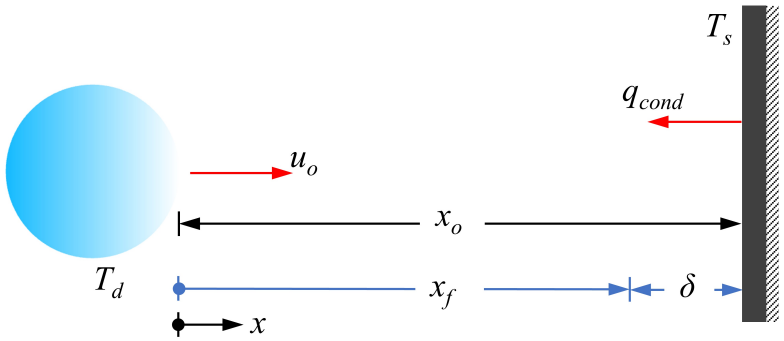

Figure 3.5: A free flying droplet in microgravity with temperature T_d approaching a planar superheated substrate. Laminar convection in the vapor layer is the zeroth-order mode of heat transfer to the droplet. The droplet reaches a final distance x_f before rebounding, separated by a vapor layer δ.

where m is the droplet mass, $\ddot{x}$ is the droplet acceleration toward the planar surface, $\dot{m}_{evap}$ is the mass flow rate of vapor evaporating from the droplet, and u_{vap} is the vapor velocity leaving the droplet. From mass conservation, the vapor velocity may be expressed in terms of vapor mass flow rate, which in turn may be expressed in terms of heat transfer to the droplet q via energy balance $q = \dot{m}_{evap}\left(c_p \Delta T + h_{fg}\right)$, where c_p is the droplet specific heat and ΔT is the difference between the droplet saturation temperature and initial droplet temperature, $\Delta T = T_d - T_o$. From a flow rate balance between droplet velocity u_o and vapor velocity in the squeeze film u_{vap} an expression for the vapor velocity is derived $u_{vap} = (\pi u_o R)/\delta$, where R is the droplet radius and δ is the vapor layer thickness. Assuming a vapor layer thickness of 1 mm for a 5 mL droplet results in $u_{vap} = 0.03$ m/s. This velocity results in order one Reynolds numbers

$\mathrm{Re} = \left(\rho_l u_{vap} \delta\right)/\mu_v$ for the squeeze film flow, where ρ_l is the droplet density and μ_v is the droplet vapor viscosity. The zeroth order mode of heat transfer to the droplet is therefore laminar convection from the heated planar substrate through the vapor layer of the droplet δ, which can be expressed as $\delta = x_o - x$. Assuming constant planar substrate temperature T_s with insulated boundary condition results in constant Nusselt number $\mathrm{Nu} = (hk_v)/\delta$ of 4.86 [160]. Thin film convection through the vapor layer can then be expressed as

$$q = 4.86 k_v A \frac{T_s - T_d}{\delta}, \tag{3.2}$$

where k_v is the droplet vapor conductivity and A is the droplet frontal heat transfer area. The droplet frontal area is computed using an expression for the surface area of a spherical cap at approximately 90% of the total droplet radius resulting in $A = 0.206\pi R^2$. Scaling laws show that outer convection to the droplet and radiation are negligible. Substitution for the vapor velocity and mass flow rate with thin film convection as the sole mode of heat transfer, the governing equation of motion becomes the simple nonlinear ODE

$$m\ddot{x} = \frac{\bar{k}}{(x_o - x)^2}, \tag{3.3}$$

with

$$\bar{k} \equiv \left[\frac{k_v (T_s - T_d)}{c_p \Delta T + h_{fg}}\right]^2 \frac{A}{\rho_v}, \tag{3.4}$$

where ρ_v is the droplet vapor density. Scaling Eq. 3.3 with $x \sim x_f$ and $t \sim x_f/u_o$, and solving for x, a scale expression for the vapor layer thickness is found to be

$$\delta \sim x_o - \frac{2\mathrm{Ep}+1-\sqrt{4\mathrm{Ep}+1}}{\left(2\mathrm{Ep}/x_o\right)}, \tag{3.5}$$

where parameter $\mathrm{Ep} = (x_o m u_o^2)/\bar{k}$, which is a dimensionless ratio of droplet kinetic energy to energy of vaporization and is coined the Evapo-propulsion number. From Eq. 3.5 the vapor layer thickness of a 5 mL droplet of water initially at 20°C travelling at 1 mm/s toward a substrate at 400°C from an initial distance of 100 mm yields $\delta \sim 5.7$ mm an unearthly large thickness 3-orders of magnitude larger than terrestrial thicknesses [132], [149], & [161]. The potentially and comparatively enormous vapor layer thicknesses predicted by Eq. 3.5 for low velocity impacts suggest that low-g droplet flows along conduits, where normal velocities approach zero, are far more likely to remain 'un-impacted' and thus remain 'uncontaminated' when compared to our terrestrial demonstrations. The results suggest a significantly enhanced non-contact nature of the Leidenfrost phenomenon in microgravity.

3.3.2 Rolling Leidenfrost Droplet Lifetime

A simple mathematical model describing the heat transfer from a hot surface to a rolling droplet in the Leidenfrost state on a superheated surface is developed. Figure 3.6 provides a schematic of a perfectly spherical capillary sized droplet with saturation temperature T_d rolling with linear velocity u on a superheated surface with temperature T_s and tilt angle α. The droplet has a radius $r(t)$ that varies with time as it evaporates in the Leidenfrost state in an environment with ambient temperature T_∞. We consider all modes of heat transfer to the rolling droplet, including thin film convection, forced and free outer convection, and radiation. A scale expression is derived for the Leidenfrost vapor layer thickness in gravity from a balance between vapor and

hydrostatic pressures for a capillary sized droplet resulting in

$$\delta \sim \left(\frac{\mu_v k_v \Delta T_1}{2\rho_l \rho_v g \left(c_p \Delta T_2 + h_{fg} \right)} \right)^{1/3}, \tag{3.6}$$

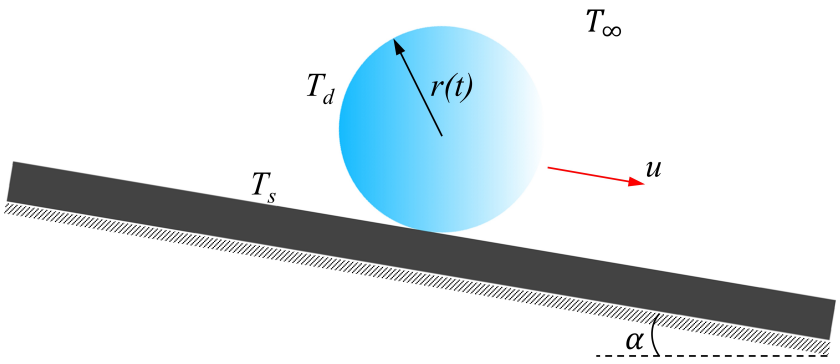

Figure 3.6: A droplet rolling with linear velocity u on a heated tilted substrate well in excess of the Leidenfrost point.

where μ_v is the droplet vapor viscosity, ρ_l is the liquid droplet density, ρ_v is the droplet vapor density, g is gravitational acceleration, $\Delta T_1 = T_s - T_d$ is the difference between plate temperature and droplet saturation temperature, and $\Delta T_2 = T_d - T_o$ is the difference between droplet saturation temperature and initial droplet temperature. Assuming a planar droplet surface at the droplet substrate interface and balancing vapor pressure with viscous forces where vapor pressure is expressed in terms of the droplet hydrostatic pressure a scale expression for the vapor velocity is derived $u_{vap} \sim \left(2\rho_l g \delta^2\right)/\mu_v$. The Reynolds number is computed for the vapor flow suggesting laminar flow in the vapor layer. Assuming constant planar substrate temperature with insulated boundary condition the Nusselt number is again determined to be constant and equal to 4.86 [160]. Using Eq. 3.6 and taking the droplet heat transfer area to be the projected spherical cap area at approximately 90% of the droplet radius, an expres-

sion for steady thin film convection through the vapor layer to the droplet can then be expressed as

$$q_c = \pi r^2 \left(k_v \Delta T_1\right)^{2/3} \left(2\rho_l \rho_v g \left(c_p \Delta T_2 + h_{fg}\right) {\mu_v}^{-1}\right)^{1/3}. \tag{3.7}$$

In this case, order of magnitude comparisons suggests that thin film convection and outer droplet forced convection are significantly more relevant than free convection and radiation. The outer convective heat transfer coefficient is estimated using the Whitaker correlation [162] for the average Nusselt number for a sphere. From Newton's law of cooling, an expression for outer forced convective heat transfer to the droplet is expressed as

$$q_{fc} = 2\pi r k_a \Delta T_3 \left[2 + \left(0.4\left[Rr\right]^{1/2} + 0.06\left[Rr\right]^{2/3}\right) \mathrm{Pr}^{0.4} \left(\frac{\mu_\infty}{\mu_s}\right)^{1/4}\right], \tag{3.8}$$

where $R \equiv \left(2\rho_a u\right)/\mu_a$, and k_a, μ_a, and ρ_a are the respective air thermal conductivity, dynamic viscosity, and density. Velocity u is that of the droplet, Pr the Prandtl number of air, μ_∞ the air free stream dynamic viscosity, μ_s the air dynamic viscosity at plate surface temperature T_s and $\Delta T_3 = T_d - T_a$ is the difference between droplet saturation temperature T_d and air free stream temperature T_a. All properties for air are taken at the bulk temperature $T_b = \left(T_s + T_\infty\right)/2$. The mass rate of change for an evaporating spherical droplet can be expressed as

$$\dot{m} = -4\pi\rho_l r^2 r_t, \tag{3.9}$$

where r_t is the time rate of change of the droplet radius. The evaporative mass flowrate can be expressed in terms of the total heat transfer to the droplet using the expression

$q = \dot{m}\left(c_p \Delta T + h_{fg}\right)$, substitution into which Eqs. 3.7 - 3.9 yield a first order non-linear ODE describing the droplet lifetime

$$r_t + \frac{k_a}{2\rho_l\left(c_p\Delta T_2 + h_{fg}\right) r}\Delta T_3 \left[2 + r^{1/2}\left(0.4R^{1/2} + 0.06R^{2/3}r^{1/6}\right)\mathrm{Pr}^{0.4}\left(\frac{\mu_\infty}{\mu_s}\right)^{1/4}\right] + \\ +1/4\left(\frac{k_v \Delta T_1}{\rho_l \mu_v^{1/2}\left(c_p\Delta T_2 + h_{fg}\right)}\right)^{2/3}\left(2\rho_v g\right)^{1/3} = 0. \tag{3.10}$$

Eq. 3.10 is solved numerically for droplets of capillary size or smaller with initial droplet radius condition $r\,(t=0) = R_o$, predicting the overall rolling droplet lifetime on a heated surface with constant velocity in the Leidenfrost state.

For droplets that are larger than the capillary length-scale, $L_\mathrm{c} = \left(\sigma/\rho_l g\right)^{1/2}$, where σ is the fluid surface tension, a second droplet evaporation rate model is developed. We consider the schematic shown in Fig. 3.7 showing a droplet slightly larger than the capillary length-scale with saturation temperature T_d rolling with linear velocity u on a superheated surface with temperature T_s and tilt angle α. The droplet has radius $r(t)$ that varies with time as it evaporates in the Leidenfrost state in an environment with ambient temperature T_∞. The droplet has a constant height that is equal to two times the capillary length in the Leidenfrost state, $H = 2L_\mathrm{c}$. We again consider thin film convection and forced outer convective heat transfer to the droplet. A scale expression is derived for the Leidenfrost vapor layer thickness in gravity from a balance between vapor and hydrostatic pressures resulting in,

$$\delta \sim \left(\frac{\mu_v k_v \Delta T_1 r}{2\rho_l \rho_v g\left(\frac{\sigma}{\rho_l g}\right)^{1/2}\left(c_p\Delta T_2 + h_{fg}\right)}\right)^{1/3}. \tag{3.11}$$

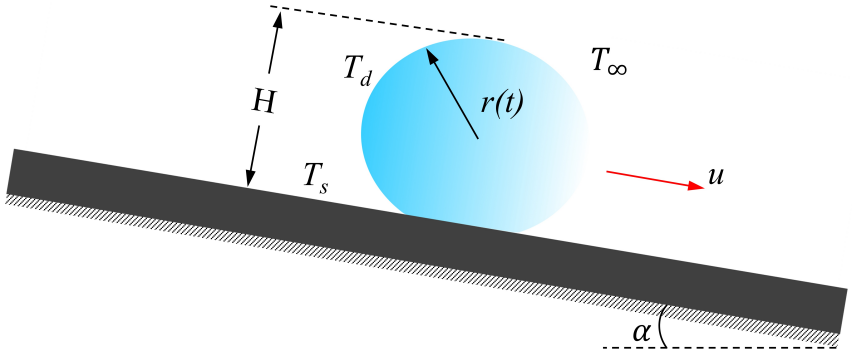

Figure 3.7: A droplet larger than the capillary length-scale rolling with linear velocity u on a heated tilted substrate well in excess of the Leidenfrost point.

Steady thin film convective heat transfer to the droplet through the vapor layer is developed similar to the capillary sized droplet case now using Eq. 3.11 and is expressed as

$$q_c = \pi r^{5/6} \left(k_v \Delta T_1\right)^{2/3} \left(2\rho_v \left(\rho_l g \sigma\right)^{1/2} \left(c_p \Delta T_2 + h_{fg}\right) {\mu_v}^{-1}\right)^{1/3}. \tag{3.12}$$

Leidenfrost droplets slightly larger than the capillary length-scale are assumed to be nearly spherical. The outer forced convective heat transfer coefficient is therefore estimated using the Whitaker correlation [162] for the average Nusselt number for a sphere. The droplet frontal area is assumed to be a circular projection of the droplet height, $H = 2L_c$ in the domain where the droplet is slightly larger than the capillary length-scale. From Newton's law of cooling, an expression for outer forced convective heat transfer to the droplet is expressed as

$$q_{fc} = 2\pi k_a L_c \Delta T_3 \left[2 + L_c^{1/2} \left(0.4R^{1/2} + 0.06R^{2/3} L_c^{1/6}\right) \mathrm{Pr}^{0.4} \left(\frac{\mu_\infty}{\mu_s}\right)^{1/4}\right]. \tag{3.13}$$

Order of magnitude comparisons again suggest that thin film convection and forced outer convection are significantly more relevant than free convection and radiation. Again using the expression for mass flowrate in terms of the total heat transfer to the droplet as $q = \dot{m}\left(c_p \Delta T + h_{fg}\right)$ and substitution of Eqs. 3.9, 3.12, and 3.13 yields a first order non-linear ODE describing the droplet lifetime for a Leidenfrost droplet with $r(t) > L_{\mathrm{c}}$,

$$r_t r^2 + \frac{k_a L_{\mathrm{c}}}{2\rho_l\left(c_p \Delta T_2 + h_{fg}\right)} \Delta T_3 \left[2 + L_{\mathrm{c}}^{1/2}\left(0.4R^{1/2} + 0.06R^{2/3}L_{\mathrm{c}}^{1/6}\right)\mathrm{Pr}^{0.4}\left(\frac{\mu_\infty}{\mu_s}\right)^{1/4}\right] + \\ + \frac{1}{4} r^{5/6}\left(\frac{k_v \Delta T_1}{\left(c_p \Delta T_2 + h_{fg}\right)}\right)^{2/3}\left(\frac{2\rho_v g}{\mu_v \rho_l^2} L_{\mathrm{c}}\right)^{1/3} = 0. \tag{3.14}$$

Eq. 3.14 describes the evaporation of a dynamically rolling Leidenfrost droplet larger than the capillary length-scale with initial droplet radius condition $r\,(t=0) = R_o$. Evaporating droplets will inevitably reduce down to capillary sized droplets. In this regime, L_{c} in Eq. 3.14 becomes $r(t)$ and Eq. 3.14 becomes Eq. 3.10. Therefore, in order to obtain droplet lifetimes for Leidenfrost droplets larger than the capillary length, Eq. 3.14 and Eq. 3.10 are both solved numerically where Eq. 3.14 is solved in the domain $L_{\mathrm{c}} < r(t) \leq R_o$ and Eq. 3.10 is solved from $0 \leq r(t) \leq L_{\mathrm{c}}$. Numerical results from Eq. 3.14 and Eq. 3.10 are compared to the experimentally measured Leidenfrost droplet lifetimes for droplets of varying initial radius, droplet velocities, and surface temperatures. Solutions to Eq. 3.10 and Eq. 3.14 provide Leidenfrost droplet evaporation rates and lifetimes, both of which are useful for sizing a Leidenfrost droplet distiller.

3.4 Results and Discussion

3.4.1 Microgravity

High Velocity Leidenfrost Impacts

Microgravity Leidenfrost droplet impact experiments are conducted with droplet impacts at various Weber numbers We = $\left(\rho u^2 D\right)/\sigma$, impact angles, surface temperature, surface wettability, and surface geometry. Figure 3.8 shows a series of images taken at 15 Hz for a 1.3 mL droplet of water impacting a superhydrophobic substrate held at 140°C in microgravity. A Logan Shooter is used to eject the water droplet free of oscillations toward the heated substrate with a normal velocity of 13.0 cm/s and a perpendicular impact Weber number of 3.1. The droplet impacts the substrate and elastically rebounds without undergoing nucleate boiling.

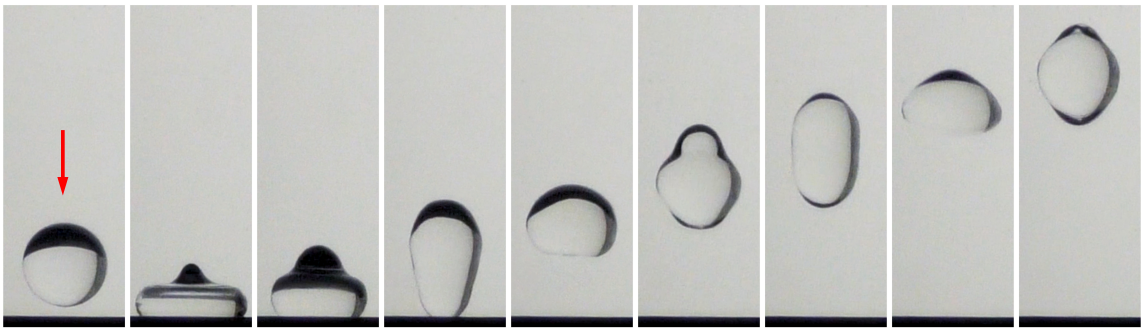

Figure 3.8: A sequence of images taken at 15 Hz of a 1.3 mL water droplet impacting a superhydrophobic substrate held at 140°C in microgravity. The droplet is ejected out of a Logan Shooter, free of oscillations, normal relative to the surface at a velocity of 13.0 cm/s with a normal impact Weber number equal to 3.1.

A series of low-g dynamic Leidenfrost impact experiments are shown in Fig. 3.9 where oscillation-free water droplets are ejected from a Logan Shooter toward heated

substrates. Figures 3.9a and 3.9b show a series of images taken at 6 Hz from impacts on polished aluminum at 206°C and a superhydrophobic surface at 142°C. Incoming impact angles are 45° and perpendicular Weber numbers are 1.9 for both experiments. Elastic rebounds are observed in both experiments with outgoing impact angles of 42° and 45° for the impact on the aluminum and superhydrophobic plates, respectively. It is clear from such demonstrations that for fixed impact Weber number, superhydrophobic surfaces drastically reduce the dynamic Leidenfrost point in microgravity.

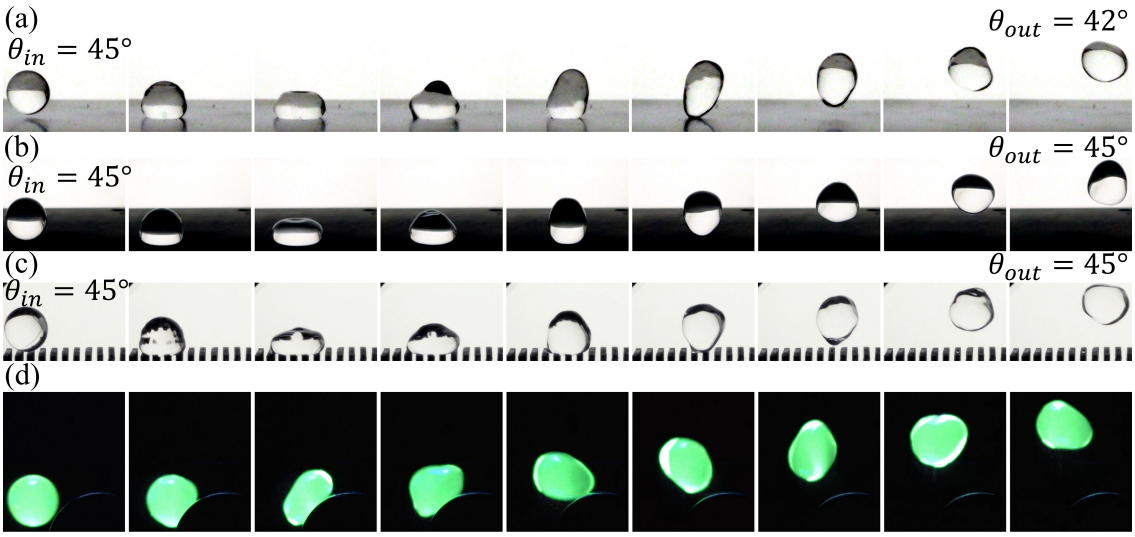

Figure 3.9: Sequence of images of oscillation-free water droplet impacts for droplets ejected using a Logan Shooter. (a) Sequence of 6 Hz images of a 12.6 cm/s 1.1 mL droplet impact at 45° on a polished aluminum substrate at 206°C, rebound angle is 42° likely due to viscous drag on impact. (b) 12.3 cm/s 1.2 mL droplet impacting a superhydrophobic surface at 142°C, rebound angle is 45°. (c) 13.2 cm/s 1.0 mL droplet impacting a superhydrophobic array of 0.9 mm diameter circular pillars and 0.8 mm spacing at 140°C, rebound angle is 45°. (d) 12 Hz images of 10.4 cm/s 1.5 mL droplet painted with UV fluorescent dye impacting a 9.5 mm diameter stainless-steel cylinder at 465°C.

Figure 3.9c shows images taken at 6 Hz for a droplet impacting a superhydrophobic array of circular pillars, held at 140°C with pillar diameters of 0.9 mm and pillar spac-

ings of 0.8 mm. The incoming and outgoing impact angles are observed to be 45° with perpendicular impact Weber number of 2.1. An elastic rebound is observed free of nucleate boiling. The droplet impact in Fig. 3.9c results in a droplet with higher mode oscillations on the surface of the droplet after impact compared to the aluminum surface rebound (3.9a) and superhydrophobic plate impact (3.9b) due to droplet deformation into the pillar gaps during impact. Figure 3.9d shows a series of images taken at 12 Hz of a 1.5 mL droplet of water painted with UV dye impacting a stainless-steel cylinder with a Weber number of 2.1. The cylinder is 9.5 mm in diameter at 465°C. The droplet impacts and rebounds from the cylinder elastically initiating a degree of rotation.

Low-gravity Leidenfrost droplet impact experiments between two parallel plates were also conducted. Shown in Fig. 3.10 are image overlays from three experiments taken at 30 Hz of 1 mL water droplets ejected with a Logan Shooter into two parallel plates separated by a distance of 13.5 mm with overall length of 127 mm. Figure 3.10a is a water droplet bouncing between two superhydrophobic plates at room temperature with initial velocity of 31.9 cm/s and final velocity of 23.2 cm/s. The sum of incident and reflection angles $\theta_i + \theta_R$ increases from 93° to 100° over the course of five bounces. Figure 3.10b shows the same experiment, but with heated superhydrophobic plates, with the top and bottom plates at 168°C and 183°C, respectively. Droplet velocity decreases from 25.1 cm/s to 21.1 cm/s and the sum of incident and reflection angles decrease from 103° to 97° over the course of five bounces. Figure 3.10c shows the same experiment as in Fig. 3.10a and 3.10b, but with superheated polished aluminum surfaces with top and bottom plates held at 305°C and 366°C, respectively. Droplet velocity decreases from 26.7 cm/s to 15.6 cm/s and the sum of incident and reflection angles decrease from 110° to 84° over the course of five bounces. The heated

plate experiments, unlike the non-heated plate experiment, observed decreases in the sum of incident and reflection angles. The experiment in Fig. 3.10c displays a greater decrease compared to the heated superhydrophobic plate experiment in Fig. 3.10b likely due to increased Leidenfrost vapor recoil forces, which propel the droplets in a predominately perpendicular direction to the substrates. A larger decrease in the sum of incident and reflection angles are due to the larger vapor recoil forces. In the absence of gravity, the Leidenfrost vapor recoil force plays a more controlling role in the droplet behavior which may be exploited in practical systems design for spacecraft.

Leidenfrost Fluid Transport in Conduits

Low-g Leidenfrost experiments investigating fluid transport in circular conduits with bends were performed. Figure 3.11a shows 17 Hz images of an experiment where blue-dyed ethanol droplets are ejected using the passive capillary ejection method (ref. Fig. 3.2). The 60 mm long 9 mm ID glass tube ejector with converging nozzle of 1.5 mm ID exit was used. The glass receiving tube has a 45° bend at the outlet and is heated to > 360°C. The glass tube has an 8.5 mm ID and is 63 mm in length. Ejected droplet diameters are 1.9 mm, with the largest velocity droplet ejected at 38.4 cm/s resulting in We = 10. Elastic Leidenfrost impacts are observed and the droplets successfully traverse the conduit and exit without wetting/touching any surfaces. Figure 3.11b shows 15 Hz images of a similar test where ethanol is ejected from the same nozzle as in Fig. 3.11a, but into a glass tube with 180° bend. This tube has a 4 mm ID and 64 mm length and is heated to > 360°C. Droplets ejected into the tube are 1.8 mm in diameter with the largest velocity of 41.6 cm/s, resulting in We = 11. All droplets rebound elastically in the Leidenfrost state, traversing the bend and exiting the tube without wetting any sur-

faces. Figure 3.11c shows 17 Hz images of a pressure driven jet of blue-dyed ethanol from a 20-gauge needle, which breaks up via the Plateau-Rayleigh instability into a stream of droplets. This droplet stream is ejected into the same glass tube as in Fig. 3.11b, heated to > 360°C. The ejected droplets have maximum diameters of 2.6 mm and average velocity of 22.0 cm/s, resulting in We = 4.5. The entire stream of droplets traverses the bend and exits the conduit without contact, wetting or nucleate boiling.

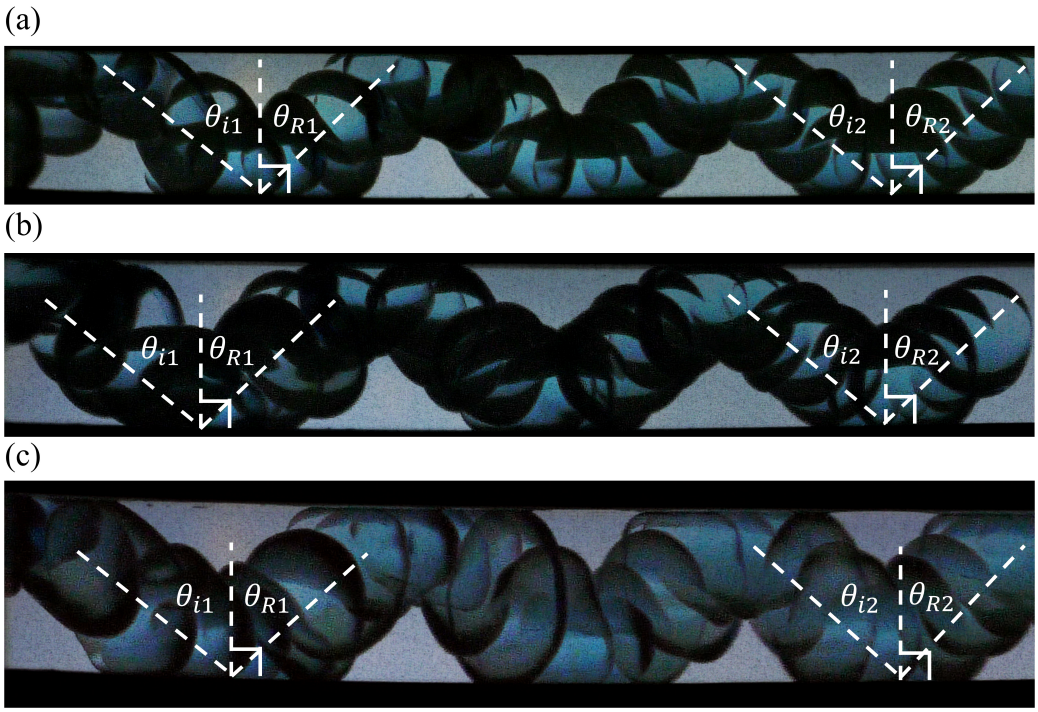

Figure 3.10: 30 Hz overlay images of 1 mL water droplets ejected in low-g with a Logan Shooter bouncing 5 times between parallel plates. The 127 mm long plates are separated by a distance of 13.5 mm. (a) Two superhydrophobic plates at room temperature: velocity decreases from 31.9 cm/s to 23.2 cm/s and $\theta_i + \theta_R$ increase from 93° to 100°. (b) Two heated superhydrophobic plates with the top and bottom plates at 168°C and 183°C, respectively. Droplet velocity decreases from 25.1 cm/s to 21.1 cm/s and $\theta_i + \theta_R$ decrease from 103° to 97°. (c) Two polished aluminum plates with top and bottom plates at 305°C and 366°C, respectively. Droplet velocity decreases from 26.7 cm/s to 15.6 cm/s and $\theta_i + \theta_R$ decrease from 110° to 84°.

Figure 3.11: Microgravity Leidenfrost droplet experiments in glass tubes. (a) Passive capillary ejection of blue-dyed ethanol droplets: 17 Hz images of 38.4 cm/s, 1.9 mm droplets into an 8.5 mm ID 63 mm long glass tube bent 45° at one end and held at > 360°C. (b) 15 Hz images of 41.6 cm/s, 1.8 mm ethanol ejected into 4.0 mm ID, 63 mm long tube with 180° bend. (c) 17 Hz images of a pressure driven ethanol jet ejected from a 20-gauge needle into the glass tube of (b), producing 2.6 mm droplets at average velocity 22 cm/s.

Ethanol Leidenfrost jet experiments in microgravity are conducted in coiled glass tubing. Figure 3.12 shows 60 Hz overlay images for three experiments where jets of ethanol are ejected into the superheated 6 mm ID glass coiled on an 85 mm OD at > 360°C. The pressure-driven ethanol jets are again ejected through a 20-gauge syringe. Figure 3.12a shows an overlay of a test where the jet is ejected into the superheated glass coil with an open inlet. The jet breaks up into a stream of droplets that traverse the coil bends in the non-contact Leidenfrost mode. Droplets exit out of the outlet of the coil as identified by the red arrow. However, a buildup of droplets is observed near

the inlet of the coil caused by vapors produced expanding both up and down stream, effectively halting the flow. When the inlet is sealed, as is the case in Fig. 3.12b, the ethanol jet evenly distributes throughout the coil and no buildup of fluid in the coil at the inlet is observed, the vapors produced propelling the droplets downstream and out of the coil. In Fig. 3.12c the same test is conducted, but with the addition of a 5.5 Lpm airflow through the coil and an open inlet. An even distribution of droplets is observed as in the experiment shown in Fig. 3.12b where no droplet buildup occurs. Such demonstrations provide ready examples of how essentially passive non-contact droplet delivery and Leidenfrost transport methods can be achieved in conduits. Based on such tests, a prototypical distillation system may require as little as ~15 m length of tubing for complete distillation.

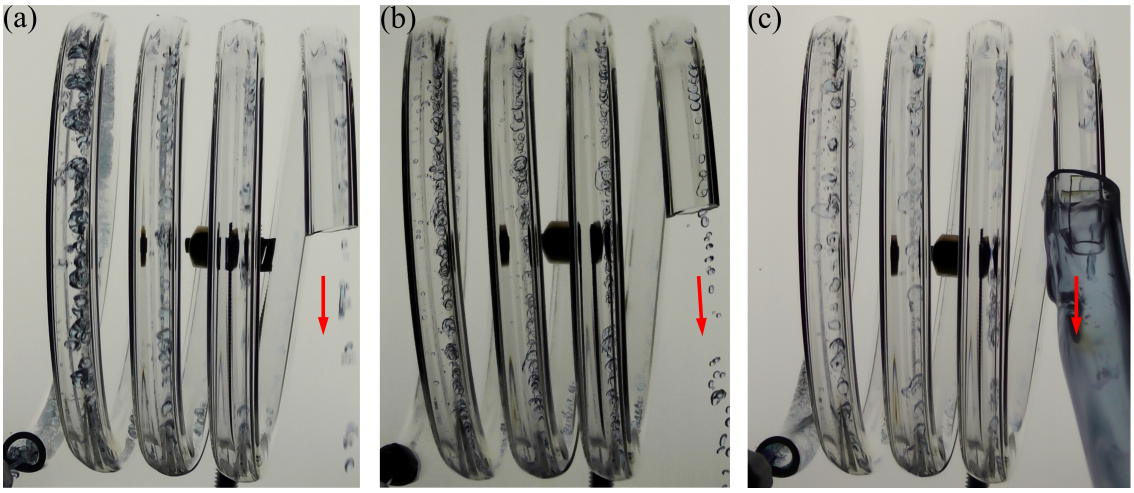

Figure 3.12: 60 Hz overlay images for three drop tower tests where jets of dyed ethanol are ejected into a 6 mm ID glass coil with OD of 85 mm at > 360°C: (a) Jet of ethanol ejected into a superheated glass coil with an open inlet and no airflow, (b) jet ejected with a plugged inlet and no airflow, and (c) jet ejected with open inlet and 5.5 Lpm airflow.

Low Velocity Leidenfrost Impact

Low velocity Leidenfrost droplet impact experiments in microgravity were conducted. Weber numbers on the order of 10^{-4} or less are desired to produce millimetric vapor layer thicknesses predicted in Eq. 3.5 for low velocity Leidenfrost impacts. Ethanol and liquid nitrogen are used in these demonstration experiments for their relatively low specific heat and latent heat of vaporization. Liquid nitrogen is of particular interest for such experiments due to its low saturation temperature -195.8°C making room temperature surfaces Leidenfrost temperature surfaces.

Passive capillary ejection of ethanol droplets into a converging nozzle toward heated surfaces at low impact angles were performed in microgravity. Figure 3.13 shows 120 Hz image overlays of a 1.9 mm ejected droplet of ethanol impacting a superheated plate at 400°C. The incoming velocity and angle of the droplet are 11.7 cm/s and 2.3°, respectively, resulting in perpendicular impact speed and perpendicular Weber number of 4.7 mm/s and 0.0015, respectively. The outgoing speed and angle are 11.4 cm/s and 7.6°, respectively, with perpendicular exit velocity of 15.1 mm/s. The three-fold increase in perpendicular velocity from pre- to post-impact suggests the magnitude of acceleration induced by droplet vaporization, which is readily detected. This force may be used to solve inversely for the evaporation rates for a more quantitative assessment of the assumptions leading to Eq. 3.5. Further analytical comparisons will be reported at a later date.

To further investigate vapor recoil forces impacting Leidenfrost phenomena in low-g environments, a series of drop tower tests were conducted to establish perpendicular Weber numbers ~10^{-4} or less, where droplets of liquid nitrogen are ejected parallel to a superheated substrate. Liquid nitrogen droplets are ejected using an aluminum

Logan Shooter, where the non-wetting function is performed by the Leidenfrost vapor layer for liquid nitrogen instead of superhydrophobic surfaces for water, as was demonstrated in Fig. 2.9. Figure 3.14 shows 120 Hz overlay images of a liquid nitrogen droplet ejected nearly parallel to a heated surface at 450°C. The 1.7 mm droplet is ejected at a speed of 60.6 cm/s at an approximately 0.2° impact angle. The ejection location is 2.7 mm above the planar heated substrate. The droplet traverses over the heated surface for a 0.61 s duration. While traversing the surface, the drop is redirected away from the surface to a distance of 3.9 mm after 370 mm of travel. The total deflection caused by vapor recoil forces is δ = 1.2 mm. In this case Ep = 0.8, indicating vapor recoil forces are somewhat larger than inertial forces. From the scale expression of Eq. 3.5, we estimate a vapor layer thickness of 1.6 mm for this outcome, which is in fair agreement with the experimental observations.

Figure 3.13: A 120 Hz image overlay of a 1.9 mm droplet of ethanol with incoming velocity, u_i, of 11.7 cm/s and incoming, θ_i, and outgoing angles, θ_e, of 2.3° and 7.6°, respectively. Normal impact Weber number was found to be $1.5 * 10^{-3}$. Incoming and outgoing normal velocities were found to be 4.7 mm/s and 15.1 mm/s, respectively.

3.4.2 Terrestrial Leidenfrost Droplet Distillation

Superhydrophobic Channel

To estimate droplet residence time in a 'Leidenfrost distiller,' droplet lifetime experiments are conducted using the rotating, heated, superhydrophobic Leidenfrost chan-

nel apparatus described in Section 3.2.3. The capillary-sized droplets of distilled water with initial volume ~ 0.029 mL are deployed in the superhydrophobic channel held at 170°C. Figure 3.15 provides a plot of droplet lifetimes as a function of linear droplet velocity for various plate tilt angles. Also plotted are the droplet lifetime results from numerical solutions to Eq. 3.10.

Figure 3.14: 120 Hz image overlay for a 1.7 mm liquid nitrogen droplet ejected at 60.6 cm/s from a Logan Shooter, nearly parallel to a planar surface at 450°C. The droplet has an impact angle of ~ 0.2°, and is ejected 2.7 mm away from the wall, before being propelled upward due to vapor recoil forces and ending up 3.9 mm from the wall. Measured vapor layer thickness is 1.2 mm.

The experimental results show a general decrease in droplet lifetime for all tilt angles as droplet velocity is increased due to increases in convective heat transfer. This trend is captured in the analytical results as well. For the same droplet velocity, droplet lifetime decreases as tilt angle is increased. This is due to increased droplet contact area with the heated plate due to the semi-circular cross-sectional geometry of the heated channel. Thin film convection is the dominant mode of heat transfer and as a result, increased contact area plays a large role in determining the droplet lifetime. This is not captured in the analysis since the solution for the droplet lifetime assumed a droplet rolling on a flat surface. Overall, the analytical model predicts droplet lifetimes reasonably well for tilt angles of 15° or lower, with maximum deviation of ± 30% for all experimental results conducted.

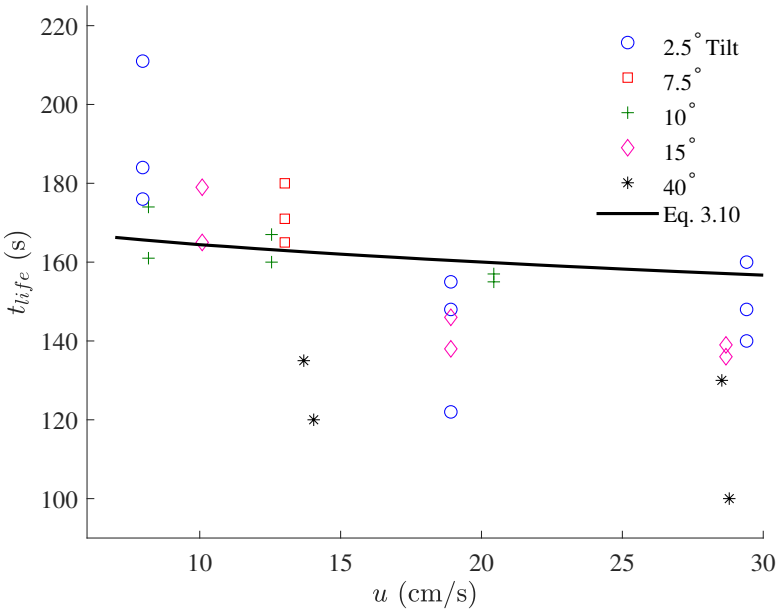

Figure 3.15: Droplet lifetime vs. droplet velocity for ~ 0.029 mL droplets of distilled water in a superhydrophobic semi-circular channel at 170°C at varying tilt angles, with comparisons to analytical model of Eq. 3.10.

To demonstrate temperature, pressure, and concentration effects, droplet distillation experiments are conducted using the same apparatus but employing flat beer, urine, and 25 g/L aqueous solutions of NaCl, KCl, and sugar. Controlled solute-solvent separation is also observed for all fluids used. An example of solute-solvent separation was shown in Fig. 3.3 for separation of water and NaCl. Deposition of solutes on the superhydrophobic surface was observed. The surface was fouled from the dissolved solutes in solutions precipitating out of solution near the end of all tests performed. The ability to clean the heated superhydrophobic surface from deposited solutes from the various solutions is easily demonstrated, exploiting the 'self-cleaning' nature of such surfaces. For example, dispensing a droplet of water into the rotating channel readily re-dissolves the solutes, cleaning the surface, and recovering the superhydrophobic

characteristics of the surface to pre-experiment conditions. These observations again demonstrate additional favorable attributes for a Leidenfrost distillation system promoting non-contact distillation.

Aluminum Channel

To understand the influence of surface temperature, initial droplet diameter, and linear droplet velocity, the aluminum channel apparatus described in Section 3.2.3 was utilized to perform a suite of Leidenfrost droplet distillation experiments. Figure 3.16 shows experimental Leidenfrost droplet lifetimes plotted against droplet velocity for water droplets with initial diameter d_o of 5.08 mm ± 0.05 mm on an aluminum surface at temperatures of 200°C, 225°C, and 250°C tilted at 10°. For constant droplet velocity, increases in surface temperature decrease droplet lifetime. At constant surface temperature, increases in droplet velocity decrease droplet lifetime resulting from increased forced convection. Figures 3.17, 3.18, and 3.19 show Leidenfrost droplet lifetimes plotted against droplet velocity for water droplets of varying initial diameter on an aluminum surface held at temperatures of 200°C, 225°C, and 250°C, respectively, with tilt angle of 10°. Across all temperatures and for all droplet sizes, increased droplet velocity results in decreasing droplet lifetime. For constant temperature and droplet velocity, increasing initial droplet diameter increases the droplet lifetime. Also plotted on Figs. 3.17, 3.18, and 3.19 are results from numerical solutions to Eq. 3.10 and Eq. 3.14. For the 200°C surface temperature case, numerical results predict Leidenfrost droplet lifetime with good agreement for droplets with d_o = 2.54 mm ± 0.03 mm, while results for droplets with d_o = 5.08 mm ± 0.05 mm and d_o = 7.64 mm ± 0.08 mm are order-of-magnitude accurate. The trend of decreasing droplet lifetime with increasing

droplet velocity is captured for all droplet diameters.

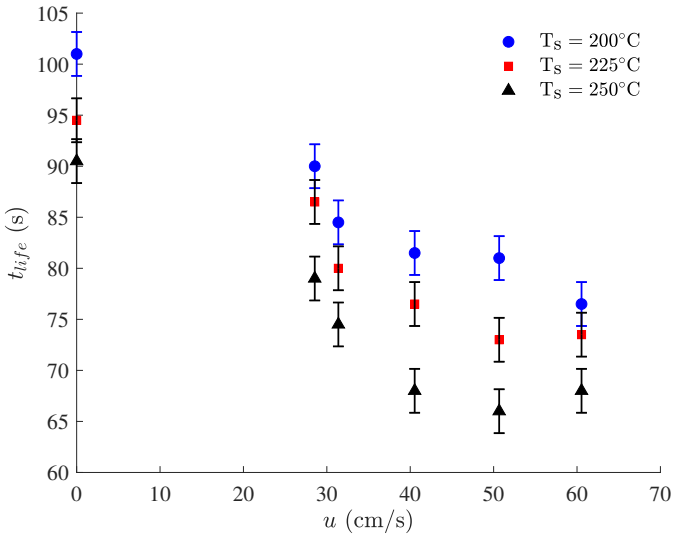

Figure 3.16: Droplet lifetime vs. droplet velocity for water droplets with initial diameter d_o = 5.08 mm ± 0.05 mm droplet on an aluminum surface with 10° tilt angle at temperatures of 200°C, 225°C, and 250°C. Uncertainties in droplet velocity are smaller than marker sizes.

Droplet lifetime results for the 225°C case in Fig. 3.18 show silimar results to the 200°C case where droplet lifetimes are predicted with good accuracy for initial droplet diameters of 2.54 mm ± 0.03 mm. Results for d_o = 5.08 mm ± 0.05 mm and d_o = 7.64 mm ± 0.08 mm are order-of-magnitude accurate with noticeably increased model accuracy when compared to the 200°C results in Fig.3.17. Droplet lifetime trends are captured in this case for increasing droplet velocities across all droplet diameters. Similar results are observed for the 250°C plate temperature case shown in Fig. 3.19 with even more noticable numerical model accuracy for dropelts of d_o = 5.08 mm ± 0.05 mm and d_o = 7.64 mm ± 0.08 mm compared to the 200°C and 225°C cases.

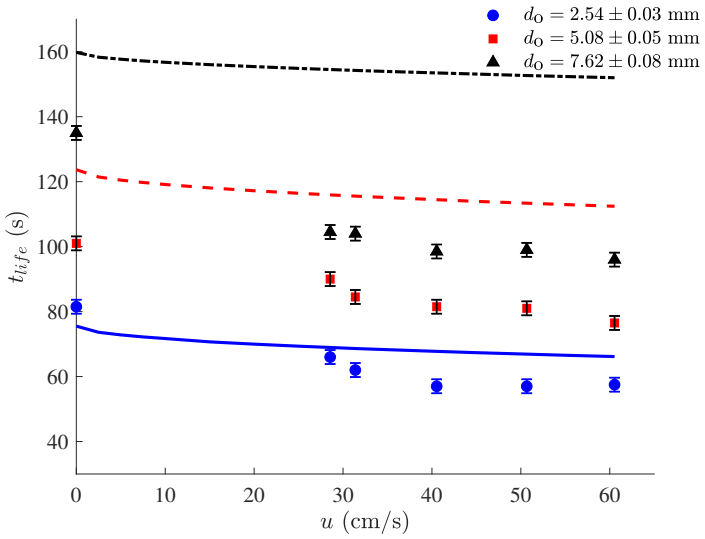

Figure 3.17: Experimental droplet lifetime results plotted against droplet velocity for water droplets of varying initial diameter on a 200°C aluminum surface with 10° tilt angle. Numerical droplet lifetime results from Eq. 3.10 and Eq. 3.14 are also plotted. Uncertainties in droplet velocity are smaller than marker sizes.

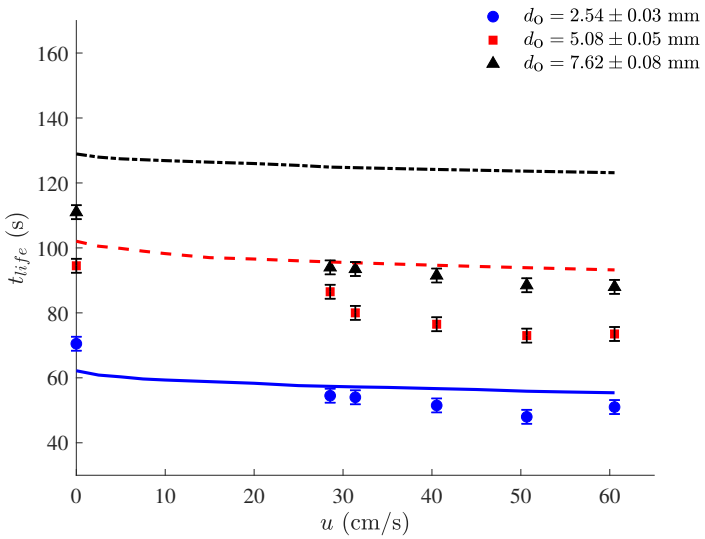

Figure 3.18: Experimental droplet lifetime results plotted against droplet velocity for water droplets of varying initial diameter on a 225°C aluminum surface with 10° tilt angle. Numerical droplet lifetime results from Eq. 3.10 and Eq. 3.14 are also plotted. Uncertainties in droplet velocity are smaller than marker sizes.

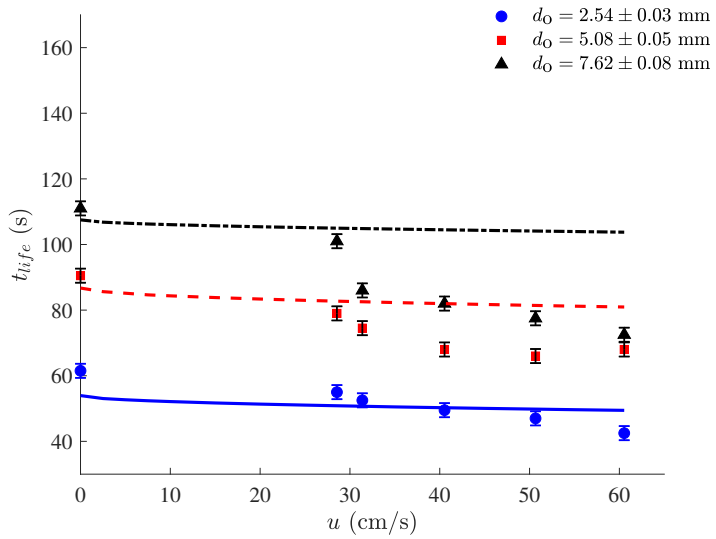

Figure 3.19: Experimental droplet lifetime results plotted against droplet velocity for water droplets of varying initial diameter on a 250°C aluminum surface with 10° tilt angle. Numerical droplet lifetime results from Eq. 3.10 and Eq. 3.14 are also plotted. Uncertainties in droplet velocity are smaller than marker sizes.

Figures 3.20, 3.21, and 3.22 show normalized droplet lifetime results plotted against normalized droplet velocity for the aluminum surface held at temperatures of 200°C, 225°C, and 250°C, respectively, with tilt angle of 10°. Experimental droplet lifetimes are normalized by numerical droplet lifetimes solved in the limit of zero convective heat transfer. As surface temperatures increase, maximum deviation between numerical and experimental results decrease from ~ 40% for the 200°C case to ~ 30% in the 250°C case. This effect is likely due to increased dominance of thin film convective heat transfer relative to natural convection with increasing surface temperature. To assess this effect, the ratio of natural convection heat transfer to thin film convective heat transfer to the droplet is computed using, $q_{NC}/q_C = h_{NC}\delta\Delta T_3/k_v\Delta T_1$. The natural convective heat transfer coefficient is computed from the correlation for the Nusselt number of an inclined hot plate developed by Fujii and Imura [163], $\mathrm{Nu} = 0.56(\mathrm{GrPr})^{1/4}$, where

Gr is the Grashoff number, Gr = $L_c^3 g\beta\,(T_s - T_\infty)\,cos\theta/\nu^2$, L_c is the ratio of the top plate area and plate perimeter A/p, β is the thermal expansion coefficient for air, T_s is the plate temperature, T_∞ is the ambient air temperature, ν is the kinematic viscosity for air, and θ is the plate tilt angle. All air properties are evaluated at the bulk temperature $T_b = (T_s + T_\infty)/2$. Results for $q_{\mathrm{NC}}/q_{\mathrm{C}}$ at plate temperatures of 200°C, 225°C, and 250°C are 0.45, 0.037, and 0.0,3 respectively. This indicates increased dominance of thin film convective heat transfer relative to natural convection, which is a higher-order effect not accounted for in the mathematical models.

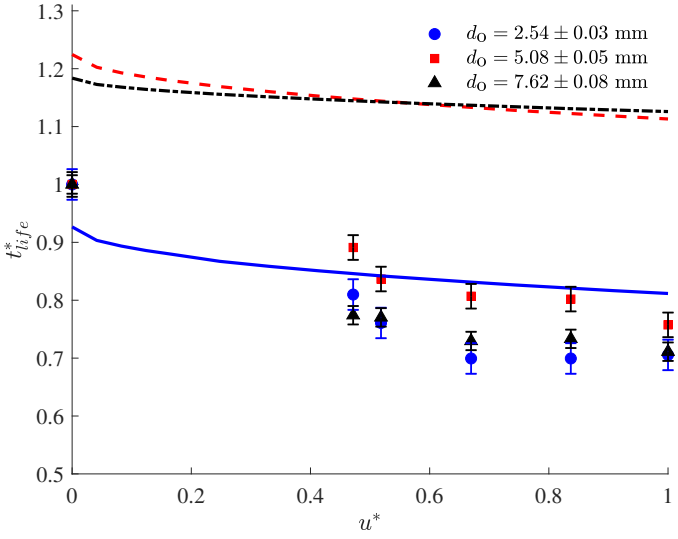

Figure 3.20: Normalized droplet lifetime plotted against droplet velocity for water droplets of varying initial diameter on a 200°C aluminum surface with 10° tilt angle. Normalized numerical droplet lifetime results from Eq. 3.10 and Eq. 3.14 are also plotted. Uncertainties in droplet velocity are smaller than marker sizes.

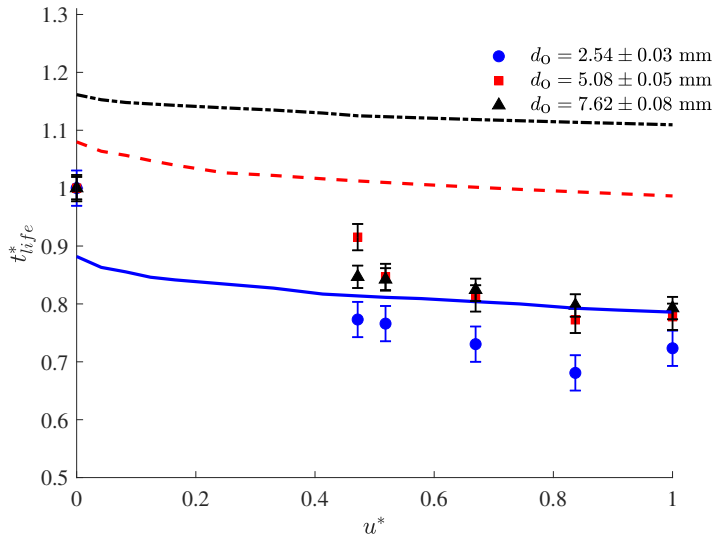

Figure 3.21: Normalized droplet lifetime plotted against droplet velocity for water droplets of varying initial diameter on a 225°C aluminum surface with 10° tilt angle. Normalized numerical droplet lifetime results from Eq. 3.10 and Eq. 3.14 are also plotted. Uncertainty in velocity is smaller than marker sizes.

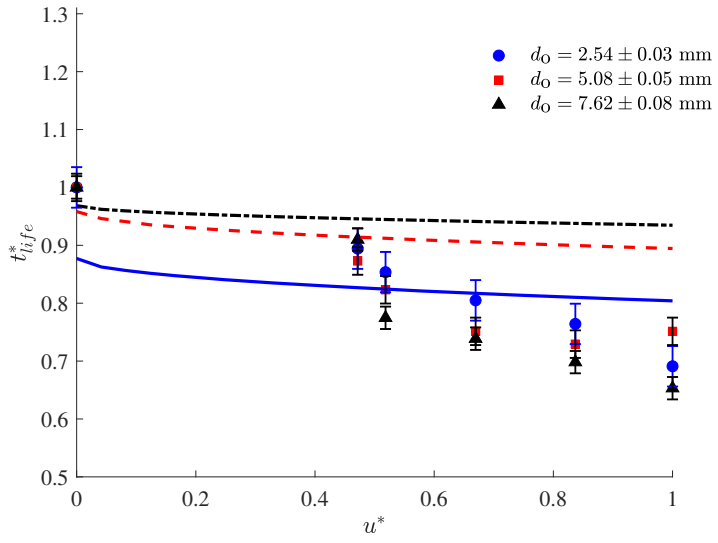

Figure 3.22: Normalized droplet lifetime plotted against droplet velocity for water droplets of varying initial diameter on a 250°C aluminum surface with 10° tilt angle. Normalized numerical droplet lifetime results from Eq. 3.10 and Eq. 3.14 are also plotted. Uncertainties in droplet velocity are smaller than marker sizes.

Total distance travelled by the Leidenfrost droplets throughout the droplet lifetimes are shown in Figs. 3.23, 3.24, and 3.25 for the 200°C, 225°C, and 250°C surface temperatures, respectively, with tilt angle of 10°. Across all temperatures, decreasing initial droplet diameter results in decreasing droplet distance travelled. Increases in droplet velocity linearly increase the distance travelled throughout the droplet lifetime suggesting equal change in droplet evaporation rate and velocity. Increasing temperature results in decreased droplet distance travelled at constant droplet initial size and velocity. It is therefore desirable to have droplets moving slowly through a device at the smallest possible initial droplet size to perform distillation in the smallest possible volume.

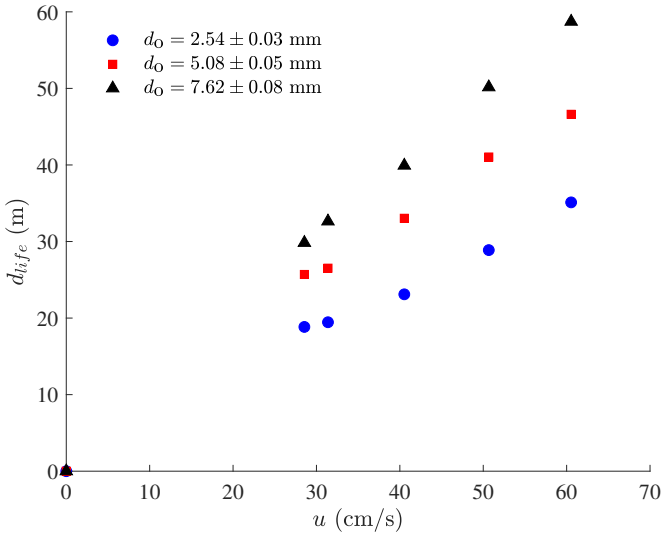

Figure 3.23: Droplet distance travelled throughout droplet lifetime as a function of droplet velocity for water droplets of varying initial diameter on a 200°C aluminum surface with 10° tilt angle. Uncertainties are smaller than marker sizes.

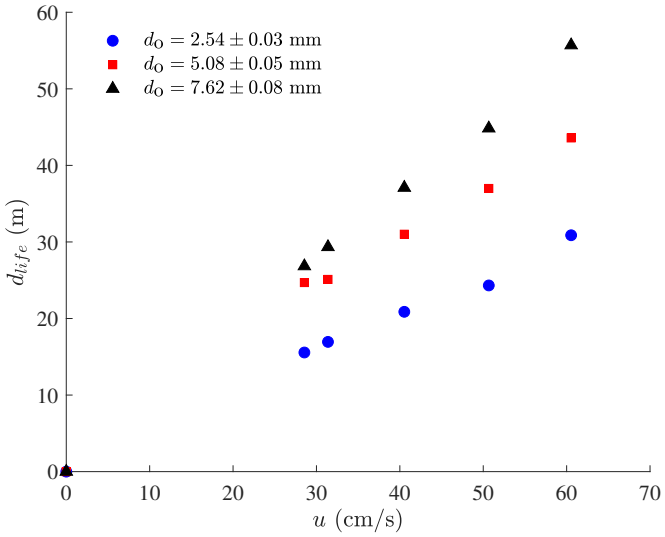

Figure 3.24: Droplet distance travelled throughout droplet lifetime as a function of droplet velocity for water droplets of varying initial diameter on a 225°C aluminum surface with 10° tilt angle. Uncertainties are smaller than marker sizes.

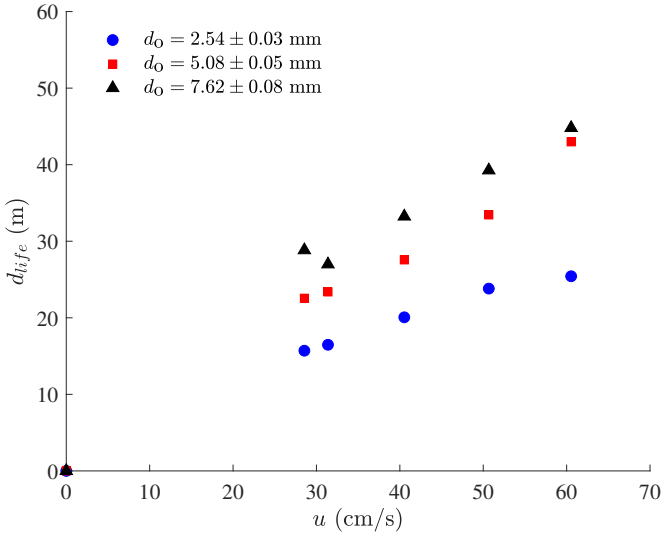

Figure 3.25: Droplet distance travelled throughout droplet lifetime as a function of droplet velocity for water droplets of varying initial diameter on a 250°C aluminum surface with 10° tilt angle. Uncertainties are smaller than marker sizes.

To assess the influence of the plate tilt angle on the Leidenfrost droplet lifetime, experiments at constant velocity, initial droplet size, and surface temperature were conducted. Figure 3.26 shows Leidenfrost droplet lifetimes plotted against tilt angle for droplets of d_o = 2.54 mm ± 0.03 mm with velocity of 34.7 ± 0.3 cm/s atop a plate with temperature of 200°C. Droplet lifetimes decrease as plate tilt angle is increased. It is suspected that centrifugal and natural convection are likely causes of the decrease in droplet lifetimes as a result of increasing plate tilt angle. As tilt angle increases, the resultant force between gravity and centrifugal acceleration increases. Figure 3.27 shows a cross-sectional view of a Leidenfrost droplet rolling in a circular track rotating along an axis of rotation shown by the dotted line and 'x' tilted with angle θ with respect to the horizontal plane. Let $\hat{\mathbf{g}}$ be the resultant vector between gravitational and centrifugal acceleration vectors, $\mathbf{g}$ and $\mathbf{g_c}$, respectively. The magnitude of the centrifugal acceleration is expressed as $||g_c|| = \mathrm{R_{plate}}\omega^2$ and is equal to 1.9 m/s^2 in this case. The magnitude of the resultant vector can be expressed as $||\hat{g}|| = \left(\left(g_c\cos\theta\right)^2 + \left(g + g_c\sin\theta\right)^2\right)^{1/2}$. The expression for thin film convective heat transfer to the Leidenfrost droplet derived in Eq. 3.7 suggest thin film convection has a one-third power dependence on gravity such that $q \sim g^{1/3}$. Replacing g with the magnitude of the new resultant vector $||\hat{g}||$ and assuming constant droplet contact area in the channel, the ratio between thin film convection at 20° and 4° tilt angles is $q_{20^\circ}/q_{4^\circ} = 1.016$. This result suggests a less than 2% increase in thin film convective heat transfer to the droplet as a result of increasing centrifugal acceleration at steep tilt angles and does not explain the magnitude of the decreased droplet lifetimes at large tilt angles.

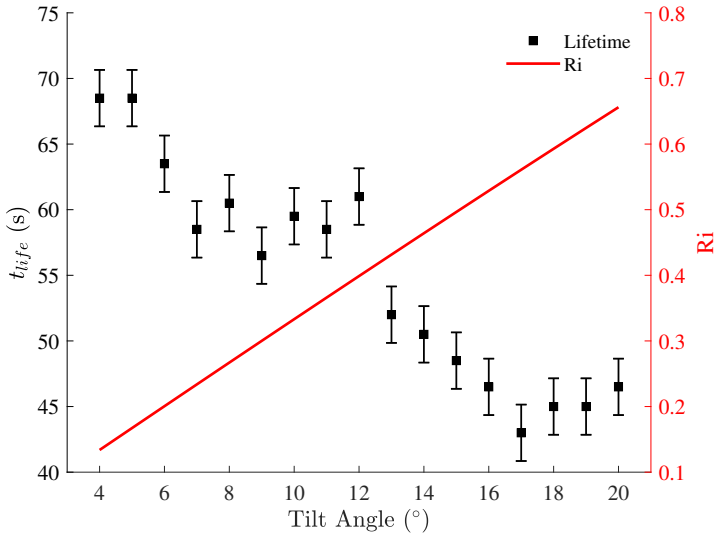

Figure 3.26: Droplet lifetime and Richardson number as a function of plate tilt angle for water droplets with d_o = 2.54 mm ± 0.03 mm, travelling with a velocity of 34.7 ± 0.3 cm/s, on a 200°C aluminum surface. Uncertainties in tilt angle are smaller than marker sizes.

The role of natural convection is assessed by computing the Richardson number, Ri = Gr/Re^2. The Richardson number describes the relative order of magnitude of forced and natural convection. If Ri $\ll$ 1 then free convection is negligibly small relative to forced convection, and may be neglected. The Grashoff number for the heated circular plate is estimated using the correlation from Fujii and Imura [163] for an inclined hot plate shown earlier. Figure 3.26 shows Richardson numbers for tilt angles between 4° and 20° for water droplets with d_o = 2.54 mm ± 0.03 mm, travelling with a velocity of 34.7 ± 0.3 cm/s, on a 200°C aluminum surface. Richardson numbers for 4°, 10°, and 20° tilt angles are 0.13, 0.33, and 0.65 respectively. At 4° natural convection may be neglected, especially due to the dominance of thin film convection, which is far more relevant than forced convection. For 10° tilt angle where Ri = 0.33, natural convection may also be neglected again due to the dominance of thin film convection

over natural and forced convection. At 15° tilt angle and beyond Ri ≥ 0.5, and at a 20° tilt angle Ri = 0.65 indicating that natural convection becomes significant and not-negligible relative to forced convection. Aside from increased natural convective forces as a function of tilt angle, droplets in the hemi-circular channel are pulled up closer to the 'rim' of the channel, where free-stream effects from natural convection are more noticeable. The observed increase in Richardson number with increasing angle as well as the droplet approaching channel rim are the most likely effects to decrease droplet lifetime with increasing tilt angle.

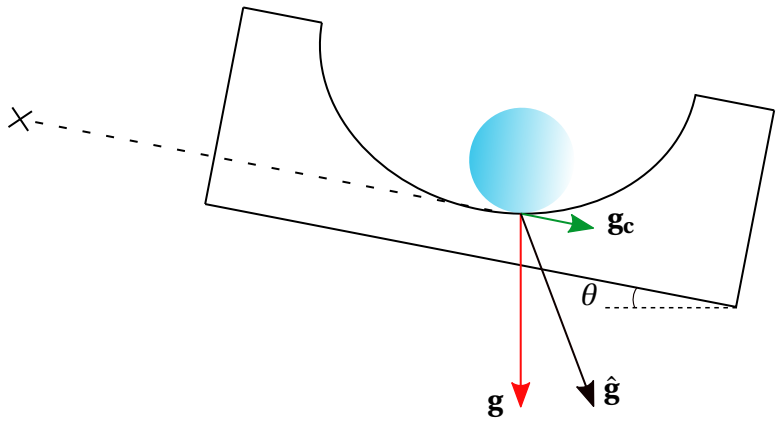

Figure 3.27: Cross-sectional view of a Leidenfrost droplet rolling in a circular channel with angle θ. The resultant vector $\hat{\mathbf{g}}$ is a combination of gravitational acceleration $\mathbf{g}$ and centrifugal acceleration $\mathbf{g_c}$ resulting from plate rotation along the axis of rotation shown by the dotted line and the 'x'.

3.5 Conclusion

Terrestrial and microgravity investigations of the Leidenfrost phenomenon relevant to potential applications aboard spacecraft life support systems have been presented. Analytical models are presented that predict Leidenfrost vapor layer thick-

nesses in microgravity for low velocity droplet impacts. A model for dynamic Leidenfrost droplets rolling on heated surfaces is also presented accounting for thin film convection and forced outer convection heat transfer to the droplets.

Novel microgravity Leidenfrost impact experiments are presented showcasing a variety of high-velocity dynamic Leidenfrost impacts on planar surfaces, surfaces with macro-roughness, and surfaces with cylindrical cross-sectional geometry in short duration drop tower tests. Also demonstrated are Leidenfrost droplet transport experiments through tortuous conduits in microgravity where droplets and streams of droplets are ejected through superheated tubes of varying lengths, diameters, and pathway geometry. Droplet transport between plates is presented where it is found that droplets bouncing between two parallel superheated plates experience decreases in incident and reflected angles due to Leidenfrost vapor recoil forces acting perpendicular to the impacted surfaces. This vapor recoil force is observed in low-velocity impacts where ethanol droplets are shown to propel away from superheated surfaces at increased normal velocity. In perhaps a first observation, the production of a large 'millimetric' vapor layer thickness of a liquid nitrogen droplet ejected nearly parallel to a superheated surface was achieved. The observed deflection of the droplet was measured to be 1.2 mm, which is in good agreement with the analytical prediction from Eq. 3.5 of 1.6 mm for the vapor layer thickness. Terrestrial vapor layers are typically 'micro-metric.'

To estimate possible performance of such processes in the sustained low-g environment of orbiting spacecraft, terrestrial Leidenfrost droplet lifetime experiments are presented for a stationary drop on a rotating Leidenfrost stage. The results show decreased droplet lifetime with increased droplet velocity, as well as a general decrease

in droplet lifetime with increased tilt angles. Results from the mathematical model developed compare somewhat favorably with experimental results. The analyses capture general droplet lifetime trends as well as overall droplet lifetimes to within ± 30%. The tests performed herein are supported by analyses that show how Leidenfrost phenomena is significantly enhanced in low-g environments.

With this knowledge, the utility of Leidenfrost phenomenon in microgravity is revealed as an attractive means of establishing essentially non-contact methods of fluids transport aboard spacecraft. For the present example, both experimental and theoretical results for Leidenfrost droplet lifetime and evaporation rates can serve as preliminary design tools for a Leidenfrost distillation system. We demonstrate non-contact microgravity Leidenfrost droplet impact phenomena on a variety of surface geometries for a variety of impact conditions. Leidenfrost droplet impacts in circular conduits are particularly applicable to practical microgravity distiller design. We also show how the addition of superhydrophobicity drastically reduces Leidenfrost temperatures for water from ~206°C to as low as ~140°C in microgravity. Such superhydrophobic substrates are observed to reduce fouling substantially, with fouled superhydrophobic surfaces capable of recovering their non-wetting characteristics after a simple rinse with clean water. These demonstrations encourage further exploitation of Leidenfrost phenomena towards fluids processing applications aboard spacecraft, such as water recovery via non-contact distillation from contaminated water sources for life support.

Chapter 4

Omni-Gravity Nanophotonic Heating and Leidenfrost-Driven Fouling-Free Water Recovery System

The work presented in this chapter is a result of a collaborative effort supported in part by a NASA Small Business Innovative Research Phase I Grant (80NSSC18P1957) and a NASA Space Technology Research Fellowship titled Leidenfrost Driven Waste-Water Separator, September 15, 2017: CoTR Jennifer Pruitt. We acknowledge contributions from Rawand M. Rasheed, Evan A. Thomas, Mark M. Weislogel, Paul Gardner, Tanya Rogers, and Rafael Verduzco in this work. We also acknowledge the efforts of John C. Graf.

4.1 Introduction

As highlighted in Chapter 1, even the current generation of spacecraft and terrestrial water recovery technologies are susceptible to failures caused by bio-fouling and mineral scaling, which can clog mechanical systems and degrade the performance of water recovery technologies [164]- [166]. Such failures require expensive and time-consuming maintenance and resupply and are thus limited to spacecraft where these resources are available [167]. Long duration spaceflight missions, such as extended stays at Lunar Outposts or during Mars transit, will increasingly benefit from water recovery hardware that minimizes the impact of fouling on hardware failures. Such systems would also benefit from a minimization in the number of moving parts, energy usage, and maintenance requirements. In this chapter, capillary fluid management

is employed in conjunction with nanophotonic hyper-localized heating to promote fouling-free fluid management at all levels of gravity. The Leidenfrost phenomenon is again exploited in this work to achieve fouling-free non-contact heat-driven distillation of waste-water streams capable of > 98% of water recovery.

Capillary fluid management systems have been utilized aboard spacecraft for decades. These systems typically employ clean, single-phase fluids such as propellants, cryogenics, and thermal-fluids where the wetting conditions are known and favorable with contact angle θ generally equal to 0° [168]. However, for life support fluids, partial wetting conditions ($0° < \theta < 90°$) are far more common and are often considered unfavorable for capillary solutions due to insufficient or erratic wetting conditions. As a result, capillary solutions have historically been under-utilized for water-based systems aboard spacecraft. Instead, forced flows and rotary separation devices have been employed to perform essential fluid phase separations [168]. Such engineering solutions employing dynamic system components (e.g. Space Shuttle rotary fan separator) are potentially unfavorable due to power consumption, increased system complexity, noise, and increased failure modes [169]. In comparison, utilizing capillary phenomenon even when wetting conditions are not optimal has the potential of offering advantages over current state-of-the-art technologies potentially reducing moving components, power consumption, and noise while increasing reliability. Weislogel et al. [168] and Weislogel et al. [170] developed a static phase separator (SPS) employing overlapping geometric capillary solutions to convert droplet streams to separated gas-liquid volumes. The SPS was tested in reduced gravity flight experiments and was shown to be capable of accommodating highly variable unfavorable wetting conditions. A sub-scale prototype achieved nearly 100% separation for fluids with widely

varying contact angles. In contrast to state-of-the-art mechanical approaches, it is anticipated that passive capillary driven liquid phase separation is feasible directly in place of active rotary separators for wastewater applications. Thomas and Muirhead [115] demonstrate increased wetting of urine on fouled surfaces, resulting from fouling caused by solutes in urine. This suggests an added benefit to capillary fluid containment solutions employed for management of waste streams. An omni-gravity SPS for multiphase liquid-gas flows is developed in this work.

Nanophotonic heating may be exploited for the pasteurization of waste-water in the SPS. When spherical nanoparticles (i.e., gold or carbon) interact at a specific wavelength of light, the nanoparticle experiences a harmonic shift in electron polarity throughout the nanoparticle. This causes the particle to resonate producing localized heat around it for a distance on the order of micros [171]. This phenomenon is known as surface plasmon resonance [172]. Hogan et al. [173] demonstrate localized heating and steam generation in a water bath without significant heating of the bulk solution by employing light induced localized heating of dispersed nanoparticles. In such a regime, light is both scattered and absorbed inducing concentrated electromagnetic energy in a small volume. Neumann et al. [174] demonstrate this effect using solar light in place of an artificial light. The study of light-induced heating of nanoparticles has gained much attention in the past decade [175]- [178] for applications in localized drug delivery [179], cancer treatment [180] [181], salt-water distillation [182], and others [183] [184]. Herein, we utilize IR LED induced localized heating of carbon black nanoparticles for pasteurization of streams of waste-water.

The Leidenfrost phenomenon is again exploited herein to promote heat driven non-contact distillation of waste-water droplet streams. Heat driven distillation is typ-

ically employed in the pooling boiling regime to perform distillation of liquid-liquid and liquid-solute solutions. Liquid droplets undergo pool boiling when deposited on substrates at or slightly above the liquid's boiling temperature. In this regime, droplets undergo nucleate boiling and boil away in seconds. However, if liquid droplets are deposited on a substrate with a temperature significantly higher than the liquid's boiling temperature, the droplets do not undergo nucleate boiling, but will instead levitate on their own vapor layer. The droplets levitate above and are insulated from the heated substrate by this vapor layer, reducing heat transfer to the droplets by orders of magnitude and eliminating nucleation sites for bubble formation. These combined effects significantly increase droplet lifetimes. For example, capillary sized droplets of water deposited on an aluminum surface held at the Leidenfrost point of water on aluminum (193°C) will take minutes to evaporate completely.

Exploiting the Leidenfrost phenomena to perform distillation of streams of droplets is advantageous for spacecraft applications. The non-contact nature of the phenomenon enables touchless, potentially fouling-free distillation. Leidenfrost distillation is also heat-driven, enabling complete distillation of droplets of waste-water to their salty constituents. Stamey and Mihara [122] present experimental results for bacterial growth in sterile urine from human subjects, discovering that exponential bacterial growth occurs after two hours for all types of bacteria. Leidenfrost distillation rates are comparable to urine production/delivery rates of humans, which permits essentially real-time distillation of streams of droplets at elevated temperatures. Liquid solutions of urine processed essentially on-demand at temperatures in excess of 70°C ensure minimal microbial growth, reducing, if not eliminating, the need for urine pretreat chemicals used to significantly hinder the rate of bacterial growth in urine in the

current state-of-the-art urine-water recovery technology. Lastly, only simple motive forces are necessary for transport of droplet streams in the Leidenfrost state due to the high mobility of Leidenfrost droplets resulting from vapor layer separation of droplets from surfaces. Viscous drag from the vapor layer is negligibly small leading to nearly frictionless motion across the heated surfaces.

The Leidenfrost effect has been studied extensively for its relevance to numerous applications including metals manufacturing, fuel combustion, jet and rocket engine propulsion, spray cooling, nuclear reactor cooling, and others [123]- [131]. Selected works are highlighted here. Biance et al. [132] investigated Leidenfrost phenomenon providing a scale expression for static Leidenfrost droplet lifetimes. Orzechowski and Wcislik conduct an experimental investigation of static Leidenfrost droplet heat transfer and evaporation rates [143]. Maquet et al. [144] demonstrate the Leidenfrost point has a weak dependence on gravity level, but that Leidenfrost droplet lifetimes have a strong inverse dependence on gravity. Vakarelski et al. [185] report significant decreases in the Leidenfrost point on microstructured superhydrophobic surfaces, which was found to result from vapor layer stabilization on such surfaces. Exploratory low-gravity Leidenfrost behavior has been pursued in drop tower tests [103] [105]. Rasheed and Weislogel present evaporation rates for dynamically rolling Leidenfrost droplets and investigate Leidenfrost phenomenon in low-gravity, including dynamic Leidenfrost droplet impacts and Leidenfrost droplet transport through conduits [112]. Rasheed and Weislogel [159] present facile production methods for superhydrophobic surfaces, including thermally stable surfaces, utilized for Leidenfrost droplet distillation experiments.

Herein, a water recovery concept is proposed and developed that employs the Lei-

denfrost phenomenon to promote non-contact heat-driven distillation of streams of salt-water droplets. A hot aluminum hemi-circular track approximately 8.5 m in length is employed to perform droplet distillation. An omni-gravity SPS is developed taking advantage of geometry to separate gas and liquid phases from incoming fluid streams in microgravity and gravity dominated environments ($1 - g_o$ and partial gravity). Surfaces of the SPS are coated with carbon black nanoparticles that are irradiated with IR LED's enabling heating of surfaces and subsequent pasteurization of fluid streams. The developed system takes advantage of gravitational forces in gravity dominated environments while utilizing capillary forces in microgravity performing fluid containment, management, and waste-water distillation in all levels of gravity.

4.2 Wate-Water Recovery System Development

4.2.1 System Overview

The omni-gravity nanophotonic heating and leidenfrost-driven fouling-free water recovery system (WRS) is a two loop system capable of continuous processing of up to one liter of waste-water at a rate of 500 mL/hr. Figure 4.1 shows a block diagram of the WRS. The architecture remains the same for all gravity environments, but the unit processing conditions vary. Waste-water streams aboard spacecraft typically comprise of humidity condensate from cabin atmospheres resulting from human respiration and perspiration, urine streams, and greywater, which consists of waste-water resulting from hygiene (shower), sink (hand-wash), and laundry streams. Humidity condensate streams are typically collected by other systems aboard spacecraft (i.e. condensing heat exchanger) and are sterile enough to be directly distilled. In the WRS, humidity condensate streams are sent directly to the distillation step, as shown in Fig. 4.1.

The distillation step also receives a stream of waste-water from the SPS. The distillation step is designed to process waste-water streams at a rate of up to 500 mL/hr. Urine streams from the urinal and greywater are fed into the SPS with a one liter capacity, where the waste-water stream is pasteurized by nanophotonic heating induced by IR light interacting with carbon black nanoparticles. This stream is then sent to the Leidenfrost distiller. All distilled streams go through a quality check where 'passing' streams go into a potable water supply, and 'failed' streams sent back to the SPS for repeat processing. Figure 4.2 provides a CAD rendering of the complete system with respective system components labeled. Each system component and respective step in the process schematic will be developed further in forthcoming sections.

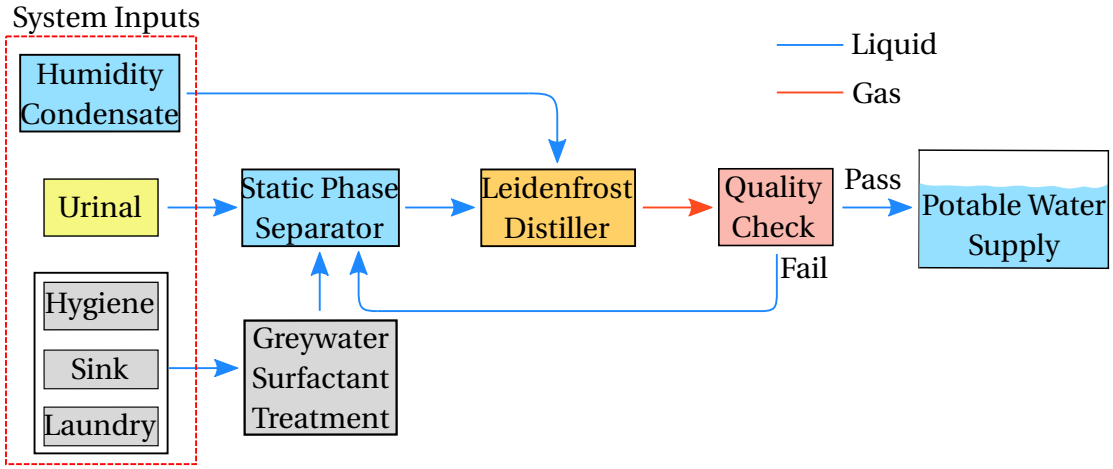

Figure 4.1: Block diagram of the integrated Water Recovery System.

4.2.2 Liquid-Gas Static Phase Separator Design

The passive SPS device was previously developed and tested in a low-gravity environment demonstrating successful liquid-gas phase separation under highly variable wetting conditions [168]. In this work, we utilized the results from the sub-scale

designs to develop a full-scale SPS capable of separating and retaining up to one liter of liquid in microgravity and partial gravity environments. Figure 4.3 provides a schematic of the SPS with cross-sectional geometries outlined at key locations. In microgravity, waste-water streams enter the SPS and traverse a series of loops inducing modest centrifugal forces on the droplet stream causing droplets to impact the walls of the device. Cross-sectional interior corner geometries in the SPS cause wetting fluids ($\theta < 90°$) to wick into the interior corner. Capillary forces hold the fluid in the interior corner. A capillary gradient resulting from varied interior corner half angle (cross-section A-A to B-B) and veined structures (cross-section C-C) at the SPS outlet induce a stable separated flow that carries fluid downstream to the SPS outlet.

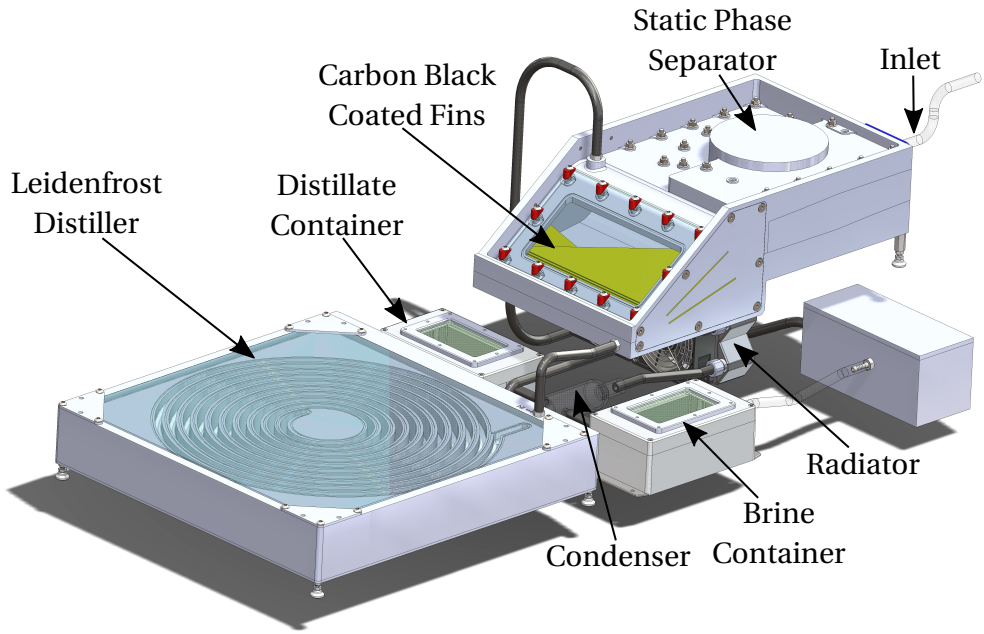

Figure 4.2: CAD rendering of the water recovery system with labeled system components.

In gravity dominated environments (ie. Lunar, Martian, and Earth surfaces) the

separation of liquid-gas streams in the SPS is accomplished predominantly by stabilization and sedimentation. The SPS interior core is designed with a 5° slope. While a sloped interior helix does not influence microgravity performance, it provides a mode of transport for incoming liquid to drain downstream from the SPS inlet, shown in Fig. 4.2, to the finned reservoir. The finned reservoir is sloped at 30° to promote fluid containment in a gravity dominated environment. Figure 4.4b shows a CAD rendering of the assembled SPS with transparent features to showcase inner geometries of the device, including the sloped SPS core and reservoir.

A CAD model with exploded view of the SPS highlighting the individual system components is shown in Fig. 4.4a. The SPS is a multi-component device consisting of a helical coiled core, a conical body for liquid-gas separation, and carbon coated fins. The SPS body is made primarily of aluminum (Fig. 4.4a gray and blue components). The fins (Fig. 4.4a yellow) are carbon black coated aluminum and the helical coil core (Fig. 4.4a red) is 3D printed polylactide (PLA). The SPS has a glass window where IR LED lights are mounted to irradiate the carbon black nanoparticles on the fins. All the components are assembled with an array of screws and bolts (assembled SPS shown in Fig. 4.2 and Fig. 4.4). Figure 4.4b shows a CAD rendering of the assembled SPS with transparent features showing inner geometries in the assembled device.

4.2.3 Carbon Black Nanoparticle Coating

The triangular aluminum fins (Fig. 4.2 & Fig. 4.4) are manufactured from 2.5 mm thick aluminum and coated with carbon black nanoparticles deposited by a plasmonic nanoparticle solution. Activated carbon CEP21K (surface area 2040 m^2/g) was purchased from Power Carbon Technology Co., Ltd. Gold nanoparticles (AuNP) of 15 nm

outer diameter (OD) suspended in 0.1 mM phosphate-buffered silane (PBS) was purchased from Sigma-Aldrich. Fully hydrolyzed Poly(vinyl alcohol) (PVA, MW = 89,000 - 98,000 g/mol) and 25 wt% aqueous solution of glutaraldehyde (GA) were produced in-house.

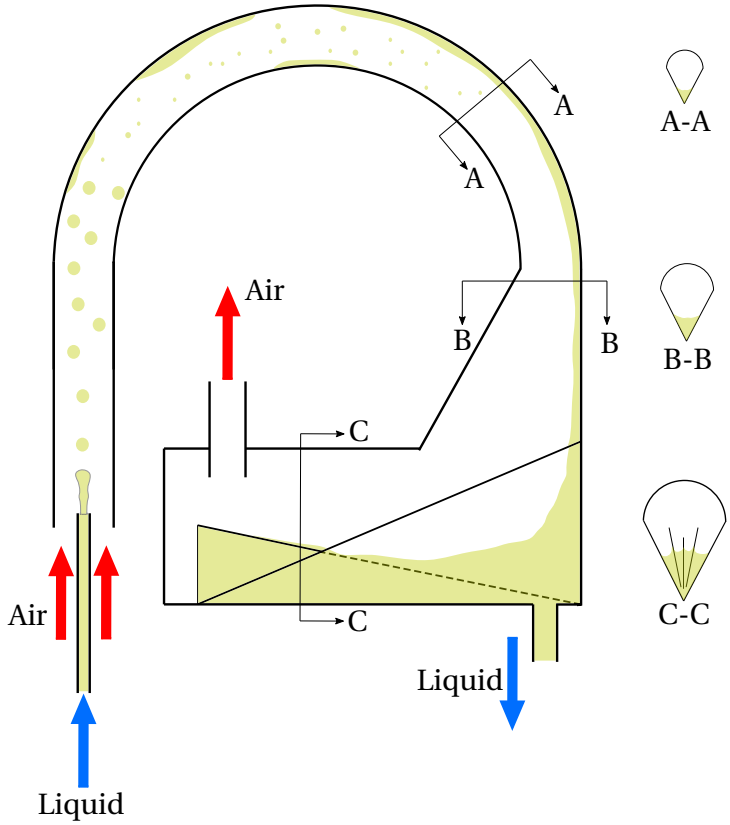

Figure 4.3: Schematic the static phase separator showing a top-down view of the device with cross-sectional views of the internal geometries. Separation of liquid-gas streams in microgravity is achieved utilizing centrifugal forces to promote droplet impacts onto surfaces. Liquid is then wicked down into the interior corners, where the energetic states are favorable for fluids. Separation of liquid-gas streams in partial gravity environments is achieved in the static phase separator primarily due to settling resulting from gravity.

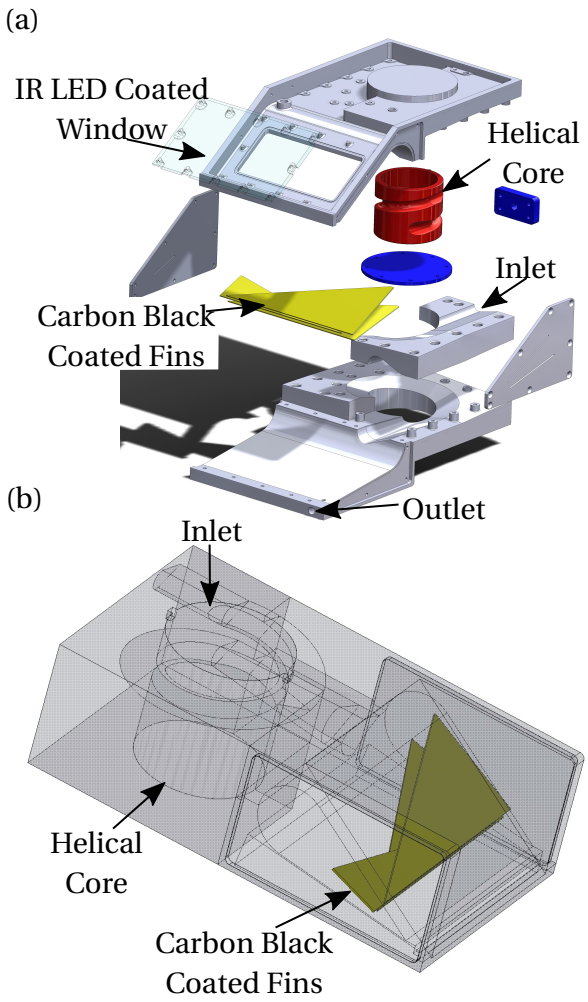

Figure 4.4: (a) CAD rendering of static phase separator exploded assembly view. Metal components (gray and blue) are made of aluminum, fins (yellow) are carbon black coated aluminum, and helical coil (red) is 3D printed out of polylactide (PLA). (b) A CAD rendering of the assembled static phase separator with transparent features showcasing inner geometries of the device.

The plasmonic nanoparticle surface treatment solution was prepared with a solution composition of 70 wt% of high-surface-area powdered activated carbon (PAC), 20 wt% of 15 nm gold nanoparticles in aforementioned buffer solution, and 10 wt % of polymeric binder (linear polymer PVA and cross-linker GA) based on total mass. First,

6 wt% PVA solution was prepared by mixing PVA in DI water at 90°C for 4 hours. Next, 5 mol% (relative to PVA repeat units) of GA solution was added and mixed for 1 hour. PAC was added slowly along with additional DI water, giving a solid content of the solution of approximately 30 wt%. The resulting mixture was stirred for 12 hours to ensure solution homogeneity. Lastly, 20 wt% of AuNP was added to the solution and allowed to mix for an additional hour. In total, 6 mL of nanoparticle solution was manually flow-coated onto each aluminum fin. A pipette was used to deposit the solution across the fin surface and then spread into a thin film using an acrylic planar surface. The fins were allowed to dry at room temperature then placed in an oven at 130°C for 1 hour to cross-link. The aluminum fins coated with carbon black nanoparticles are shown in Fig. 4.5.

Figure 4.5: Post process aluminum fins coated with carbon black nanoparticles.

4.2.4 Non-Contact Leidenfrost Distiller Design

The non-contact Leidenfrost distiller is designed to distill a stream of waste-water droplets. It is perhaps the most gravity sensitive component of this system. The Leidenfrost distiller needs to incorporate sufficient droplet residence time in the distiller to perform optimal distillation of each individual droplet. Too much residence times result in complete droplet distillation before exiting the distiller, potentially resulting in fouling the distiller surfaces while too little residence times result in droplets that are not sufficiently distilled upon exiting the distiller. Approximately 90% droplet distillation in the Leidenfrost distiller is selected to significantly distill droplets while protecting distiller surfaces from potential fouling due to precipitation of solutes in waste-water solutions, which result in wetting and fouling of surfaces. Passive evaporation in a heated, disposable catch basin performs the remainder of the distillation. Figure 4.6 shows a series of images of a urine droplet distilled on a superhydrophobic surface held at 140°C, above the Leidenfrost point of water on a superhydrophobic surface. After approximately 93% droplet distillation, the solutes in urine begin to precipitate, changing the urine composition from predominantly water-based to oil-based. Oily solutions have drastically lower surface tension values than water, resulting in dramatically elevated Leidenfrost point temperatures relative to water [146]. This transition is shown in Fig. 4.6 at t = 100 s, and t = 103 s where the droplet wets (and fouls) the superhydrophobic surface. To ensure ideal droplet distillation, the design of the Leidenfrost distiller requires optimization of two independent variables, surface temperature and pitch. Pitch defines the droplet velocity and residence time in the distiller and the temperature dictates droplet distillation rate.

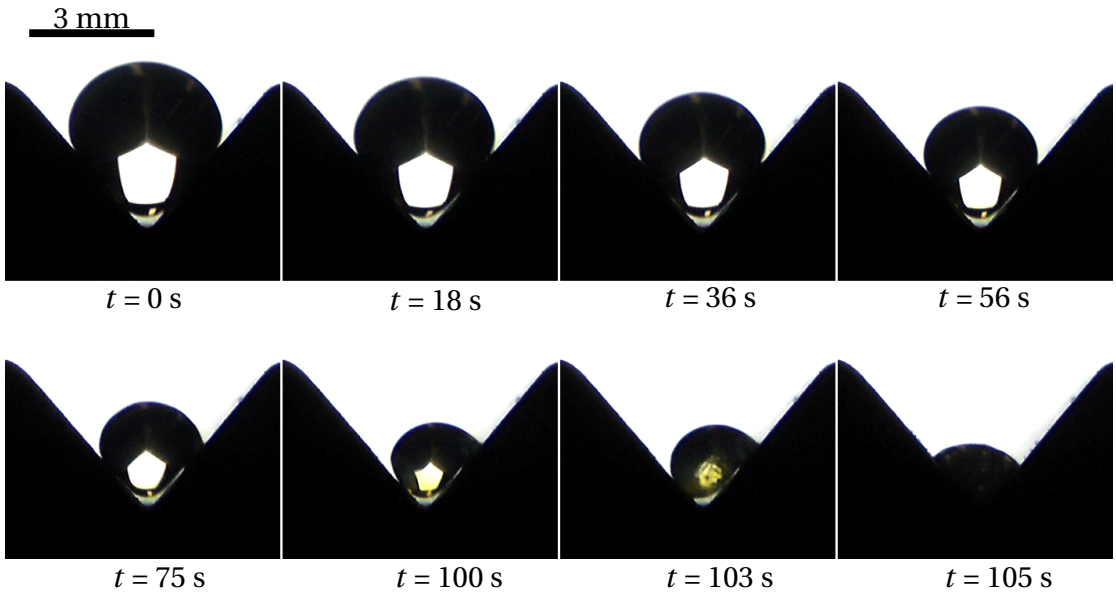

Figure 4.6: A droplet of urine distilled on a superhydrophobic plate held at 140°C. The droplet has a diameter of 3.9 mm at t = 0 s and begins to undergo wetting between t = 100 s and t = 103 s, where the droplet radius is reduced below 1.7 mm, signifying a ~92% reduction in droplet volume.

Droplet evaporation rates are predicted from a simple mathematical model describing the heat transfer from a hot surface to a droplet on a surface above the Leidenfrost temperature. Figure 4.7 provides a schematic of a droplet with time varying radius $r(t)$ at saturation temperature T_d rolling with linear velocity u on a superheated surface with temperature T_s and tilt angle α in an ambient environment with temperature T_∞. Through a balance in hydrostatic pressure from droplet mass and vapor pressure from droplet evaporation, a scale expression for the Leidenfrost vapor layer thickness is derived,

$$\delta \sim \left(\frac{\mu_v k_v \Delta T_1}{2\rho_l \rho_v g \left(c_p \Delta T_2 + h_{fg} \right)} \right)^{1/3}, \tag{4.1}$$

where k_v is the droplet vapor thermal conductivity, ρ_l is the liquid droplet density, ρ_v is the droplet vapor density, μ_v is the droplet vapor viscosity, c_p is the droplet specific heat, h_{fg} is the droplet latent heat of vaporization, g is gravitational acceleration, $\Delta T_1 = T_s - T_d$ is the difference between plate temperature and droplet saturation temperature, and $\Delta T_2 = T_d - T_o$ is the difference between droplet saturation temperature and initial droplet temperature. Assuming a planar droplet surface at the droplet substrate interface and balancing vapor pressure with viscous forces where vapor pressure is expressed in terms of the droplet hydrostatic pressure a scale expression for the vapor velocity is derived $u_{vap} \sim \left(2\rho_l g\delta^2\right)/\mu_v$. The Reynolds number $\mathrm{Re} = \left(\rho_l u_{vap}\delta\right)/\mu_v$ is computed for the vapor flow and suggests laminar flow in the vapor layer. Assuming constant planar substrate temperature with insulated boundary condition the Nusselt number is constant and equal to 4.86 [160]. Using Eq. 4.1 and setting the droplet heat transfer area equal to the projected spherical cap area at approximately 90% of the droplet radius, an expression for steady thin film convection through the vapor layer to the droplet can then be expressed as

$$q = \pi r^2 \left(k_v \Delta T_1\right)^{2/3} \left(2\rho_l \rho_v g \left(c_p \Delta T_2 + h_{fg}\right) {\mu_v}^{-1}\right)^{1/3}. \tag{4.2}$$

Order of magnitude comparisons show that thin film convection is the dominant mode of heat transfer to the droplet while outer forced convection, free convection and radiation are negligibly small. Forced outer convection over the spherical drops may be considered in this case as was done by Rasheed and Weislogel [112], but for the operating conditions of the Leidenfrost distiller device, the spherical drop forced convection is also negligibly small. The mass rate of change for an evaporating spherical droplet can be expressed as

$$\dot{m} = -4\pi\rho_l r^2 r_t, \tag{4.3}$$

where $r_t \equiv dr/dt$ is the time rate of change of the droplet radius. The evaporative mass flowrate is expressed in terms of the total heat transfer to the droplet using the expression $q = \dot{m}\left(c_p\Delta T_2 + h_{fg}\right)$, substitution into which Eqs. 4.2 and Eq. 4.3 result in a first order linear ODE describing the droplet evaporation rate,

$$r_t = \frac{1}{4}\left(\frac{k_v\Delta T_1}{\rho_l\mu_v^{1/2}\left(c_p\Delta T_2 + h_{fg}\right)}\right)^{2/3}\left(2\rho_v g\right)^{1/3}. \tag{4.4}$$

A single integration of Eq. 4.4 with $r\,(t=0) = R_o$ results in,

$$r(t) = R_o - kt, \tag{4.5}$$

where $k \equiv \frac{1}{4}\left(\frac{k_v\Delta T_1}{\rho_l\mu_v^{1/2}(c_p\Delta T_2+h_{fg})}\right)^{2/3}\left(2\rho_v g\right)^{1/3}$. Solutions to Eq. 4.5 are used to predict the overall lifetime of a droplet on a surface heated past the Leidenfrost temperature for all levels of gravity.

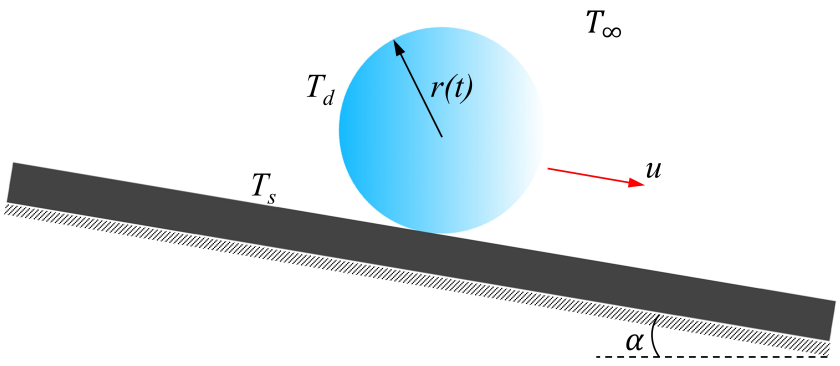

Figure 4.7: A droplet rolling with linear velocity u on a heated tilted substrate exceeding the liquid's Leidenfrost point.

The Leidenfrost distiller employs a gravity feed for waste-water droplet delivery. Such droplets are typically capillary sized droplets. The capillary length-scale is predicted for any celestial body through a balance between capillary and gravitational forces on a fluid. Solving for the characteristic length-scale, the expression $L_c = \left(\frac{\sigma}{\Delta\rho g}\right)^{1/2}$ is derived where σ is the fluid surface tension and $\Delta\rho$ is the difference in density between interfacing fluids (i.e., water-air). For a terrestrial system, capillary sized droplets are typically on the order of 2.7 mm in diameter. The Leidenfrost distiller is designed to operate at 230°C to ensure that surfaces stay well above the Leidenfrost point of water on aluminum. Solutions to Eq. 4.5 for the time to distill a capillary sized water droplet to 90% of the original radius atop a surface held at 230°C suggest a total residence time of approximately 77 s.

For the Leidenfrost distiller design, a sloped circular channel was designed and manufactured from aluminum. Figure 4.8a shows a CAD rendering of the designed Leidenfrost distiller. A scale expression for the slope of the channel was derived equating the energy resulting from gravity to the rotational and translational kinetic energy of the droplet and work done on the droplet due to air-drag. A channel pitch angle of 0.25° was derived. Figure 4.8b shows a CAD rendering of the Leidenfrost distiller cross section showcasing the distiller pitch. A corresponding total channel length of ~ 8.5 m is required to ensure droplet residence time of ~ 75 s in the distiller. Based on maximum characteristic droplet diameter (2.7 mm), the channel was milled with a 3/8" ball nose end mill resulting in a semicircular cross section (shown in Fig. 4.8b). The Leidenfrost distiller tracks were manufactured with machined grooves for O-ring placements. A 0.25" thick glass lid was mounted atop the Leidenfrost distiller tracks sealed with high-temperature O-rings, and clamped with four brackets at each corner

of the distiller. These features are shown in Fig. 4.8a.

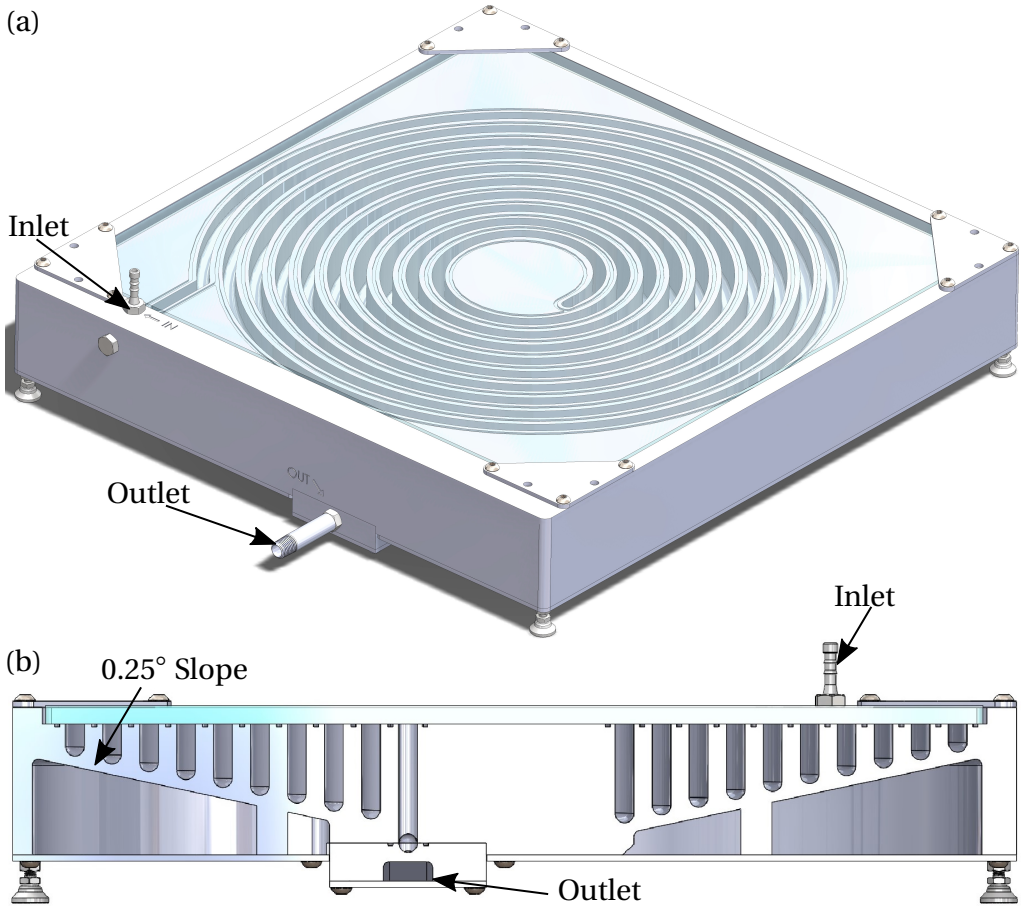

Figure 4.8: (a) An isometric view of the CAD model of the Leidenfrost distiller and (b) a cross sectional view of the Leidenfrost distiller.

The droplet evaporation model of Eq. 4.5 provides a design tool for the Leidenfrost distiller. As shown in Eq. 4.5, distillation rates in the Leidenfrost state have a weak power law dependence on gravity. Although weakly dependent on gravity, changing the gravitational constant from terrestrial (1-g_o) to Lunar surface ($1/6 - g_o$) and holding all else constant results in 129 s, or a 1.7 factor increase, to achieve 90% distillation of a 2.7 mm droplet. Gravity fed droplets on the Lunar surface will also have different

characteristic sizes than terrestrial droplets. Droplets will have a capillary length on the order of 6.6 mm on the Lunar surface. Further, gravity driven droplet velocities are directly proportional to gravitational acceleration imparted on them. The dramatically varying system parameters resulting from varying gravity levels means that Leidenfrost distiller designs are uniquely optimized for a single gravitational environment. Despite this, however, Leidenfrost distiller designs for different gravity environments can readily be resized using the developed design tools.

4.2.5 Auxiliary System Components

Other system components include Leidenfrost distiller heaters, heater controls, thermal insulation, a vacuum pump, condenser, and plumbing elements. Figure 4.9 shows an image of the full system build with labeled system components. The Leidenfrost distiller heaters shown in Fig. 4.9 were manufactured from k23 firebricks and two resistance heater wires each with 8.4 Ohm nominal resistance capable of dissipating 1440 W of power per heater wire at 110 V, providing a total of ~ 2900 W heating power to the distiller. The resistance heating wires were laid onto and stapled into the firebrick with heavy duty staples to mount the wire to the brick. A temperature control circuit consisting of a temperature controller, thermocouples, and high power relays were utilized to control resistance heater power and maintain set point temperatures in the Leidenfrost distiller. The Leidenfrost distiller was wrapped in 4" of high temperature ceramic fiber insulation to limit thermal losses to the environment.

IR LED strips 940 nm nominal wavelength shown in Fig. 4.9 were utilized for nanoparticle irradiation. A jacketed glass coiled reflux condenser 200 mm in length was assembled with a Koolance computer cooling loop capable of ~ 1700 W of cool-

ing, which consisted of a radiator, cooling fans, and coolant circulating pump (shown in Fig. 4.9). The vapor trail and salty droplets from the Leidenfrost distiller are routed through a waste catch basin (shown in Fig. 4.9), where salty droplets are captured and stored. The vapor trail is pumped from the catch basin through the condenser where it is condensed and captured in a distillate catch basin (shown in Fig. 4.9). The whole system is interconnected with vacuum tube plumbing, with a vacuum pump inline to draw steam from the Leidenfrost distiller to the distillate catch basin.

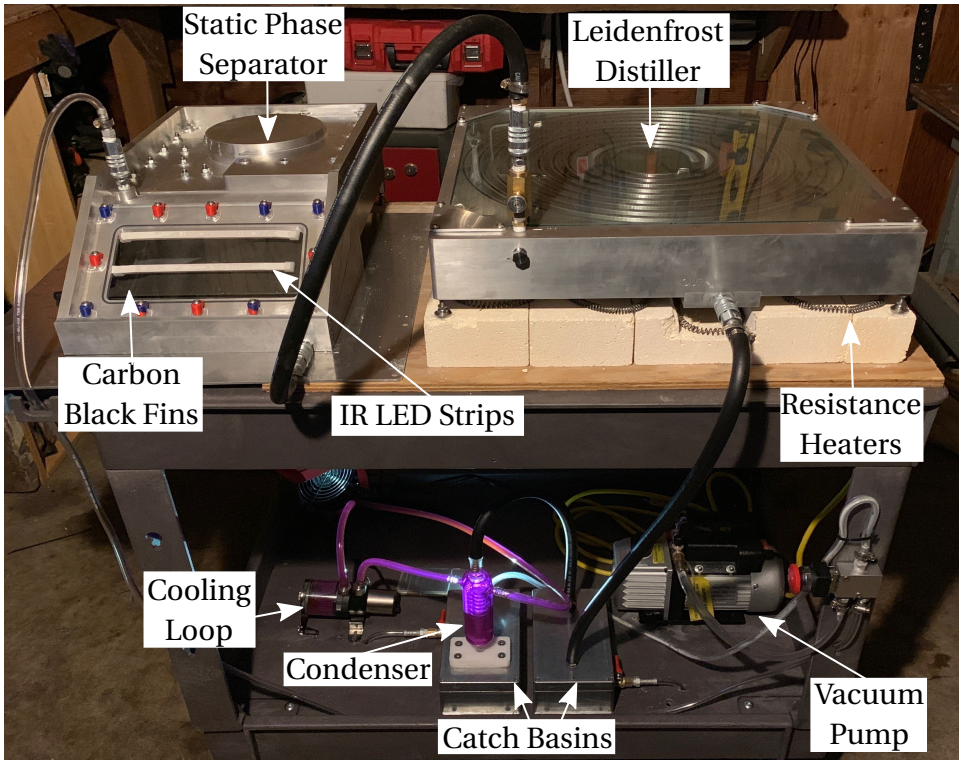

Figure 4.9: Final water recovery system build. Thermal insulation is omitted.

4.3 Results and Discussion

4.3.1 Nanophotonic Heating

The nanoparticle coated aluminum fins were directly exposed to an IR LED source at a peak wavelength of 940 nm. Under the presence of the photon emitting field, electrons inside the nanoparticles were mobilized as energy carriers through plasmon resonance phenomenon. Excitons were created as heat dissipated through an interband absorption process, both scattering and adsorbing light. The nanoparticles concentrated light energy into mesocale volumes near the illuminated fin surface, creating intense localized heating and providing an elevated temperature source for surrounding mediums. Three case scenarios were tested for localized heating using a SEEK thermal imaging camera. For the baseline scenario, an aluminum coupon was coated with 3 mL of activated carbon CEP21K-H_2O solution and room temperature readings were recorded. For the second scenario, the coupon was exposed to a 940 nm IR LED strip with density of 60 LED's/m placed in a fixed position 70 mm parallel from the plate surface. Temperature readings were recorded at 1 minute intervals until incremental changes were no longer observed after 4 minutes. For the third scenario, 20 wt% of 15 nm gold nanoparticle constituent was added to activated carbon CEP21K-H_2O solution and 3 mL was surface coated onto a fresh aluminum coupon. The coupon was placed in the same test configuration from scenario two and exposed to LED photons for 4 minutes.

Figure 4.10 shows images highlighting the thermal imaging results for cases 1,2, and 3. Test coupon 2 (Fig. 4.10b) coated with activated carbon-H_2O solution reached a maximum surface temperature of 84 °F after 4 minutes of LED exposure. Test coupon

3 (Fig. 4.10c) was coated with activated carbon-H_2O and gold nanoparticle constituent reached a maximum surface temperature of 91 °F after 4 minutes of exposure. These elevated temperatures, in combination with the biocidal nature of gold nanoparticles [186] [187] due to the oligodynamic effect, are capable of rendering microbes inactive in both wastewater and recovered distillate streams.

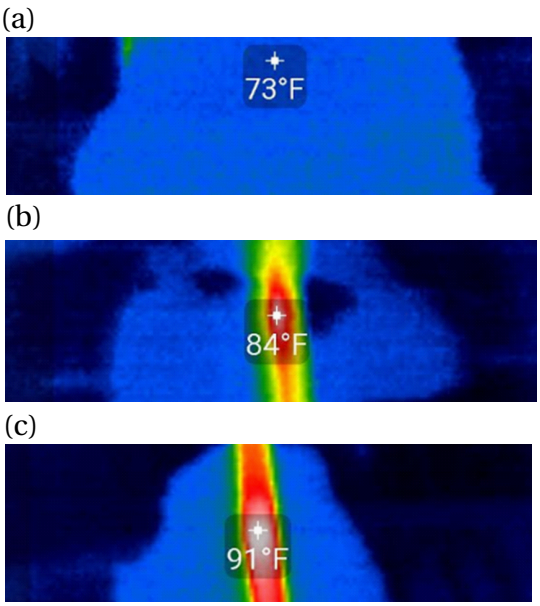

Figure 4.10: Thermal images from (a) baseline carbon black nanoparticle aluminum coated fin at room temperature and (b) exposed to 940 nm IR LED strips with density of 60 LED's/m. (c) Aluminum fin coated with activated carbon CEP21k-H_2O solution with 20 wt% of 15 nm gold nanoparticle constituent added and exposed to 940 nm IR LED strips with density of 60 LED's/m.

4.3.2 Salt-Water Distillation

The Leidenfrost Distiller was tested with salt-water as a urine ersatz fluid. A salt-water salinity of 40 milliSiemens (mS) was chosen, which is approximately that of sea-water, to closely approximate urine solids content. The distiller operating temperature

for distillation experiments was set to 230°C. Experiments were conducted wherein salt-water was fed to the distiller in the form of a stream of droplets, as shown in Fig. 4.11. Distilled salty brine droplets were captured in the brine container (shown in Fig. 4.9). Steam from the Leidenfrost distiller was pumped to the condenser with the vacuum pump and captured as distillate in the distillate container. The Leidenfrost distiller operation was recorded with a highspeed HD video camera. Throughout the operation of the Leidenfrost distiller, scaling and deposition of salt-water on distiller surfaces was not observed. Surfaces remained free of salt residue throughout the duration of the ~ 20 hours of distiller operation.

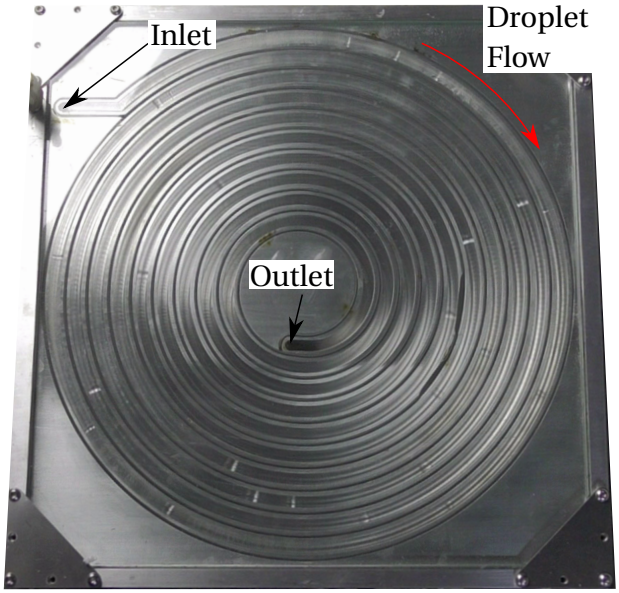

Figure 4.11: Top down view of the Leidenfrost distiller operating at 230 °C with droplets of 40 mS salt-water flowing through the distiller.

Salinity and volume of the captured brine and distillate were measured at varied intervals. Figure 4.12 shows a bar-plot of the ratio of distillate and brine volumes collected. The sum of the ratio of distillate and brine is equal to one. The amount of distillate collected was on average about 40% of the total initial influent volume, meaning the Leidenfrost distiller achieved only about 40% water recovery from salt-water. This figure is about half of the target 90% water recovery rate. Figure 4.13 shows a plot of experimentally measured evaporation rates of individual droplets measured from videos of the Leidenfrost Distiller experiments. The distiller design operating temperature of 230°C and an elevated operating temperature of 310°C were investigated. Also plotted on Fig. 4.13 are theoretically determined droplet evaporation rates from Eq. 4.5 to assess the accuracy of the developed droplet lifetime model. Experimental and theoretical results presented in Fig. 4.13 for droplet evaporation rates at 230°C indicate good agreement with theoretical results predicting experimental droplet evaporation rates with an average error of ~ 35%. At 310°C, Eq. 4.5 is order-of-magnitude accurate, underpredicting experimental droplet evaporation rates with an average percent error of ~ 54%. There is an observable increase in deviation from experimental and theoretical results when comparing results from 230°C and 310°C. This is likely due to the flat plate assumption in the model where conductive heat-flux to the droplet is assumed to result exclusively from the surface the droplet is rolling upon. In the Leidenfrost distiller channels, however, there is some conductive heat transfer from the distiller walls, which are not accounted for in the model, explaining why the model typically underpredicts evaporation rates, and why there is an increased deviation in the theoretical and experimental evaporation rates at the higher temperature.

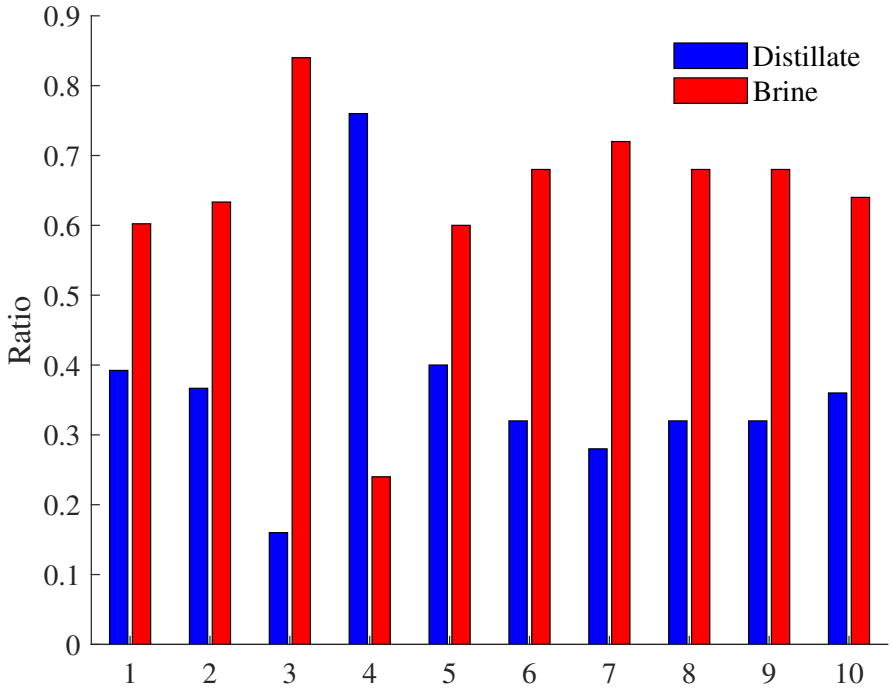

Figure 4.12: Ratio of distillate and brine to the total starting fluid volume out of the Leidenfrost distiller.

The model used to size the Leidenfrost distiller predicted droplet evaporation rates with reasonable accuracy, and exclusively provided conservative estimates for droplet evaporation rates. Therefore, the lack of total droplet distillation in the Leidenfrost distiller is not due to significant inaccuracies in the droplet evaporation model used to size the distiller itself. Further examination of the distiller operation showed that average droplet residence time in the distiller was approximately 30 seconds. The Leidenfrost distiller was designed to operate at 230°C and sized for droplets to reside in the distiller for approximately 75 s to achieve 90% distillation. The distiller was sized with the assumption that droplets would be exclusively gravity driven. In the fully assembled system, the vacuum pump provided a pressure differential to sweep away steam from

the Leidenfrost distiller and induce some airflow in the SPS. This pressure differential unexpectedly added enough momentum to the droplets to increase their speed by over a factor of two.

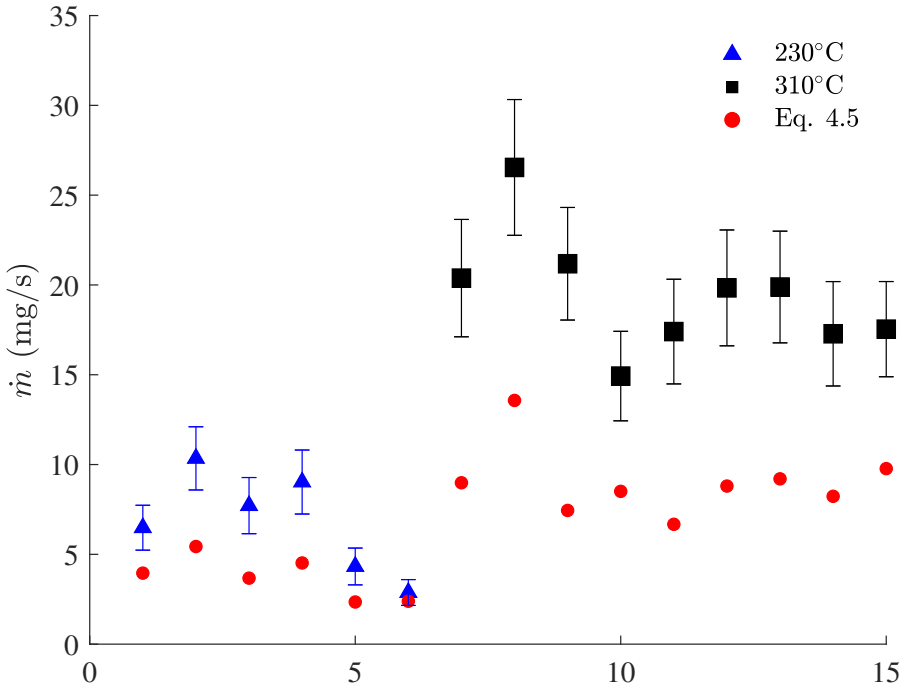

Figure 4.13: Experimental and theoretical salt-water droplet evaporation rates in the Leidenfrost distiller at 230°C and 310°C.

Despite the hindered distillation, the Leidenfrost Distiller performed well. Figure 4.14 shows a plot of measured salinity values of salt-water influent, and captured distillate and salty-brine. The influnt was fed to the distiller at a salinity of 40 mS. For all experimental runs, the distillate salinity was measured at nearly 0 mS indicating that the collected distillate is essentially pure water to measurement accuracy. The brine salinity was measured at an average of about 58 mS across all experimental runs, indicating increased salt-content as water is removed from the droplets.

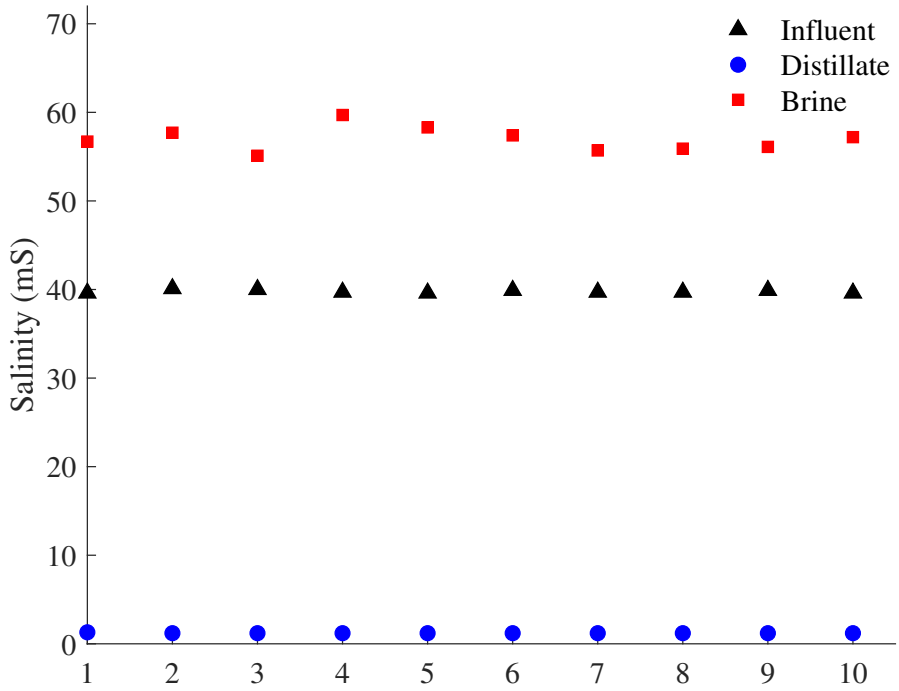

Figure 4.14: Plot of salinity for the influent salt-water and the effluent distillate and brine taken at various intervals during Leidenfrost distiller testing.

4.3.3 Mass and Energy Trade Analysis

The Nanophotonic Heating and Leidenfrost-Driven Fouling-Free WRS was evaluated using the equivalent system mass (ESM) metric as developed by Levri & Vaccari [188] and compared to the current state-of-the-art water recovery technology ESM metrics aboard the International Space Station (ISS). The ESM metric is an equivalent mass value reflective of a system's mass, volume, and energy requirements. The ESM value is used when comparing technologies in order to scope launch and operating costs of a system. The ESM value is computed using the relationship,

$$\text{ESM} = M + \left(V * V_{\text{eq}}\right) + \left(P * P_{\text{eq}}\right) + \left(C * C_{\text{eq}}\right) \tag{4.6}$$

where M is the overall system hardware mass in kg, V is the system volume in m^3, P is the system power requirements in kW, and C is the system cooling power requirement in kW. All aforementioned terms are converted to mass values using V_{eq}, P_{eq}, and C_{eq} which are the volume, power, and cooling infrastructure cost factors, respectively, and have units of kg/m^3, kg/kW, and kg/kW, respectively. The infrastructure cost factors are constant values used to convert system resource requirements to a mass value, and are given by Levri & Vaccari [188]. Crew times are also typically included in ESM trade studies, but in this study the crew times are assumed to be equivalent for both systems, although the Nanophotonic Heating and Leidenfrost-Driven WRS is expected to reduce crew time relative to current state of the art. This is due to less consumables resulting from the elimination of pretreat chemicals and a reduction in system servicing due to a significant reduction of moving parts.

As mentioned earlier, the WRS developed herein boasts several advantages relative to current state-of-the-art technology. The first of which includes the use of nanophotonic pasteurization for microbial control and real-time processing of urine-streams in the Leidenfrost distiller, which eliminates the need for highly acidic and hazardous pretreatment chemicals and the consumable tanks, pumps, controls, and plumbing associated with chemical dosing that is required by the current state-of-the-art. Contact-free Leidenfrost distillation eliminates surface fouling, which decrease system robustness, an issue encountered in the current state-of-the-art. Lastly, passive phase separation replaces the need for moving parts which reduce mass and energy needs. The advantages of the WRS developed herein generally result in reduction in mass, energy, and the need for replacement parts. These advantages serve to make the ESM metric for the system more favorable relative to the current state-of-the-art.

Mass and volume values for the Nanophotonic Heating and Leidenfrost-Driven WRS are obtained by summation of individual component mass measurements and overall footprint measurements of the system prototype shown in Fig. 4.9. Table 4.1 lists the mass, power, and volume requirements for the current state-of-the-art WRS aboard the ISS and for the Nanophotonic Heating and Leidenfrost-Driven WRS. These metrics are converted to an ESM value and listed in Table 4.1. All values for the current state-of-the-art are obtained from Anderson et al. [189]. The Nanophotonic Heating and Leidenfrost-Driven WRS has an ESM value of 392 kg, and attractive ESM value when compared to current state-of-the-art, which has an ESM of 1506 kg. The Nanophotonic Heating and Leidenfrost-Driven WRS traded favorably to the current state-of-the-art in two key metrics, mass and volume. The WRS developed here has a total mass of 245 kg and total volume of 0.5 m^3, while current state-of-the-art has a total mass of 1380 kg and volume of 3.14 m^3. Such dramatic savings in mass and volume are a result of employing capillary forces for phase separation and fluid containment resulting in the elimination of pump equipment, rotary equipment and supporting components in the distillation assembly, chemical pretreatment assembly, and reduced number of filtration beds, which are employed in the current state-of-the-art.

Table 4.1: Mass, power, volume, and ESM values listed for ISS WRS and Nanophotonic Heating and Leidenfrost-Driven WRS

	ISS WRS	Nanophotonic Heating and Leidenfrost-Driven WRS
Mass (kg)	1380	245
Power (W)	560	650
Volume (m^3)	3.14	0.5
ESM (kg)	1506	392

Power requirements for the Nanophotonic Heating and Leidenfrost-Driven WRS are computed from the individual system components operating at peak power levels. The SPS unit consists of IR LEDs to irradiate plasmonic nanoparticles and enable liquid pasteurization. The 12 VDC flexible IR LED strips consist of 60 LED/m at 940 nm peak wavelength and require 4.8 W/m of power. For the holding tank of the SPS, 1.5 m of IR LED's are used resulting in 7.2 W of power consumption. The Vacuum pump requires 208 W to operate, and the condenser cooling loop fans and pump require a total 60 W to operate. The rest of the Nanophotonic Heating and Leidenfrost-Driven WRS power requirements come from the Leidenfrost distiller. Energy consumption of the Leidenfrost distiller is computed using a thermal resistance model. Energy required to heat and maintain the temperature of the aluminum mass that makes up the Leidenfrost distiller is computed using a lumped mass approximation. Assuming a quiescent environment at 20°C, 4" of ceramic fiber insulation insulation for the distiller (k = 0.05 W/mK), and distiller surfaces assumed uniformly held at 230°C results in ~15 W of heat loss to the environment. This energy requirement accounts for energy leaking from the system to the ambient environment in the form of radiation, natural convection, and conduction for the Leidenfrost distiller at steady-state. Distillation of water-based solutions adds an additional energy load to the system in the form of sensible heat to heat urine from an inlet temperature of 20°C to 100°C, and latent heat of vaporization to perform phase change from liquid to steam. This energy load for the Leidenfrost distiller is computed using $q = \dot{m}(c_p \Delta T + h_{fg})$, where $\dot{m}$ is the mass of water processed per hour, and $h_{fg}$is the latent heat of vaporization of water. For a 4 person crew, the target operating rate for the system is to process 500 mL of waste-water per hour. The added energy load to process 500 mL of wastewater per hour adds ~360 W of energy to the sys-

tem at steady-state operating conditions. The resulting total power requirements for this system are ~650 W of power. Savings in mass and volume thwart the effect of the ~90 W increased power consumption of the Nanophotonic Heating and Leidenfrost-Driven WRS relative to the current ISS WRS, although increased power consumption can be attributed to increased distillation levels of waste-water streams, which requires additional energy.

4.4 Conclusion

Developed herein is the first omni-gravity water recovery system (WRS) utilizing non-contact Leidenfrost distillation and nanophotonic heating as methods to promote fouling-free water recovery from waste streams. An omni-gravity passive liquid-gas phase separator was developed utilizing a helical bend to impart centrifugal forces on fluid streams in microgravity promoting wall bounded impacts and subsequent capillary containment in interior corner geometries for perfectly wetting ($\theta = 0°$) and partial-wetting conditions ($0° < \theta < 90°$). Sloped interior geometries were utilized in the phase separator to promote gravity driven draining into a reservoir in a gravity dominated enviornment, wherein gravity is the predominate force for liquid-gas phase separation as opposed to centrifugal forces in microgravity. The phase separator surfaces were coated with carbon black nanoparticles that were irradiated with IR LED strips to induce hyperlocal nanophotonic heating to promote pasteurization of waste-water streams to thwart microbial growth in the phase separator reservoir. These surfaces were shown to heat up to 91°F.

A mathematical model was developed describing droplet evaporation in the Leidenfrost state. The model was then utilized to design and size the Leidenfrost distiller.

The Leidenfrost droplet distiller was built from an aluminum block with a circular track ~8.5 m in length machined with semi-circular cross section at a 0.25° pitch to promote gravity driven droplet transport through the distiller. The distiller was heated past the Leidenfrost point of water on aluminum with a pair of resistance heaters. The Leidenfrost distiller was tested with 40 mS salt-water as a urine ersatz fluid. Throughout the ~20 hr operation of the Leidenfrost distiller, no significant salt-deposits or other forms of fouling were observed on distiller surfaces. Volume and salinity measurements at varying intervals during the operation of the Leidenfrost distiller showed an average water recovery rate of 40% with virtually no salt content in recovered distillate, and an average of 58 mS in the captured residual brine. Upon further investigation, droplet evaporation rates were shown to be predicted with good accuracy for salt-water droplets in the distiller at the design temperature of 230°C and an elevated temperature of 310°C. It was determined that a pressure drop induced by an inline vacuum pump resulted in droplets of salt-water residing in the distiller for ~30 s instead of the design time of 75 s, leading to less than half of the target water-recovery figure of 90%. Auxiliary system components were developed from mostly off-the-shelf components. These system components included vacuum tubing, a vacuum pump, reflux condenser, cooling loop, resistance heaters, and thermal insulation.

The all-gravity nanophotonic heating and Leidenfrost-driven fouling-free WRS was traded against the current state-of-the-art water recovery technology currently aboard the International Space Station (ISS) with the equivalent system mass metric. The water recovery system developed herein trades favorably relative to current state-of-the-art with an equivalent system mass of 392 kg compared to 1506 kg for the current system aboard ISS. The water recovery system developed herein has demonstrated the

feasibility of a fouling-free water recovery system demonstrating numerous advantages relative to current state-of-the-art. These include omni-gravity capability and a reduction in system mass and volume through a reduction in moving parts and storage tanks resulting from the use of capillary fluid management methods and fouling-resistant real-time fluid processing potentially eliminating the need for pretreat chemicals. Heat-driven distillation as a driving force for water-recovery boasts the advantage of achieving 100% water recovery from waste-water streams. Further system development and optimization can readily bring water recovery metrics to 90% and beyond in the non-contact heat-driven Leidenfrost distillation step. Further development of such methods is encouraged for the advancement of water recovery technologies and life support systems technologies at large.

Chapter 5

Parallel Investigations

In this work, a host of parallel investigations were conducted resulting in early first observations of unique fluid phenomenon.

5.1 Airflow-Driven Droplet Levitation on Porous Superhydrophobic Surfaces

A porous superhydrophobic surface is developed utilizing a 3.175 mm thick sintered stainless steel disk 6.35 mm in diameter with nominal pore diameter of 10 μm. Candle soot is deposited on the surface of the stainless steel disk and sprayed with Dome Magic^{TM} PTFE spray producing a superhydrophobic surface. The porous superhydrophobic disk is clamped between two plates. The bottom plate has a hose for pressure-driven airflow upward and underneath the superhydrophobic disk. A sketch of the apparatus is shown in Fig. 5.1. Airflow through the porous disk is driven at 6.9, 20.7, and 137.9 kPa. Droplets of water 0.03 mL in volume are dispensed onto the disk. A camera records the interaction between the droplets and the surface.

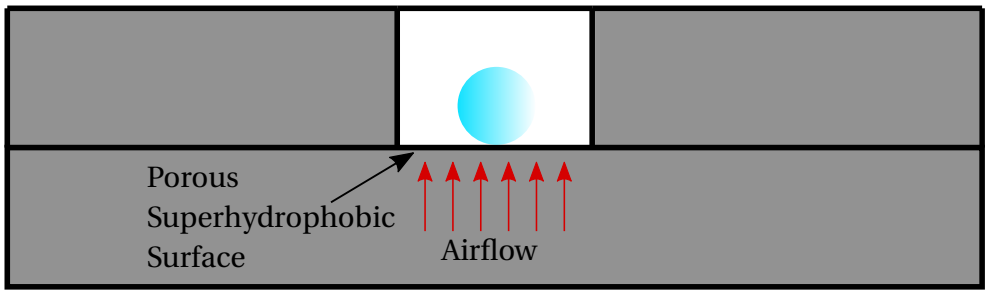

Figure 5.1: An image of a droplet atop a porous superhydrophobic surface with an upward pressure-driven airflow.

Figure 5.2 shows 120 Hz images of 0.03 mL droplets atop the porous superhydrophobic disk with airflow at 6.9 kPa (Fig. 5.2a), 20.7 kPa (Fig. 5.2b), and 137.9 kPa (Fig. 5.2c). All droplets are observed to oscillate due to the pressure resulting from the airflow underneath the droplets. All droplets are in complete non-contact with the porous superhydrophobic surface. Airflow through the surfaces serves as an analog to the Leidenfrost vapor layer.

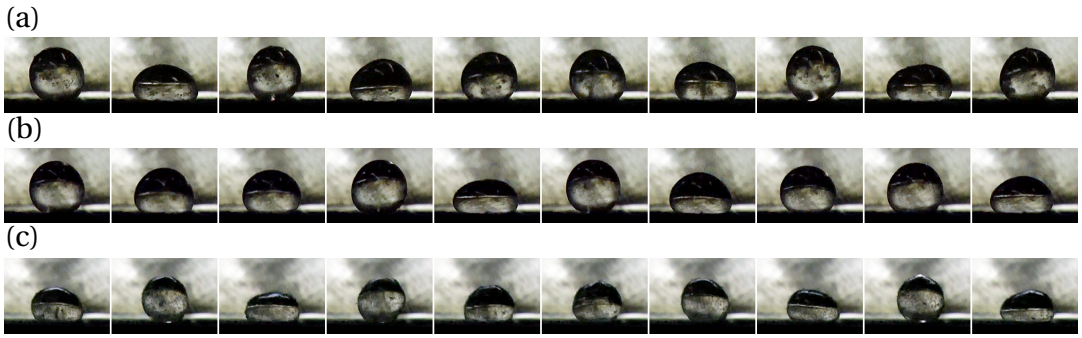

Figure 5.2: 120 Hz images of 0.03 mL droplets atop a porous superhydrophobic surface 3.175 mm thick, 6.35 mm diameter, and 10 μm pore diameter with upward pressure-driven airflow at (a) 6.9 kPa, (b) 20.7 kPa, and (c) 136.9 kPa.

5.2 Leidenfrost-Driven Microgravity Droplet Generator

The oscillation-free microgravity droplet generator referred to as the 'Logan Shooter' was introduced in Chapter 2. Figure 2.9 showed an example of the classic Logan Shooter employing superhydrophobic surfaces to eject a droplet of water free of oscillations out of the device. This device configuration is useful for ejection of non-wetting water, but not for highly wetting fluids. Shown in Fig. 5.3 is a 6 Hz image sequence of a Logan Shooter ejecting liquid nitrogran droplets. The Logan Shooter is made of two aluminum plates formed into a wedge with half-angle of 3°. Liquid ni-

trogen is dispensed in the aluminum wedges held at 20°C, which is greater than the Leidenfrost point of liquid nitrogen. Upon step reduction in gravity resulting from the initiation of the drop-tower test, the puddles of liquid nitrogen attempt to reorient into spheres but are confined by the Logan Shooter surfaces forming capillary pressure gradients in the droplets which force the droplets out of the shooter. The droplets are separated from surfaces by Leidenfrost vapor layers resulting in near-friction-less motion across surfaces. Some of the liquid nitrogen droplet oscillations are dampened and droplets are ejected with maximum droplet diameter and velocity of 10.7 ± 0.1 mm and 10.7 ± 1.4 cm/s, respectively. This is the first demonstration of a Leidenfrost Logan Shooter utilizing Leidenfrost temperatures to promote non-contact, near-friction-less droplet motion in place of superhydrophobic surfaces. Leidenfrost temperatures expand the utility of the Logan Shooter device to all fluids, including highly wetting fluids such as ethanol and potentially oils.

5.3 Liquid-Liquid Interface Puddle Jump

Puddle jumping phenomenon has been studied extensively and was outlined in Chapter 2. Herein, the first demonstrations of puddling jumping phenomenon on liquid-liquid interfaces are demonstrated. Figure 5.4 shows a 5.5 Hz sequence of images of a liquid nitrogen puddle jumping from a bath of water. A volume of liquid nitrogen is dispensed onto the bath of water held at 22°C, greater than the Leidenfrost point of liquid nitrogen. The liquid nitrogen is separated from the water interface by a layer of vapor. Upon a step reduction in gravity, the puddle of liquid nitrogen reorients into a sphere resulting in the collision of capillary waves which cause the droplet to detach from the surface with constant velocity of 6.0 ± 0.7 cm/s. Here, the non-contact

role of superhydrophobic surfaces is replaced with Leidenfrost temperatures, making liquid-liquid puddle jumps feasible.

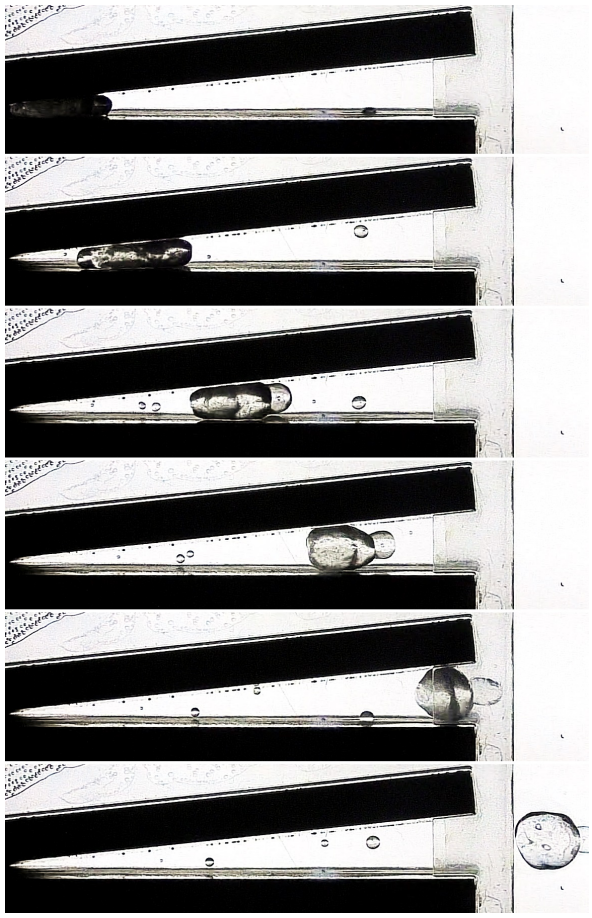

Figure 5.3: Images taken at 6 Hz of an aluminum Logan Shooter with 3° half -angle ejecting liquid nitrogen droplets with maximum diameter and velocity of 10.7 ± 0.1 mm and 10.7 ± 1.4 cm/s, respectively.

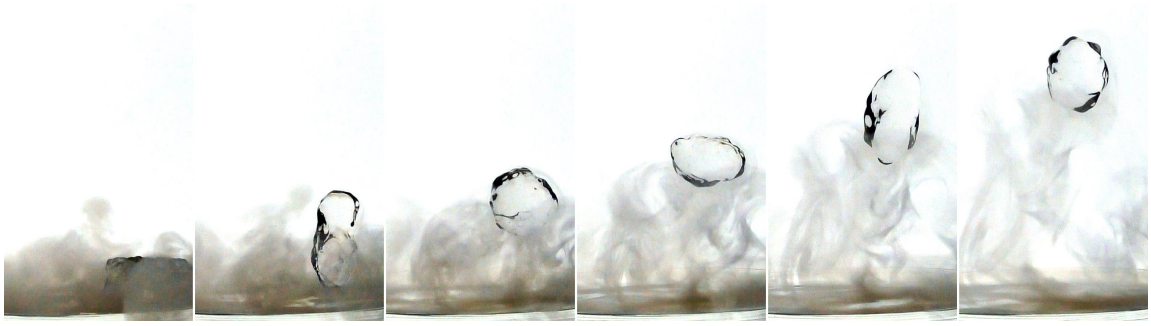

Figure 5.4: A 5.5 Hz sequence of images of a liquid nitrogen puddle with diameter 17.8 ± 0.1 mm puddle jumping from a bath of water with velocity of 6.0 ± 0.7 cm/s.

5.4 Liquid Nitrogen Capillary Auto-Ejection

Auto-ejection of fluids rising in tubes with converging nozzles was outlined in Chapter 2. The first demonstrations of auto-ejection of cryogenic fluids is demonstrated herein. Figure 5.5 shows 30 Hz images of liquid nitrogen auto-ejected with max diameter and velocity of 1.85 ± 0.05 mm and 48.9 ± 2.1 cm/s, respectively, from a 60 mm long 9 mm ID glass tube ejector held at -196°C with converging nozzle of 1.5 mm ID exit.

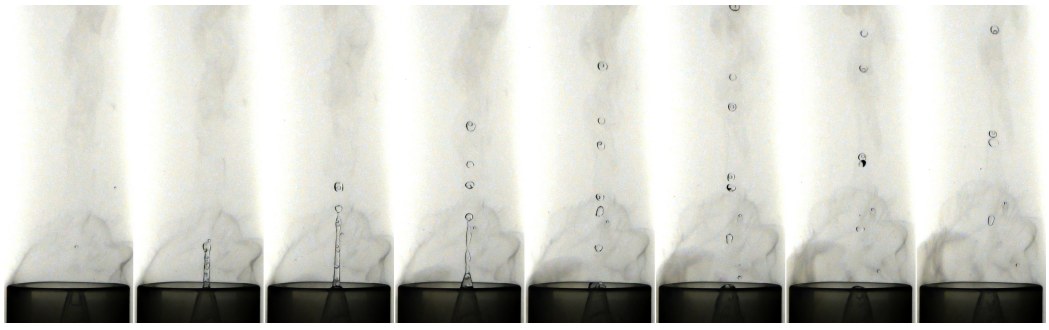

Figure 5.5: A 30 Hz series of images of liquid nitrogen auto-ejected with max diameter and velocity of 1.85 ± 0.05 mm and 48.9 ± 2.1 cm/s, respectively, from a tube ejector with converging nozzle.

[1] F. P. Chiaramonte and J. A. Joshi, "Workshop on critical issues in microgravity fluids, transport, and reaction processes in advanced human support technology," NASA/TM-2004-212940, E-14380, 2004.

[2] M. Jernigan, R. Gatens, J. Perry, and J. Joshi, "The next steps for environmental control and life support systems development for deep space exploration," 48th International Conference on Environmental Systems, #274, 2018.

[3] E. M. Cortright, *Apollo Expeditions to the Moon.* NASA SP-350, 1975.

[4] NASA, "Apollo program summary report," *Houston, Tex.: NASA Manned Spacecraft Center*, JSC-09423, 1975.

[5] NASA, "Apollo 16 mission report," *Houston, Tex.: NASA Manned Spacecraft Center*, MSC-07230, 1972.

[6] R. Orloff and S. Garber, *Apollo by the numbers: a statistical reference.* NASA/SP-2000-4029, 2000.

[7] C. Morgan, "Shuttle-Mir: The united states and russia share history's highest stage," NASA/SP-2001-4225, 2001.

[8] B. J. Motil and J. B. Mcquillen, "Multiphase flow research on the international space station," 2016.

[9] NASA, "Apollo 13 mission report," *Houston, Tex.: NASA Manned Spacecraft Center*, MSC-02680, 1970.

[10] C. Campbell, "Shuttle/ISS EMU failure history and the impact on advanced EMU portable life support system (PLSS) design," 45th International Conference on Environmental Systems, #327, 2015.

[11] J. Steele, C. Metselaar, B. Peyton, T. Rector, R. Rossato, B. Macias, D. Weigel, and D. Holder, "Failure analysis results and corrective actions implemented for the extravehicular mobility unit 3011 water in the helmet mishap," 45th International Conference on Environmental Systems, 2015.

[12] NASA, "Space shuttle technical conference part 1," *NASA Conference Publication 2342, Houston, Tex.: Lyndon B. Johnson Space Center*, N85-16889, 1983.

[13] NASA, "Skylab experience bulletin No. 8 cleansing provisions within the waste management compartment," *Houston, Tex.: Lyndon B. Johnson Space Center*, JSC-09542, 1974.

[14] NASA, "A study of the collection and preservation of biological specimens during space flight for post-flight analysis," *Houston, Tex.: Lyndon B. Johnson Space Center*, NASW-1562, 1967.

[15] NASA, "MSFC skylab orbital workshop volume III," *Huntsville, Ala.: George C. Marshall Space Flight Center*, X-64813, 1974.

[16] NASA, "Design concept definition study for an improved shuttle waste collection subsystem," *Houston, Tex.: Lyndon B. Johnson Space Center*, N85-12546, 1984.

[17] R. Kosson, R. Brown, and E. Ungar, "Space station heat pipe advanced radiator element (share) flight test results and analysis," in *28th Aerospace Sciences Meeting*, p. 59, 1990.

[18] E. K. Ungar and F. A. Ouellette, "Design of a shuttle air and water prefilter for reduced gravity operation," tech. rep., SAE Technical Paper 921161, 1992.

[19] R. A. Scheuring, J. A. Jones, J. D. Novak, J. D. Polk, D. B. Gillis, J. Schmid, J. M. Duncan, and J. R. Davis, "The apollo medical operations project: Recommendations to improve crew health and performance for future exploration missions and lunar surface operations," *Acta Astronautica*, vol. 63, no. 7-10, pp. 980–987, 2008.

[20] J. Gaddis, "Feasibility demonstration of a spraying flash evaporator final report," VMSC Report No. 00.1427, 1971.

[21] C. Hixon and J. Dietz, "Development and parametric evaluation of the prototype 2 and 3 flash evaporators," NASA-CR-144446, 1975.

[22] J. R. Nason, F. A. Wierum, and J. L. Yanosy, "Challenges in the development of the orbiter active thermal control subsystem," NASA. Johnson Space Center Space Shuttle Tech. Conf., Pt. 1 pp. 450-464, 1985.

[23] A. Marmur, "The lotus effect: superhydrophobicity and metastability," *Langmuir*, vol. 20, no. 9, pp. 3517–3519, 2004.

[24] S. Wang, K. Liu, X. Yao, and L. Jiang, "Bioinspired surfaces with superwettability: new insight on theory, design, and applications," *Chemical reviews*, vol. 115, no. 16, pp. 8230–8293, 2015.

[25] D. Kumar, L. Li, and Z. Chen, "Mechanically robust polyvinylidene fluoride (pvdf) based superhydrophobic coatings for self-cleaning applications," *Progress in Organic Coatings*, vol. 101, pp. 385–390, 2016.

[26] Y. Lai, J. Huang, Z. Cui, M. Ge, K.-Q. Zhang, Z. Chen, and L. Chi, "Recent advances in tio2-based nanostructured surfaces with controllable wettability and adhesion," *Small*, vol. 12, no. 16, pp. 2203–2224, 2016.

[27] H. Wang, Y. Zhu, Z. Hu, X. Zhang, S. Wu, R. Wang, and Y. Zhu, "A novel electrodeposition route for fabrication of the superhydrophobic surface with unique self-cleaning, mechanical abrasion and corrosion resistance properties," *Chemical Engineering Journal*, vol. 303, pp. 37–47, 2016.

[28] I. Hejazi, G. M. M. Sadeghi, S. H. Jafari, H. A. Khonakdar, J. Seyfi, M. Holzschuh, and F. Simon, "Transforming an intrinsically hydrophilic polymer to a robust self-cleaning superhydrophobic coating via carbon nanotube surface embedding," *Materials & Design*, vol. 86, pp. 338–346, 2015.

[29] G. D. Bixler and B. Bhushan, "Fluid drag reduction with shark-skin riblet inspired microstructured surfaces," *Advanced Functional Materials*, vol. 23, no. 36, pp. 4507–4528, 2013.

[30] B. Bhushan and Y. C. Jung, "Natural and biomimetic artificial surfaces for superhydrophobicity, self-cleaning, low adhesion, and drag reduction," *Progress in Materials Science*, vol. 56, no. 1, pp. 1–108, 2011.

[31] R. J. Daniello, N. E. Waterhouse, and J. P. Rothstein, "Drag reduction in turbulent flows over superhydrophobic surfaces," *Physics of Fluids*, vol. 21, no. 8, p. 085103, 2009.

[32] N.-R. Chiou, C. Lu, J. Guan, L. J. Lee, and A. J. Epstein, "Growth and alignment of polyaniline nanofibres with superhydrophobic, superhydrophilic and other properties," *Nature nanotechnology*, vol. 2, no. 6, p. 354, 2007.

[33] N. Wang, D. Xiong, Y. Deng, Y. Shi, and K. Wang, "Mechanically robust superhydrophobic steel surface with anti-icing, uv-durability, and corrosion resistance properties," *ACS applied materials & interfaces*, vol. 7, no. 11, pp. 6260–6272, 2015.

[34] L. B. Boinovich, A. M. Emelyanenko, K. A. Emelyanenko, and K. I. Maslakov, "Anti-icing properties of a superhydrophobic surface in a salt environment: an unexpected increase in freezing delay times for weak brine droplets," *Physical Chemistry Chemical Physics*, vol. 18, no. 4, pp. 3131–3136, 2016.

[35] K. Liu, M. Cao, A. Fujishima, and L. Jiang, "Bio-inspired titanium dioxide materials with special wettability and their applications," *Chemical reviews*, vol. 114, no. 19, pp. 10044–10094, 2014.

[36] S. Zheng, C. Li, Q. Fu, W. Hu, T. Xiang, Q. Wang, M. Du, X. Liu, and Z. Chen, "Development of stable superhydrophobic coatings on aluminum surface for corrosion-resistant, self-cleaning, and anti-icing applications," *Materials & Design*, vol. 93, pp. 261–270, 2016.

[37] B. Zhang, J. Li, X. Zhao, X. Hu, L. Yang, N. Wang, Y. Li, and B. Hou, "Biomimetic one step fabrication of manganese stearate superhydrophobic surface as an efficient barrier against marine corrosion and chlorella vulgaris-induced biofouling," *Chemical Engineering Journal*, vol. 306, pp. 441–451, 2016.

[38] L. Zhao, Q. Liu, R. Gao, J. Wang, W. Yang, and L. Liu, "One-step method for the fabrication of superhydrophobic surface on magnesium alloy and its corrosion protection, antifouling performance," *Corrosion Science*, vol. 80, pp. 177–183, 2014.

[39] R. S. Peres, A. F. Baldissera, E. Armelin, C. Alemán, and C. A. Ferreira, "Marine-friendly antifouling coating based on the use of a fatty acid derivative as a pigment," *Materials Research*, vol. 17, no. 3, pp. 720–727, 2014.

[40] Q. Wang, M. Yu, G. Chen, Q. Chen, and J. Tian, "Robust fabrication of fluorine-free superhydrophobic steel mesh for efficient oil/water separation," *Journal of materials science*, vol. 52, no. 5, pp. 2549–2559, 2017.

[41] G. Wang, Z. Zeng, H. Wang, L. Zhang, X. Sun, Y. He, L. Li, X. Wu, T. Ren, and Q. Xue, "Low drag porous ship with superhydrophobic and superoleophilic surface for oil spills cleanup," *ACS applied materials & interfaces*, vol. 7, no. 47, pp. 26184–26194, 2015.

[42] A. Esmaeilirad, *Fabrication of robust superhydrophobic aluminium alloys and their application in corrosion protection.* PhD thesis, 2017.

[43] T. Rezayi and M. H. Entezari, "Fabrication of superhydrophobic iron with anti-corrosion property by ultrasound," *Surface and Coatings Technology*, vol. 309, pp. 795–804, 2017.

[44] A. K. Kota, W. Choi, and A. Tuteja, "Superomniphobic surfaces: design and durability," *MRS Bulletin*, vol. 38, pp. 383–390, 2013.

[45] E. G. Shafrin and W. A. Zisman, "Upper limits for the contact angles of liquids on solids," tech. rep., NAVAL RESEARCH LAB WASHINGTON DC, 1963.

[46] D. Quéré, "Wetting and roughness," *Annu. Rev. Mater. Res.*, vol. 38, pp. 71–99, 2008.

[47] T. Nishino, M. Meguro, K. Nakamae, M. Matsushita, and Y. Ueda, "The lowest surface free energy based on- cf3 alignment," *Langmuir*, vol. 15, no. 13, pp. 4321–4323, 1999.

[48] X. Gao and L. Jiang, "Biophysics: water-repellent legs of water striders," *Nature*, vol. 432, no. 7013, p. 36, 2004.

[49] X.-Q. Feng, X. Gao, Z. Wu, L. Jiang, and Q.-S. Zheng, "Superior water repellency of water strider legs with hierarchical structures: experiments and analysis," *Langmuir*, vol. 23, no. 9, pp. 4892–4896, 2007.

[50] Y. Su, B. Ji, Y. Huang, and K.-c. Hwang, "Natures design of hierarchical superhydrophobic surfaces of a water strider for low adhesion and low-energy dissipation," *Langmuir*, vol. 26, no. 24, pp. 18926–18937, 2010.

[51] Z. Guo and W. Liu, "Biomimic from the superhydrophobic plant leaves in nature: Binary structure and unitary structure," *Plant Science*, vol. 172, no. 6, pp. 1103–1112, 2007.

[52] K. Koch, B. Bhushan, Y. C. Jung, and W. Barthlott, "Fabrication of artificial lotus leaves and significance of hierarchical structure for superhydrophobicity and low adhesion," *Soft Matter*, vol. 5, no. 7, pp. 1386–1393, 2009.

[53] L. Feng, S. Li, Y. Li, H. Li, L. Zhang, J. Zhai, Y. Song, B. Liu, L. Jiang, and D. Zhu, "Super-hydrophobic surfaces: from natural to artificial," *Advanced materials*, vol. 14, no. 24, pp. 1857–1860, 2002.

[54] Z. Sun, T. Liao, K. Liu, L. Jiang, J. H. Kim, and S. X. Dou, "Fly-eye inspired superhydrophobic anti-fogging inorganic nanostructures," *Small*, vol. 10, no. 15, pp. 3001–3006, 2014.

[55] D. Byun, J. Hong, J. H. Ko, Y. J. Lee, H. C. Park, B.-K. Byun, J. R. Lukes, *et al.*, "Wetting characteristics of insect wing surfaces," *Journal of Bionic Engineering*, vol. 6, no. 1, pp. 63–70, 2009.

[56] J. Hasan, H. K. Webb, V. K. Truong, S. Pogodin, V. A. Baulin, G. S. Watson, J. A. Watson, R. J. Crawford, and E. P. Ivanova, "Selective bactericidal activity of nanopatterned superhydrophobic cicada psaltoda claripennis wing surfaces," *Applied microbiology and biotechnology*, vol. 97, no. 20, pp. 9257–9262, 2013.

[57] L. Zhai, M. C. Berg, F. C. Cebeci, Y. Kim, J. M. Milwid, M. F. Rubner, and R. E. Cohen, "Patterned superhydrophobic surfaces: toward a synthetic mimic of the namib desert beetle," *Nano Letters*, vol. 6, no. 6, pp. 1213–1217, 2006.

[58] A. R. Parker and C. R. Lawrence, "Water capture by a desert beetle," *Nature*, vol. 414, no. 6859, p. 33, 2001.

[59] C. Dorrer and J. Ruhe, "Mimicking the stenocara beetle dewetting of drops from a patterned superhydrophobic surface," *Langmuir*, vol. 24, no. 12, pp. 6154–6158, 2008.

[60] R. Garrod, L. Harris, W. Schofield, J. McGettrick, L. Ward, D. Teare, and J. Badyal, "Mimicking a stenocara beetle's back for microcondensation using plasma-chemical patterned superhydrophobic- superhydrophilic surfaces," *Langmuir*, vol. 23, no. 2, pp. 689–693, 2007.

[61] T. Darmanin and F. Guittard, "Recent advances in the potential applications of bioinspired superhydrophobic materials," *Journal of Materials Chemistry A*, vol. 2, no. 39, pp. 16319–16359, 2014.

[62] T. Darmanin, J. Tarrade, E. Celia, and F. Guittard, "Superoleophobic meshes with high adhesion by electrodeposition of conducting polymer containing short perfluorobutyl chains," *The Journal of Physical Chemistry C*, vol. 118, no. 4, pp. 2052–2057, 2014.

[63] R. N. Wenzel, "Resistance of solid surfaces to wetting by water," *Industrial & Engineering Chemistry*, vol. 28, no. 8, pp. 988–994, 1936.

[64] A. Cassie and S. Baxter, "Wettability of porous surfaces," *Transactions of the Faraday society*, vol. 40, pp. 546–551, 1944.

[65] E. Gogolides, K. Ellinas, and A. Tserepi, "Hierarchical micro and nano structured, hydrophilic, superhydrophobic and superoleophobic surfaces incorporated in microfluidics, microarrays and lab on chip microsystems," *Microelectronic Engineering*, vol. 132, pp. 135–155, 2015.

[66] R. Liao, Z. Zuo, C. Guo, Y. Yuan, and A. Zhuang, "Fabrication of superhydrophobic surface on aluminum by continuous chemical etching and its anti-icing property," *Applied Surface Science*, vol. 317, pp. 701–709, 2014.

[67] Y. Zhang, J. Wu, X. Yu, and H. Wu, "Low-cost one-step fabrication of superhydrophobic surface on al alloy," *Applied Surface Science*, vol. 257, no. 18, pp. 7928–7931, 2011.

[68] R. Wu, S. Liang, A. Pan, Z. Yuan, Y. Tang, X. Tan, D. Guan, and Y. Yu, "Fabrication of nano-structured super-hydrophobic film on aluminum by controllable immersing method," *Applied Surface Science*, vol. 258, no. 16, pp. 5933–5937, 2012.

[69] X. Li, Q. Zhang, Z. Guo, T. Shi, J. Yu, M. Tang, and X. Huang, "Fabrication of superhydrophobic surface with improved corrosion inhibition on 6061 aluminum alloy substrate," *Applied Surface Science*, vol. 342, pp. 76–83, 2015.

[70] J. Yang and W. Li, "Preparation of superhydrophobic surfaces on al substrates and the anti-icing behavior," *Journal of Alloys and Compounds*, vol. 576, pp. 215–219, 2013.

[71] W. Liu, L. Sun, Y. Luo, R. Wu, H. Jiang, Y. Chen, G. Zeng, and Y. Liu, "Facile transition from hydrophilicity to superhydrophilicity and superhydrophobicity on aluminum alloy surface by simple acid etching and polymer coating," *Applied Surface Science*, vol. 280, pp. 193–200, 2013.

[72] M. Ruan, W. Li, B. Wang, B. Deng, F. Ma, and Z. Yu, "Preparation and anti-icing behavior of superhydrophobic surfaces on aluminum alloy substrates," *Langmuir*, vol. 29, no. 27, pp. 8482–8491, 2013.

[73] K. Li, X. Zeng, H. Li, and X. Lai, "A study on the fabrication of superhydrophobic iron surfaces by chemical etching and galvanic replacement methods and their anti-icing properties," *Applied Surface Science*, vol. 346, pp. 458–463, 2015.

[74] F. Lv and P. Zhang, "Fabrication and characterization of superhydrophobic surfaces on aluminum alloy substrates," *Applied Surface Science*, vol. 321, pp. 166–172, 2014.

[75] P. Li, X. Chen, G. Yang, L. Yu, and P. Zhang, "Fabrication and characterization of stable superhydrophobic surface with good friction-reducing performance on al foil," *Applied Surface Science*, vol. 300, pp. 184–190, 2014.

[76] L. Feng, Y. Che, Y. Liu, X. Qiang, and Y. Wang, "Fabrication of superhydrophobic aluminium alloy surface with excellent corrosion resistance by a facile and environment-friendly method," *Applied Surface Science*, vol. 283, pp. 367–374, 2013.

[77] A. Esmaeilirad, M. V. Rukosuyev, M. B. Jun, and F. C. van Veggel, "A cost-effective method to create physically and thermally stable and storable superhydrophobic aluminum alloy surfaces," *Surface and Coatings Technology*, vol. 285, pp. 227–234, 2016.

[78] W. Liu, L. Sun, Y. Luo, R. Wu, H. Jiang, Y. Chen, G. Zeng, and Y. Liu, "Facile transition from hydrophilicity to superhydrophilicity and superhydrophobicity on aluminum alloy surface by simple acid etching and polymer coating," *Applied Surface Science*, vol. 280, pp. 193–200, 2013.

[79] D. K. Sarkar, M. Farzaneh, and R. W. Paynter, "Superhydrophobic properties of ultrathin rf-sputtered teflon films coated etched aluminum surfaces," *Materials letters*, vol. 62, no. 8-9, pp. 1226–1229, 2008.

[80] Z. Sun, B. Liu, S. Huang, J. Wu, and Q. Zhang, "Facile fabrication of superhydrophobic coating based on polysiloxane emulsion," *Progress in Organic Coatings*, vol. 102, pp. 131–137, 2017.

[81] S. Agarwal, S. Horst, and M. Bognitzki, "Electrospinning of fluorinated polymers: formation of superhydrophobic surfaces," *Macromolecular Materials and Engineering*, vol. 291, no. 6, pp. 592–601, 2006.

[82] I. O. Arukalam, E. E. Oguzie, and Y. Li, "Nanostructured superhydrophobic polysiloxane coating for high barrier and anticorrosion applications in marine environment," *Journal of colloid and interface science*, vol. 512, pp. 674–685, 2018.

[83] M. Saadat-Bakhsh, H. R. Ahadian, and N. M. Nouri, "Facile, robust and large-scale fabrication method of mechanically durable superhydrophobic pdms/aerogel coating on fibrous substrates," *Cellulose*, vol. 24, no. 8, pp. 3453–3467, 2017.

[84] W.-T. Cao, Y.-J. Liu, M.-G. Ma, and J.-F. Zhu, "Facile preparation of robust and superhydrophobic materials for self-cleaning and oil/water separation," *Colloids and Surfaces A: Physicochemical and Engineering Aspects*, vol. 529, pp. 18–25, 2017.

[85] C. Li, Y. Sun, M. Cheng, S. Sun, and S. Hu, "Fabrication and characterization of a tio2/polysiloxane resin composite coating with full-thickness superhydrophobicity," *Chemical Engineering Journal*, vol. 333, pp. 361–369, 2018.

[86] S. Gao, J. Huang, S. Li, H. Liu, F. Li, Y. Li, G. Chen, and Y. Lai, "Facile construction of robust fluorine-free superhydrophobic tio2@ fabrics with excellent antifouling, water-oil separation and uv-protective properties," *Materials & Design*, vol. 128, pp. 1–8, 2017.

[87] C. Lv, H. Wang, Z. Liu, C. Wang, H. Li, Y. Zhao, and Y. Zhu, "A fluorine-free superhydrophobic pps composite coating with high thermal stability, wear resistance, corrosion resistance," *Progress in Organic Coatings*, vol. 110, pp. 47–54, 2017.

[88] Y. Wu, S. Jia, S. Wang, Y. Qing, N. Yan, Q. Wang, and T. Meng, "A facile and novel emulsion for efficient and convenient fabrication of durable superhydrophobic materials," *Chemical Engineering Journal*, vol. 328, pp. 186–196, 2017.

[89] S. Lei, Z. Shi, J. Ou, W. Li, G. Qiao, and X. Yu, "A facile process for preparing superhydrophobic pbz-ptfe coating with excellent stable properties," *Applied Physics A*, vol. 122, no. 12, p. 1011, 2016.

[90] Y. Li, X. Men, X. Zhu, B. Ge, F. Chu, and Z. Zhang, "One-step spraying to fabricate nonfluorinated superhydrophobic coatings with high transparency," *Journal of materials science*, vol. 51, no. 5, pp. 2411–2419, 2016.

[91] T. F. Qahtan, M. A. Gondal, I. O. Alade, and M. A. Dastageer, "Fabrication of water jet resistant and thermally stable superhydrophobic surfaces by spray coating of candle soot dispersion," *Scientific reports*, vol. 7, no. 1, p. 7531, 2017.

[92] M. Hancer and H. Arkaz, "A facile fabrication of superhydrophobic nanocomposite coating with contact angles approaching the theoretical limit," *Applied Surface Science*, vol. 354, pp. 342–346, 2015.

[93] C. Wei, Y. Tang, G. Zhang, Q. Zhang, X. Zhan, and F. Chen, "Facile fabrication of highly omniphobic and self-cleaning surfaces based on water mediated fluorinated nanosilica aggregation," *RSC Advances*, vol. 6, no. 78, pp. 74340–74348, 2016.

[94] M. Long, S. Peng, X. Yang, W. Deng, N. Wen, K. Miao, G. Chen, X. Miao, and W. Deng, "One-step fabrication of non-fluorinated transparent super-repellent surfaces with tunable wettability functioning in both air and oil," *ACS applied materials & interfaces*, vol. 9, no. 18, pp. 15857–15867, 2017.

[95] X. Liu, Y. Xu, K. Ben, Z. Chen, Y. Wang, and Z. Guan, "Transparent, durable and thermally stable pdms-derived superhydrophobic surfaces," *Applied Surface Science*, vol. 339, pp. 94–101, 2015.

[96] Z. Cai, J. Lin, and X. Hong, "Transparent superhydrophobic hollow films (tshfs) with superior thermal stability and moisture resistance," *RSC Advances*, vol. 8, no. 1, pp. 491–498, 2018.

[97] X. Deng, L. Mammen, H.-J. Butt, and D. Vollmer, "Candle soot as a template for a transparent robust superamphiphobic coating," *Science*, vol. 335, no. 6064, pp. 67–70, 2012.

[98] A. Covelo, C. Menchaca, M. Flores, P. Rodríguez-Rojas, M. Hernandez-Gallegos, E. M. Meza, R. Jaimes-Ramírez, and J. Uruchurtu, "Hydrophobic coatings for corrosion control of aluminum heat exchangers," in *New Technologies in Protective Coatings*, IntechOpen, 2017.

[99] "Portland State Dryden Drop Tower Homepage." `https://www.pdx.edu/dryden-drop-tower/`.

[100] A. Wollman and M. Weislogel, "New investigations in capillary fluidics using a drop tower," *Experiments in fluids*, vol. 54, no. 4, p. 1499, 2013.

[101] A. Wollman, "Capillarity-driven droplet ejection," *Master's Thesis*, 2012. Permanent Link: `http://archives.pdx.edu/ds/psu/8243`.

[102] L. Torres, M. Weislogel, A. Avhad, and H. Tan, "Large droplet generation by capillary migration in super-hydrophobic wedges," *33rd Annual Meeting of the American Society for Gravitational and Space Research*, Oct. 25-28, 2017.

[103] B. Attari, M. Weislogel, A. Wollman, Y. Chen, and T. Snyder, "Puddle jumping: Spontaneous ejection of large liquid droplets from hydrophobic surfaces during drop tower tests," *Physics of Fluids*, vol. 28, no. 10, p. 102104, 2016.

[104] E. Schmidt, "Electro-drop bouncing in low-gravity," *Master's Thesis*, 2018.

[105] A. Wollman, M. Weislogel, B. Wiles, D. Pettit, and T. Snyder, "More investigations in capillary fluidics using a drop tower," *Experiments in Fluids*, vol. 57, no. 4, p. 57, 2016.

[106] L. Torres, "Capillary migration of large confined drops in non-wetting wedges," *Master's Thesis*, 2019.

[107] L. Torres, M. Weislogel, and S. Arnold, "Capillary migration of large confined super-hydrophobic drops in wedges," in *APS Meeting Abstracts*, 2016.

[108] K. Cardin, "Jet rebound from hydrophobic substrates in microgravity," *Master's Thesis*, 2019.

[109] K. Cardin and M. Weislogel, "Rebound of large jets from hydrophobic surfaces in low-gravity," *Bulletin of the American Physical Society*, 2018.

[110] K. Cardin and M. Weislogel, "Capillary fluidics: discovery via drop tower," in *42nd COSPAR Scientific Assembly*, vol. 42, 2018.

[111] M. Weislogel, B. Attari, A. Wollman, K. Cardin, J. Geile, and T. Lindner, "Big hydrophobic capillary fluidics; basically water ping pong in space," in *APS Meeting Abstracts*, 2016.

[112] R. M. Rasheed and M. M. Weislogel, "On-demand non-contact distillation: Low-g demonstrations of a leidenfrost waste-water processor," in *49th International Conference on Environmental Systems*, #222, 2019.

[113] F. P. Chiaramonte and J. A. Joshi, "Workshop on critical issues in microgravity fluids, transport, and reaction processes in advanced human support technology," NASA/TM-2004-212940, E-14380, 2004.

[114] H. W. Jones and M. H. Kliss, "Exploration life support technology challenges for the crew exploration vehicle and future human missions," *Advances in Space Research*, vol. 45, no. 7, pp. 917–928, 2010.

[115] E. Thomas and D. Muirhead, "Impact of wastewater fouling on contact angle," *Biofouling*, vol. 25, no. 5, pp. 445–454, 2009.

[116] C. Ray and B. Salyer, "International space station eclss technical task agreement summary report," 1999.

[117] D. W. Holder Jr, D. L. Carter, and C. F. Hutchens, "Phase iii integrated water recovery testing at msfc: international space station configuration test results and lessons learned," *SAE transactions*, pp. 821–833, 1995.

[118] I. U. Vakarelski, N. A. Patankar, J. O. Marston, D. Y. Chan, and S. T. Thoroddsen, "Stabilization of leidenfrost vapour layer by textured superhydrophobic surfaces," *Nature*, vol. 489, no. 7415, p. 274, 2012.

[119] R. Rasheed and M. Weislogel, "Large length scale leidenfrost phenomena: Recent results from drop tower experimentation," *34th Annual Meeting of the American Society for Gravitational and Space Research*, Oct. 31-Nov. 3, 2018.

[120] J. G. Leidenfrost, *De aquae communis nonnullis qualitatibus tractatus*. Ovenius, 1756.

[121] D. Quéré, "Leidenfrost dynamics," *Annual Review of Fluid Mechanics*, vol. 45, pp. 197–215, 2013.

[122] T. A. Stamey and G. Mihara, "Observations on the growth of urethral and vaginal bacteria in sterile urine," *The Journal of urology*, vol. 124, no. 4, pp. 461–463, 1980.

[123] M. Itaru and M. Kunihide, "Heat transfer characteristics of evaporation of a liquid droplet on heated surfaces," *International journal of heat and mass transfer*, vol. 21, no. 5, pp. 605–613, 1978.

[124] C. Avedisian and J. Koplik, "Leidenfrost boiling of methanol droplets on hot porous/ceramic surfaces," *International journal of heat and mass transfer*, vol. 30, no. 2, pp. 379–393, 1987.

[125] J. D. Bernardin, C. J. Stebbins, and I. Mudawar, "Mapping of impact and heat transfer regimes of water drops impinging on a polished surface," *International Journal of Heat and Mass Transfer*, vol. 40, no. 2, pp. 247–267, 1997.

[126] M. Rein, "Interactions between drops and hot surfaces," in *Drop-Surface Interactions*, pp. 185–217, Springer, 2002.

[127] B. Abramzon and S. Sazhin, "Droplet vaporization model in the presence of thermal radiation," *International Journal of Heat and Mass Transfer*, vol. 48, no. 9, pp. 1868–1873, 2005.

[128] G. Wu and W. A. Sirignano, "Transient convective burning of interactive fuel droplets in double-layer arrays," *Combustion and Flame*, vol. 158, no. 12, pp. 2395–2407, 2011.

[129] S. Sazhin, P. Krutitskii, I. Gusev, and M. Heikal, "Transient heating of an evaporating droplet," *International Journal of Heat and Mass Transfer*, vol. 53, no. 13-14, pp. 2826–2836, 2010.

[130] M. Gradeck, A. Ouattara, D. Maillet, P. Gardin, and M. Lebouché, "Heat transfer associated to a hot surface quenched by a jet of oil-in-water emulsion," *Experimental Thermal and Fluid Science*, vol. 35, no. 5, pp. 841–847, 2011.

[131] L. Tarozzi, A. Muscio, and P. Tartarini, "Experimental tests of dropwise cooling on infrared-transparent media," *Experimental thermal and fluid science*, vol. 31, no. 8, pp. 857–865, 2007.

[132] A.-L. Biance, C. Clanet, and D. Quéré, "Leidenfrost drops," *Physics of Fluids*, vol. 15, no. 6, pp. 1632–1637, 2003.

[133] D. Quéré, "Leidenfrost dynamics," *Annual Review of Fluid Mechanics*, vol. 45, pp. 197–215, 2013.

[134] T. Tran, H. J. Staat, A. Prosperetti, C. Sun, and D. Lohse, "Drop impact on superheated surfaces," *Physical review letters*, vol. 108, no. 3, p. 036101, 2012.

[135] S.-C. Yao and K. Y. Cai, "The dynamics and leidenfrost temperature of drops impacting on a hot surface at small angles," *Experimental Thermal and Fluid Science*, vol. 1, no. 4, pp. 363–371, 1988.

[136] T. Tran, H. J. Staat, A. Susarrey-Arce, T. C. Foertsch, A. van Houselt, H. J. Gardeniers, A. Prosperetti, D. Lohse, and C. Sun, "Droplet impact on superheated micro-structured surfaces," *Soft Matter*, vol. 9, no. 12, pp. 3272–3282, 2013.

[137] M. A. van Limbeek, M. Shirota, P. Sleutel, C. Sun, A. Prosperetti, and D. Lohse, "Vapour cooling of poorly conducting hot substrates increases the dynamic leidenfrost temperature," *International journal of heat and mass transfer*, vol. 97, pp. 101–109, 2016.

[138] M. Gradeck, N. Seiler, P. Ruyer, and D. Maillet, "Heat transfer for leidenfrost drops bouncing onto a hot surface," *Experimental Thermal and Fluid Science*, vol. 47, pp. 14–25, 2013.

[139] J. Park and H. Kim, "An experimental investigation on dynamics and heat transfer associated with a single droplet impacting on a hot surface above the leidenfrost point temperature," *Kerntechnik*, vol. 81, no. 3, pp. 233–243, 2016.

[140] P. Dunand, G. Castanet, M. Gradeck, D. Maillet, and F. Lemoine, "Energy balance of droplets impinging onto a wall heated above the leidenfrost temperature," *International Journal of Heat and Fluid Flow*, vol. 44, pp. 170–180, 2013.

[141] P. Dunand, G. Castanet, M. Gradeck, F. Lemoine, and D. Maillet, "Heat transfer of droplets impinging onto a wall above the leidenfrost temperature," *Comptes Rendus Mécanique*, vol. 341, no. 1-2, pp. 75–87, 2013.

[142] H. Xie and Z. Zhou, "A model for droplet evaporation near leidenfrost point," *International Journal of Heat and Mass Transfer*, vol. 50, no. 25-26, pp. 5328–5333, 2007.

[143] T. Orzechowski and S. Wciślik, "Analysis of d2-law in case of leidenfrost drop evaporation," *Experimental Thermal and Fluid Science*, vol. 59, pp. 230–237, 2014.

[144] L. Maquet, M. Brandenbourger, B. Sobac, A.-L. Biance, P. Colinet, and S. Dorbolo, "Leidenfrost drops: Effect of gravity," *EPL (Europhysics Letters)*, vol. 110, no. 2, p. 24001, 2015.

[145] A. Veldhoven and B. Capelleveen, "Ambient air pressure influence on the dynamic leidenfrost temperature of impacting droplets," B.S. thesis, University of Twente, 2014.

[146] H. Chen, W.-l. Cheng, Y.-h. Peng, and L.-j. Jiang, "Dynamic leidenfrost temperature increase of impacting droplets containing high-alcohol surfactant," *International Journal of Heat and Mass Transfer*, vol. 118, pp. 1160–1168, 2018.

[147] Y. Takata, S. Hidaka, J. Cao, T. Nakamura, H. Yamamoto, M. Masuda, and T. Ito, "Effect of surface wettability on boiling and evaporation," *Energy*, vol. 30, no. 2-4, pp. 209–220, 2005.

[148] S. H. KIM, J. Y. KANG, H. S. AHN, H. J. JO, and M. H. KIM, "Study of leidenfrost mechanism in droplet impacting on hydrophilic and hydrophobic surfaces," *International Journal of Air-Conditioning and Refrigeration*, vol. 21, no. 04, p. 1350028, 2013.

[149] H. Kim, B. Truong, J. Buongiorno, and L.-W. Hu, "On the effect of surface roughness height, wettability, and nanoporosity on leidenfrost phenomena," *Applied Physics Letters*, vol. 98, no. 8, p. 083121, 2011.

[150] H. Kim, B. Truong, J. Buongiorno, and L.-W. Hu, "Effects of micro/nano-scale surface characteristics on the leidenfrost point temperature of water," *Journal of Thermal Science and Technology*, vol. 7, no. 3, pp. 453–462, 2012.

[151] G. C. Lee, J.-y. Kang, H. S. Park, K. Moriyama, S. H. Kim, and M. H. Kim, "Induced liquid-solid contact via micro/nano multiscale texture on a surface and its effect on the leidenfrost temperature," *Experimental Thermal and Fluid Science*, vol. 84, pp. 156–164, 2017.

[152] C. Kruse, T. Anderson, D. Alexander, G. Gogos, and S. Ndao, "Controlling the leidenfrost temperature through laser-assisted surface micro/nano texturing," in *ASME 2013 Heat Transfer Summer Conference collocated with the ASME 2013 7th International Conference on Energy Sustainability and the ASME 2013 11th International Conference on Fuel Cell Science, Engineering and Technology*, pp. V002T07A025–V002T07A025, American Society of Mechanical Engineers, 2013.

[153] C. Kruse, T. Anderson, C. Wilson, C. Zuhlke, D. Alexander, G. Gogos, and S. Ndao, "Extraordinary shifts of the leidenfrost temperature from multiscale micro/-nanostructured surfaces," *Langmuir*, vol. 29, no. 31, pp. 9798–9806, 2013.

[154] G. R. Duursma, R. A. Kennedy, K. Sefiane, *et al.*, "The leidenfrost phenomenon on structured surfaces," 4th Micro and Nano Flows Conference, University College London, No. 69, 2014.

[155] H. Nair, H. J. Staat, T. Tran, A. van Houselt, A. Prosperetti, D. Lohse, and C. Sun, "The leidenfrost temperature increase for impacting droplets on carbon-nanofiber surfaces," *Soft matter*, vol. 10, no. 13, pp. 2102–2109, 2014.

[156] H.-m. Kwon, J. C. Bird, and K. K. Varanasi, "Increasing leidenfrost point using micro-nano hierarchical surface structures," *Applied Physics Letters*, vol. 103, no. 20, p. 201601, 2013.

[157] D. Arnaldo del Cerro, A. G. Marin, G. R. Romer, B. Pathiraj, D. Lohse, and A. J. Huis int Veld, "Leidenfrost point reduction on micropatterned metallic surfaces," *Langmuir*, vol. 28, no. 42, pp. 15106–15110, 2012.

[158] I. U. Vakarelski, N. A. Patankar, J. O. Marston, D. Y. Chan, and S. T. Thoroddsen, "Stabilization of leidenfrost vapour layer by textured superhydrophobic surfaces," *Nature*, vol. 489, no. 7415, p. 274, 2012.

[159] R. M. Rasheed and M. M. Weislogel, "The unrealized potential of superhydrophobic substrates in advanced life support systems," in *49th International Conference on Environmental Systems*, #224, 2019.

[160] S. Ramadhyani, D. Moffatt, and F. Incropera, "Conjugate heat transfer from small isothermal heat sources embedded in a large substrate," *International Journal of Heat and Mass Transfer*, vol. 28, no. 10, pp. 1945–1952, 1985.

[161] M. A. J. van Limbeek, "The dynamics of leidenfrost drops," 2017.

[162] S. Whitaker, "Forced convection heat transfer correlations for flow in pipes, past flat plates, single cylinders, single spheres, and for flow in packed beds and tube bundles," *AIChE Journal*, vol. 18, no. 2, pp. 361–371, 1972.

[163] T. Fujii and H. Imura, "Natural-convection heat transfer from a plate with arbitrary inclination," *International Journal of Heat and Mass Transfer*, vol. 15, no. 4, pp. 755–767, 1972.

[164] W. C. Wong, L. A. Dudinsky, V. M. Garcia, C. M. Ott, and V. A. Castro, "Efficacy of various chemical disinfectants on biofilms formed in spacecraft potable water system components," *Biofouling*, vol. 26, no. 5, pp. 583–586, 2010.

[165] L. Carter, "Status of the regenerative ecls water recovery system," in *40th International Conference on Environmental Systems*, p. 6216, 2010.

[166] D. L. Carter, B. Tobias, and N. Y. Orozco, "Status of iss water management and recovery," in *43rd International Conference on Environmental Systems*, p. 3509, #73, 2013.

[167] J. M. Pruitt, L. Carter, R. M. Bagdigian, and M. J. Kayatin, "Upgrades to the iss water recovery system," 45th International Conference on Environmental Systems, #133, 2015.

[168] M. Weislogel, E. Thomas, and J. Graf, "A novel device addressing design challenges for passive fluid phase separations aboard spacecraft," *Microgravity Science and Technology*, vol. 21, no. 3, p. 257, 2009.

[169] J. Johnson, "Eecom/df82/jsc-19935 shuttle ops v08-waste collection system," *Houson, TX*, 2002.

[170] M. M. Weislogel, E. A. Thomas, and J. C. Graf, "Systems and methods for separating a multiphase fluid," Mar. 15 2011. US Patent 7,905,946.

[171] H. H. Richardson, M. T. Carlson, P. J. Tandler, P. Hernandez, and A. O. Govorov, "Experimental and theoretical studies of light-to-heat conversion and collective heating effects in metal nanoparticle solutions," *Nano letters*, vol. 9, no. 3, pp. 1139–1146, 2009.

[172] A. Agrawal, S. H. Cho, O. Zandi, S. Ghosh, R. W. Johns, and D. J. Milliron, "Localized surface plasmon resonance in semiconductor nanocrystals," *Chemical reviews*, vol. 118, no. 6, pp. 3121–3207, 2018.

[173] N. J. Hogan, A. S. Urban, C. Ayala-Orozco, A. Pimpinelli, P. Nordlander, and N. J. Halas, "Nanoparticles heat through light localization," *Nano letters*, vol. 14, no. 8, pp. 4640–4645, 2014.

[174] O. Neumann, A. S. Urban, J. Day, S. Lal, P. Nordlander, and N. J. Halas, "Solar vapor generation enabled by nanoparticles," *ACS nano*, vol. 7, no. 1, pp. 42–49, 2012.

[175] T. Bora, D. Zoepfl, and J. Dutta, "Importance of plasmonic heating on visible light driven photocatalysis of gold nanoparticle decorated zinc oxide nanorods," *Scientific reports*, vol. 6, p. 26913, 2016.

[176] Y. Zhang, C. Gu, A. M. Schwartzberg, S. Chen, and J. Z. Zhang, "Optical trapping and light-induced agglomeration of gold nanoparticle aggregates," *Physical Review B*, vol. 73, no. 16, p. 165405, 2006.

[177] Z. Fang, Y.-R. Zhen, O. Neumann, A. Polman, F. J. Garcia de Abajo, P. Nordlander, and N. J. Halas, "Evolution of light-induced vapor generation at a liquid-immersed metallic nanoparticle," *Nano letters*, vol. 13, no. 4, pp. 1736–1742, 2013.

[178] V. P. Pattani and J. W. Tunnell, "Nanoparticle-mediated photothermal therapy: A comparative study of heating for different particle types," *Lasers in surgery and medicine*, vol. 44, no. 8, pp. 675–684, 2012.

[179] K. Niikura, N. Iyo, Y. Matsuo, H. Mitomo, and K. Ijiro, "Sub-100 nm gold nanoparticle vesicles as a drug delivery carrier enabling rapid drug release upon light irradiation," *ACS applied materials & interfaces*, vol. 5, no. 9, pp. 3900–3907, 2013.

[180] Z. Zhang, J. Wang, and C. Chen, "Near-infrared light-mediated nanoplatforms for cancer thermo-chemotherapy and optical imaging," *Advanced materials*, vol. 25, no. 28, pp. 3869–3880, 2013.

[181] S.-M. Lee, H. Park, and K.-H. Yoo, "Synergistic cancer therapeutic effects of locally delivered drug and heat using multifunctional nanoparticles," *Advanced Materials*, vol. 22, no. 36, pp. 4049–4053, 2010.

[182] P. D. Dongare, A. Alabastri, S. Pedersen, K. R. Zodrow, N. J. Hogan, O. Neumann, J. Wu, T. Wang, A. Deshmukh, M. Elimelech, *et al.*, "Nanophotonics-enabled solar membrane distillation for off-grid water purification," *Proceedings of the National Academy of Sciences*, vol. 114, no. 27, pp. 6936–6941, 2017.

[183] A. O. Govorov, W. Zhang, T. Skeini, H. Richardson, J. Lee, and N. A. Kotov, "Gold nanoparticle ensembles as heaters and actuators: melting and collective plasmon resonances," *Nanoscale Research Letters*, vol. 1, no. 1, p. 84, 2006.

[184] D. J. de Aberasturi, A. B. Serrano-Montes, and L. M. Liz-Marzán, "Modern applications of plasmonic nanoparticles: from energy to health," *Advanced Optical Materials*, vol. 3, no. 5, pp. 602–617, 2015.

[185] I. U. Vakarelski, N. A. Patankar, J. O. Marston, D. Y. Chan, and S. T. Thoroddsen, "Stabilization of leidenfrost vapour layer by textured superhydrophobic surfaces," *Nature*, vol. 489, no. 7415, p. 274, 2012.

[186] E. Lima, R. Guerra, V. Lara, and A. Guzmán, "Gold nanoparticles as efficient antimicrobial agents for escherichia coli and salmonella typhi," *Chemistry Central Journal*, vol. 7, no. 1, p. 11, 2013.

[187] V. Ravishankar Rai and A. Jamuna Bai, "Nanoparticles and their potential application as antimicrobials," *A Méndez-Vilas A, editor. Mysore: Formatex*, 2011.

[188] J. A. Levri, D. A. Vaccari, and A. E. Drysdale, "Theory and application of the equivalent system mass metric," tech. rep., SAE Technical Paper, 2000.

[189] M. S. Anderson, M. K. Ewert, and J. F. Keener, "Life support baseline values and assumptions document," 2018.